Studies on Photophysical and Electrical Characteristics of Host-Guest Systems in Organic and Organic-Inorganic Hybrid Thin-Films

劉, 学龍

https://hdl.handle.net/2324/7157327

出版情報：九州大学, 2023, 博士（工学）, 課程博士
バージョン：
権利関係：

2023

Doctoral Thesis

有機及び有機-無機ハイブリッド薄膜におけるゲスト-ホストシステムの光物性及び電気物性に関する研究

Studies on Photophysical and Electrical Characteristics of Host-Guest Systems in Organic and Organic-Inorganic Hybrid Thin-Films

Xuelong Liu

Department of Chemistry and Biochemistry,
Graduate School of Engineering,
Kyushu University

Table of contents

Chapter 1

General Introduction

Chapter 1: General introduction

1.1 Introduction

Luminescent materials are a fascinating class of substances that exhibit the ability to emit light when they absorb external energy. This energy absorption can occur through various means, such as exposure to light, heat, electricity, or chemical reactions. Unlike incandescent materials that emit light due to high temperatures, luminescent materials can emit light even in ambient conditions. The emitted light can span a broad spectrum of colors and intensities, depending on the specific properties of the material.

The exploration of luminescent materials dates back to ancient times when civilizations observed certain natural substances (such as “luminous pearls”) glowing in the dark. However, the scientific understanding of luminescence emerged much later. In the 17th century, an Italian shoemaker, V. Casciarolo, observed strong luminescence from a mineral barite, $BaSO_4$, later known as the famous Bologna stone [1]. However, it was not until the 19th century that luminescence began to be studied in depth. One significant breakthrough came in 1852 when British scientist G. G. Stokes discovered the phenomenon of fluorescence [2]. He observed that certain compounds, when illuminated by ultraviolet light, would absorb the light and re-emit it as a different color. Stokes named this phenomenon after the Latin word "fluere," meaning "to flow," due to the flowing nature of the emitted light. Later in the 20th century, the study of luminescent materials gained momentum with advancements in chemistry, materials science, and technology [3-6]. Researchers began synthesizing and manipulating materials to enhance their luminescent properties. This led to the development of various applications, such as fluorescent dyes for microscopy, luminescent paints, and phosphors for electronic displays. With the advent of semiconductor technology, luminescent materials ranging from inorganic, and organic to organic-inorganic hybrid materials (**Figure** 1.1) found their way into optoelectronic devices [7-10]. Light-emitting diodes (LEDs) and organic light-emitting diodes (OLEDs) revolutionized the lighting industry and display technologies, offering energy-efficient and vibrant lighting solutions. Furthermore, luminescent materials have found applications in diverse fields such as medicine, environmental monitoring, security, and art. They continue to be an active area of research, with scientists striving to discover new materials and improve their efficiency, stability, and range of colors.

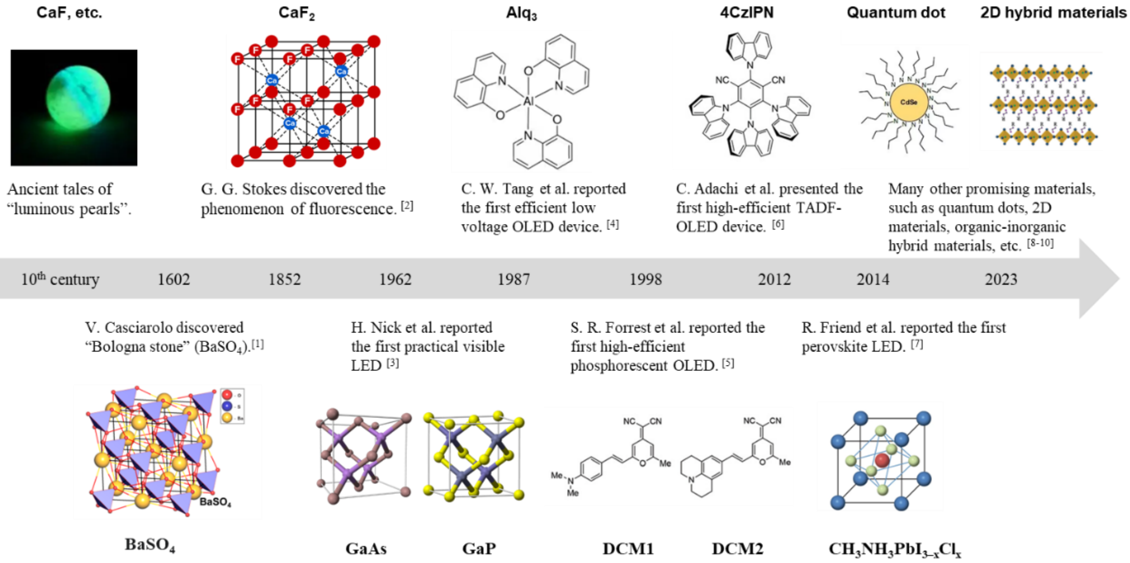

Figure 1.1 The evolution of luminescent materials.

1.2 Host-Guest (H-G) system for luminescent materials

One approach to enhance the luminescent properties and functionality of these materials is through the utilization of H-G systems [11, 12]. H-G systems have many advantages for luminescent materials, primarily by providing a favorable environment for luminescent guests, thereby enhancing their luminescence efficiency. By dispersing the luminescent molecules or ions within a host matrix, undesired interactions such as aggregation or quenching can be minimized or eliminated. The host matrix can act as a protective shell, isolating the guests from external factors that may impede their luminescence, resulting in improved emission properties, higher quantum yields, and prolonged excited-state lifetimes. Further, H-G systems offer a versatile platform for tuning the emission colors of luminescent materials. By carefully selecting the host matrix, the energy levels and electronic environments can be tailored to influence the emission properties of the guest species. This flexibility allows for the design of luminescent materials with a wide range of emission colors, spanning the visible and near-infrared regions. Moreover, H-G systems can allow for the exchange or replacement of guest species within the host matrix. This feature provides versatility in tailoring the luminescent properties or incorporating multiple guest species with different emission characteristics. Furthermore, reversible guest binding and release can be achieved, enabling materials with switchable luminescence or reusability. All in all, H-G systems provide a powerful strategy for enhancing and controlling the luminescent properties of materials. Through the dispersion of luminescent guests within a host matrix, improved luminescence efficiency, tunability of emission colors and guest exchange capabilities can be achieved. The utilization of H-G systems expands the possibilities for developing advanced luminescent materials for a wide range of applications, paving the way for future advancements in areas such as lighting, displays, sensing, and biomedical technologies. However, the selection of materials in H-G systems is of paramount importance, as it directly influences the performance, stability, and functionality of these systems. Based on the types of materials, the H-G system can be divided into inorganic-inorganic, organic-organic, and organic-inorganic H-G systems. This thesis aims to highlight the significance of luminescent material selection in two specific types of H-G systems: organic-organic and organic-inorganic.

1.2.1 Organic-Organic H-G system

In organic-organic H-G systems refer to the use of an organic host layer doped with organic emitters. While organic materials can be either small molecules or polymers, this thesis exclusively focuses on small molecules. The choice of luminescent materials is critical for achieving desired luminescent properties and functionality. Several studies have investigated the use of organic-organic H-G systems for light emission and discussed the requirements for achieving high efficiency and stability. Liu et al. examined the impact of the energy level relationship between organic host and organic guest molecules on OLED performance [13]. Their findings suggest that the host materials with higher triplet energy levels than that of the guests and with the lowest unoccupied molecular orbital (LUMO) and highest occupied molecular orbital (HOMO) level within the host materials lead to high-efficiency OLEDs. Lee et al. discussed the importance of thermal stability in organic materials on the performance of OLEDs [14]. This review indicates that organic semiconductor materials with high thermal stability result in stable OLEDs, while organic materials with low thermal stability inevitably experience molecular motion, resulting in the degradation of organic molecules. Moreover, Chiu et al. emphasized that the well-balanced hole and electron mobilities of the organic-organic H-G system are crucial for achieving high-efficiency OLEDs [15]. In summary, an ideal H-G system for light-emitting applications should satisfy suitable band alignment, balanced charge carrier mobility, and high thermal stability.

1.2.2 Inorganic-organic H-G system

Since organic-organic H-G systems are typically formed by an amorphous film, a rather large distance between adjacent molecules creates an energy barrier for the transport of charge carriers. As a result, the charge conductivity of these systems is often limited. In contrast, inorganic materials tend to be crystalline textures with a long-range order, resulting in the formation of a band structure. This provides rather high carrier mobilities in the valance band (VB) and conduction band (CB). In addition, inorganic semiconductor materials possess a rigid and stable structure that can limit molecular motions and vibrations. By doping organic materials into an inorganic host framework, it is possible to further restrict these motions and vibrations, thereby reducing nonradiative loss of singlet and triplet excitons and enhancing emission output. Furthermore, the H-G system can be tuned based on the H-G interaction, variable molecular aggregation, and the external doping of inorganic ions. Despite the potential advantages of inorganic hosts, only a few works have utilized them in the formation of inorganic-organic H-G systems through the doping of organic emitters [16-18]. One promising approach involves the use of perovskite as an inorganic host doped with organic emitter coumarin 153. This has been shown to result in a reduction of driving voltage and enhancement of external quantum efficiency compared to the devices with conventional organic host materials [18]. Due to its designable structure, perovskite materials have great potential for constructing high-performance inorganic-organic H-G systems.

1.3 Carrier dynamics and exciton behavior in H-G system

1.3.1 Exciton generation and dissociation

Exciton formation occurs in many solid states, which is defined as an electron-hole pair bound by coulombic interaction. In organic materials, excitons are typically generated when a photon with sufficient energy is absorbed, exciting an electron into the LUMO level and leaving a hole behind in the HOMO level. The electron and hole remain coulombically attracted to each other, forming the exciton. Alternatively, the exciton formation can also occur when an electron and a hole injected from opposite electrodes converge and form a bound state without recombination. The former mechanism is particularly common in photoexcitation processes, while the latter plays an important role in OLEDs.

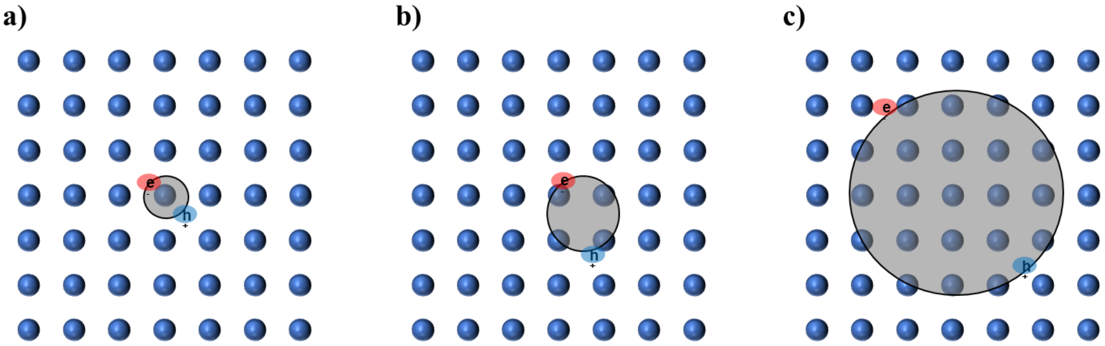

Frenkel exciton **Charge transfer (CT) exciton** **Wannier-Mott exciton**

Figure 1.2 Schematic representation of three types of excitons: (a) Frenkel, (b) CT, and (c) Wannier-Mott.

To date, three types of excitons have been observed in semiconductors, namely Frenkel, charge-transfer (CT), and Wannier-Mott exciton, which are shown schematically in **Figure** 1. 2. Frenkel excitons are localized on a single molecule and have a high binding energy of the order of 1 eV due to the small radius. On the other hand, CT excitons are localized on adjacent molecules with slightly smaller binding energy. Frenkel and CT excitons are widely investigated in organic semiconductor materials, where they dominate the optical absorption and emission processes. In contrast, Wannier-Mott excitons typically occur in inorganic semiconductors and have a large radius, resulting in lower binding energy (typically, a few meV).

1.3.2 Intramolecular and intermolecular energy transfer

Energy decay/transfer in a H-G system can be categorized as either intramolecular or intermolecular. Once an organic molecule is excited, the formed exciton can be either singlet (S) or triplet (T), depending on the spin of the charge carriers. The excited molecule will be in a non-equilibrium state and will dissipate the energy to return to the ground state. Typically, a series of processes, including vibration relaxation, internal conversion, intersystem crossing (ISC), fluorescence, and phosphorescence, can take place within the organic molecule to bring the excited molecule back to the ground state. In addition to the intramolecular energy decay, intermolecular energy transfer occurs when the excitons migrate or diffuse freely within the bulk materials. There are two types of intermolecular energy transfer mechanisms: Förster energy resonant energy transfer (FRET) and Dexter energy transfer (DET) as shown in **Figure** 1.3. FRET typically occurs over a long distance, and its transfer efficiency is highly dependent on the overlap integral between the donor's emission spectrum and the acceptor's absorption spectrum. DET, on the other hand, is a short-range energy transfer that occurs only within 10 angstroms. In this case, the orbitals of the donor and acceptor need to be overlapped for direct electron exchange. Inorganic semiconductor materials emit light via a band-to-band transition, and efficient energy transfer between inorganic and organic semiconductors has been demonstrated. This energy transfer, either by FRET or DET, can achieve high efficiency by designing a hybrid organic-inorganic structure that allows the transfer between Wannier-type excitons and Frenkel-type excitons.

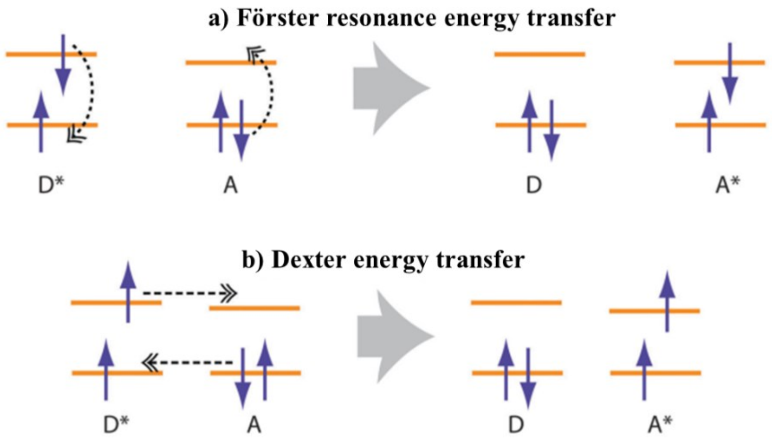

Figure 1. 3 (a) FRET and (b) DET processes. The horizontal lines represent the HOMO and LUMO energy levels of both donor and acceptor molecules where the asterisk denotes the excited states. The dashed arrow indicates the simultaneous rearrangement of the electronic configuration [19].

1.3.3 Charge transport and recombination

Charge transport is an essential process that underlies many of the electronic and optoelectronic properties of semiconductors. Inorganic semiconductors, such as silicon, gallium arsenide, and III-V compounds, have been extensively studied and are widely used in electronic devices [20-23]. In these materials, the charge transport is mainly governed by the movement of electrons and holes in the conduction and valence bands, respectively. The mobility of these charge carriers is determined by various factors, including the crystal structures, defects, and impurities, which can affect their scattering and trapping. Additionally, inorganic semiconductors can exhibit unique electronic properties, such as quantum confinement, where the confinement of electrons and holes in small dimensions leads to discrete energy levels and enhanced excitonic effects, as observed in perovskite materials. On the other hand, organic semiconductors, such as small molecules (which are the focus of this thesis), rely on the hopping of the charge carriers between localized states within the energy bandgap, known as the transport through trap states [24-26]. The mobility of these charge carriers is strongly influenced by the molecular structures and intermolecular interactions, which can affect the charge transfer integral and the reorganization energy. However, this hopping transport is often slow and thermally activated, limiting their device performance. Nonetheless, with tighter molecular packing and ordered structures, the interaction between two molecules can be enhanced and carriers can be further delocalized. Thus, organic molecules can also achieve high carrier mobility. If the electrons and holes in a semiconductor are not collected by the electrodes, they will recombine with each other. This recombination can occur either radiatively or non-radiatively. The former process involves the emission of a photon when the electron and holes recombine, while the latter process does not produce any photons. Recombination can also be classified into different types, including band-to-band recombination, trap-assisted recombination, and Auger recombination.

1.4 Heterostructure and band alignment

A heterostructure refers to the junction formed between two different semiconductor materials with distinct electronic properties, such as bandgap, carrier mobility, and doping concentration. When two semiconductors are brought into contact, the electronic properties at their interface can be altered due to the difference in the energy levels of their valence and conduction bands. This leads to a change in the distribution of charge carriers and transport properties [27, 28].

One of the crucial factors that determine the electronic properties of heterojunctions is the energy level alignment between the two semiconductors at the interface. The energy level alignment refers to the relative positions of the valence and conduction band edges or HOMO and LUMO of the two semiconductors concerning the vacuum level. This alignment can significantly affect the injection, extraction, and recombination of charge carriers across the heterojunction, as well as the formation and dissociation of excitons, which are bound electron-hole pairs that contribute to light emission and absorption. There are three types of energy level alignment at a heterostructure: Type I, Type II, and Type III, as shown in **Figure**1. 4. The Type III heterostructures are rare, and this thesis only focuses on Type I and Type II.

In a Type I heterostructure, the band gap of one semiconductor material overlaps with that of the other material. This type of heterostructure confines both electrons and holes in the lower-band-gap material. Due to the confinement, Type I heterostructures are typically used in OLEDs. On the other hand, in a Type II heterostructure, both the CB and VB of one material are lower than those of other materials. In this case, excitons formed in such a structure are dissociated at the heterointerface, with electrons confined in one material and holes restricted in the other material. Therefore, Type II heterostructures are commonly utilized in solar cells.

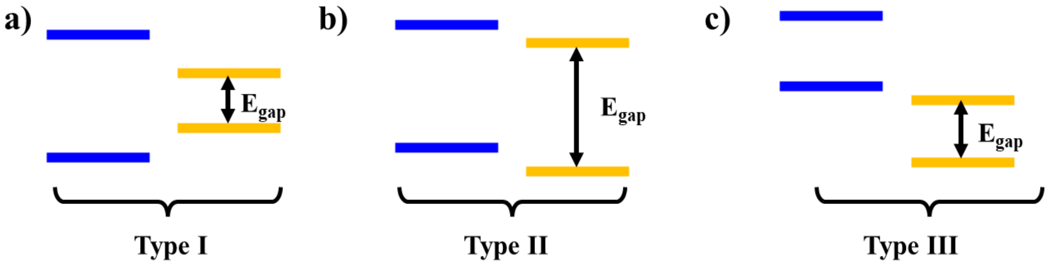

Figure 1. 4 Type I (a), Type II (b), and Type III (c) heterostructures.

1.5 Overview of the Dissertation

Luminescent materials play a crucial role in various fields, including optoelectronics, photonics, sensing, and bioimaging. Over the years, significant advancements have been made in the development of luminescent materials, ranging from purely inorganic systems and organic systems to organic-inorganic hybrid H-G systems. Organic luminescent materials, based on carbon-based molecules, have demonstrated remarkable properties such as tunable emission wavelengths, high quantum yields, and solution processability. They have found applications in optoelectronics, photonics, sensing, and bioimaging. Organic materials, including, small organic molecules, and organic dyes, have shown great potential for devices like OLEDs, OSCs, and biological imaging tools. The integration of organic luminophores into inorganic host materials has led to the emergence of organic-inorganic hybrid H-G systems. These systems combine the desirable properties of both organic and inorganic components, offering enhanced luminescent properties and functionality. Organic-inorganic hybrids have shown promise in light-emitting devices, sensing, and catalysis. Despite significant progress, the development of high-efficiency luminescent materials remains a crucial focus. There are several areas that require attention to further enhance the performance of luminescent materials, such as the photoluminescent quantum efficiency (PLQY), stability and lifetime, broad spectral coverage, energy transfer and exciton management, device integration and manufacturing. Therefore, Continued research and innovation are essential to tackle these challenges and advance the field of luminescent materials. By improving the efficiency, stability, spectral coverage, and device integration capabilities, high-performance luminescent materials can revolutionize various industries, including lighting, energy, displays, sensing, and healthcare applications. Inspired by this motivation, this dissertation is dedicated to designing luminescent materials in H-G systems from organic-organic to inorganic-organic approaches, and investigating their application for light emission. The goal is to demonstrate the unique advantages of organic-organic and organic-inorganic hybrid H-G systems for light emission. All the works are summarized in **Figure** 1.6.

First, in Chapter 2, we introduced a deuterated organic-organic H-G system. The photophysical properties of the H-G system based on deuterated 2,6-di(9H-carbazol-9-yl-)pyridine-$\boldsymbol{d_{16}}$ (PYD2Cz-d_{16}) were similar to that of non-deuterated PYD2Cz. However, the physical properties of their thin films were quite different. The green device using this deuterated H-G system demonstrated operational stability (LT_{95}) which is 1.7 times longer than that of the non-deuterated H-G system. Hole-only and electron-only devices (HODs/EODs) demonstrated that the deuterated H-G system possesses comparable hole transport and electron transport properties. The well-balanced carrier transport properties of the deuterated H-G system can provide a broad recombination zone, hence increasing the LT_{95} in the OLEDs.

In Chapter 3: Inspired by the advantage of balanced carrier transport, we proposed a novel H-G system formed by organic and inorganic materials in a perovskite structure, as the perovskite has an intrinsically balanced carrier transport ability. We also examined the electronic and photophysical properties of this hybrid system using experimental and theoretical investigations. Finally, the hybrid system presented two intercalated separate pathways for electrons and holes, indicating the exciton can be dissociated at the heterointerface. This work would give insight into understanding the band alignment effect on the performance of inorganic-organic hybrid systems, which is paramount for future optoelectronic applications.

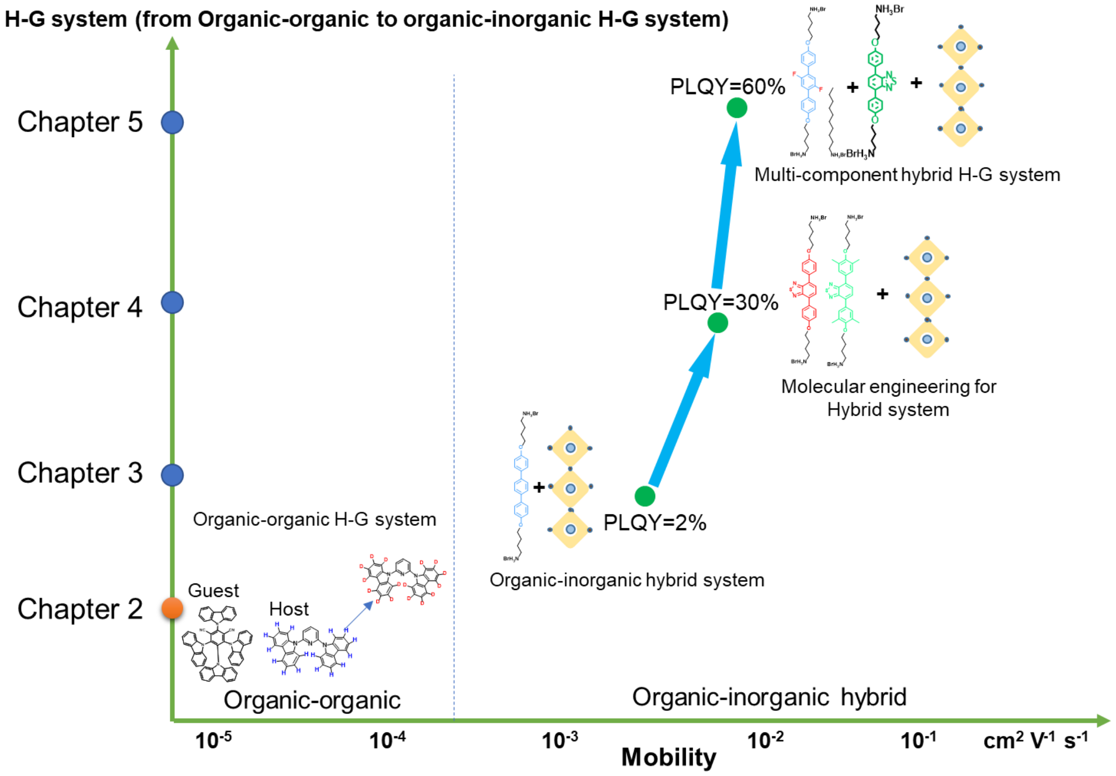

Figure 1.5 Summary of this work for H-G systems from organic-organic to organic-inorganic hybrid approaches.

Chapter 4 proposes two newly designed organic guest emitters, 4,4'-((benzo[c][1,2,5]thiadiazole-4,7-diylbis(4,1-phenylene))bis(oxy))bis(butan-1-aminium) bromide (BT) and 4,4'-((benzo[c][1,2,5]thiadiazole-4,7-diylbis(2,6-dimethyl-4,1-phenylene))bis(oxy)) bis(butan-1-aminium)dibromide (4mBT), introduced into the inorganic framework to form a H-G system. These perovskite films exhibit a Type I heterostructure formed by the organic and inorganic layers. Moreover, the 2-dimensional (2D) perovskite films with BT and 4mBT formed a vertically oriented structure that allows charge carriers to travel through the inorganic layers between two electrodes. Furthermore, these 2D perovskite films with a Type I heterostructure exhibit efficient FRET from the inorganic layer to the organic layer, resulting in high PLQYs. The vertically oriented hybrid H-G system with efficient interlayer energy transfer holds great potential for optoelectronic device applications.

In Chapter 5, we improved the performance of this inorganic-organic hybrid H-G system by introducing several additional organic host materials into the perovskite structure to form a multi-component H-G system. This system allows the host material to disperse the emitter (such as the BT molecule) and weaken concentration quenching. By carefully designing the host materials, the multi-component H-G systems exhibited higher PLQY than that of single H-G systems. Finally, this thesis concludes with some future topics for further H-G systems, especially the application of these H-G systems.

1.6 References

1. Hölsä, J. Persistent luminescence beats the afterglow: 400 years of persistent luminescence. *Electrochem. Soc. Interface* **18**, 42 (2009).
2. Stokes, G.G. On the change of refrangibility of light. *Philos. Trans. R. Soc. London*, **142**, 463-562 (1852).
3. Holonyak Jr, N. & Bevacqua, S.F. Coherent (visible) light emission from Ga (As1− x P x) junctions. *Appl. Phys. Lett.* **1**, 82-83 (1962).
4. Tang, C.W. & VanSlyke, S.A. Organic electroluminescent diodes. *Appl. Phys. Lett.* **51**, 913-915 (1987).
5. Baldo, M.A. et al. Highly efficient phosphorescent emission from organic electroluminescent devices. *Nature* **395**, 151-154 (1998).
6. Uoyama, H., Goushi, K., Shizu, K., Nomura, H. & Adachi, C. Highly efficient organic light-emitting diodes from delayed fluorescence. *Nature* **492**, 234-238 (2012).
7. Tan, Z.-K. et al. Bright light-emitting diodes based on organometal halide perovskite. *Nature Nanotech.* **9**, 687-692 (2014).

8. Sadeghi, S. et al. Quantum dot white LEDs with high luminous efficiency. *Optica* **5**, 793-802 (2018).

9. Bae, W.K. et al. R/G/B/natural white light thin colloidal quantum dot-based light-emitting devices. *Adv. Mater.* **26**, 6387-6393 (2014).

10. Jing, C.Q. et al. Improving Broadband White-Light Emission Performances of 2D Perovskites by Subtly Regulating Organic Cations. *Chem. Eur. J.* **26**, 10307-10313 (2020).

11. Diaz, A.L. Progress in Understanding Host-Sensitized Excitation Processes in Luminescent Materials. *ECS J. Solid State Sci. Technol.* **8**, R14 (2019).

12. Hong, G. et al. A brief history of OLEDs emitter development and industry milestones. *Adv. Mater.* **33**, 2005630 (2021).

13. Liu, W. et al. Effect of the relationship between the energy levels of host and guest on EL performance of phosphorescence organic light-emitting diodes. *Org. Electron.* **93**, 106128 (2021).

14. Lee, S., Kim, H. & Kim, Y. Progress in organic semiconducting materials with high thermal stability for organic light-emitting devices. *InfoMat* **3**, 61-81 (2021).

15. Huang, J.-Y. et al. Revealing the mechanism of carrier transport in host-guest systems of organic materials with a modified Poisson and drift-diffusion solver. *Phys. Rev. Mater.* **4**, 125602 (2020).

16. Doki, N. & Yokota, M. Luminescent characteristic of organic compound-containing inorganic crystal at room temperature. *Adv. Chem. Eng.* **5**, 441 (2015).

17. Xiao, G., Zhou, B., Fang, X. & Yan, D. Room-temperature phosphorescent organic-doped inorganic frameworks showing wide-range and multicolor long-persistent luminescence. *Res.* **2021** (2021).

18. Matsushima, T. et al. Enhanced Electroluminescence from Organic Light-Emitting Diodes with an Organic–Inorganic Perovskite Host Layer. *Adv. Mater.* **30**, 1802662 (2018).

19. Mikhnenko, O.V., Blom, P.W. & Nguyen, T.-Q. Exciton diffusion in organic semiconductors. *Energy Environ. Sci.* **8**, 1867-1888 (2015).

20. Rech, B. & Wagner, H. Potential of amorphous silicon for solar cells. *Appl. Phys. A* **69**, 155-167 (1999).

21. Blakemore, J. Semiconducting and other major properties of gallium arsenide. *J. Appl. Phys.* **53**, R123-R181 (1982).

22. Mikhailova, M.P., Moiseev, K.D. & Yakovlev, Y.P. Discovery of III–V semiconductors: physical properties and application. *Semicon.* **53**, 273-290 (2019).

23. Joyce, H.J. et al. III–V semiconductor nanowires for optoelectronic device applications. *Prog. Quantum Electron.* **35**, 23-75 (2011).

24. Glaeser, R. & Berry, R.S. Mobilities of electrons and holes in organic molecular solids. Comparison of band and hopping models. *J. Chem. Phys.* **44**, 3797-3810 (1966).

25. Guo, A.-M., Hu, P.-J., Gao, X.-H., Fang, T.-F. & Sun, Q.-F. Topological phase transitions of Thouless charge pumping realized in helical organic molecules with long-range hopping. *Phys. Rev., B* **102**, 155402 (2020).

26. Houili, H., Tutiš, E., Batistić, I. & Zuppiroli, L. Investigation of the charge transport through disordered organic molecular heterojunctions. *J. Appl. Phys.* **100**, 033702 (2006).

27. Shi, E., Gao, Y., Finkenauer, B.P., Coffey, A.H. & Dou, L. Two-dimensional halide perovskite nanomaterials and heterostructures. *Chem. Soc. Rev.* **47**, 6046-6072 (2018).

28. Liao, W., Huang, Y., Wang, H. & Zhang, H. Van der Waals heterostructures for optoelectronics: progress and prospects. *Appl. Mater. Today* **16**, 435-455 (2019).

Chapter 2

Isotope effect of organic-organic H-G system

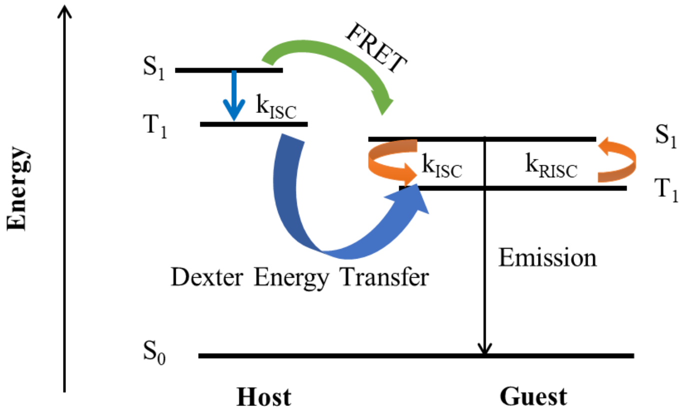

Chapter 2: Isotope effect of organic-organic H-G system

2.1 Introduction

Luminescent materials have attracted tremendous attention due to their wide applications in full-color flat-panel displays and solid-state lighting sources[1, 2]. Nearly all Luminescent materials are based on H-G systems in which guest materials are homogeneously doped into host matrices to tune the performance of the light emission. The overall performance of H-G systems is typically determined by the selection of suitable host and guest materials. Hence, the design of both host and guest components is paramount in achieving highly efficient light emissions. In recent years, the concept of Thermally Activated Delayed Fluorescence (TADF) has emerged as a captivating approach for guest material selection. TADF involves the conversion of triplet excitons into delayed fluorescence through thermal energy, thereby presenting an attractive avenue for achieving 100% Internal Quantum Efficiency (IQE) without the need for noble metals. [3-6]. Since the efficient TADF-OLEDs were reported in 2012,[5] numerous efforts have been devoted to enhancing their Electroluminescence (EL) efficiency and color purity. However, the development of stable host-guest systems for high-performance TADF-OLEDs remains a major obstacle impeding their commercialization. [7-9]

In fact, the choice of host materials has a pronounced effect on device stability. It has been reported that the device operational stability of TADF or phosphorescent (Ph) OLEDs are significantly increasing when chemically stable materials are utilized as the host.[10-12] Numerous reports of rational molecular design of the H-G system have pointed out the importance of balanced carrier transporting properties of host materials to expand a recombination zone and extend their device stability. [13, 14]

One of the interesting reports is the device operational lifetime of the reported Ph-OLED using deuterated host materials, in which hydrogen atoms are replaced by deuterium atoms, was improved; LT_{50} from 0.5 h to 2 h.[15] It is believed that the reason for extended device lifetimes originated from the heavier deuterium atom that may lead slower kinetic rate for unwarranted chemical reactions.[16, 17]. However, the mechanism of improved device stability of deuterated hosts-guest system in OLEDs is still unclear and there is no report of using deuterated hosts in TADF-OLEDs.

In this chapter, we introduced a deuterated host, namely PYD2Cz-d_{16}, and TADF green emitter (4s,6s)-2,4,5,6-tetra(9H-carbazol-9-yl)isophthalonitrile (4CzIPN) to form an orgnaic-organic H-G system. The photophysical properties of the deuterated and non-deuterated H-G systems were investigated. Additionally, the results show PYD2Cz-d_{16} forms a denser film than that of the PYD2Cz. The operational stability (LT_{95}) of the deuterated H-G system-based OLEDs (green device) is 1.7-times longer than that of the non-deuterated H-G system-based TADF-OLED. HODs/EODs demonstrated that PYD2Cz-d_{16} possesses comparable hole transport and electron transport properties. The well-balanced carrier transport properties of the deuterated H-G system can provide a broad recombination zone, hence increasing the LT_{95} in the OLEDs.

2.2 Results and Discussion

2.2.1 Characterization of deuterated host

PYD2Cz and PYD2Cz-d_{16} were synthesized by nucleophilic substitution reaction in *N,N*-Dimethylformamide at 150 ºC (The synthesis processes and characterization are described in Experimental Section), and the chemical structures are shown in **Figure** 2.1. To confirm the deuteration of the materials, IR spectra of PYD2Cz and PYD2Cz-d_{16} were measured as shown in **Figure** 2.2; the peaks of aromatic C-H and C-D stretching can be found in 3042 and 2282 cm^{-1}, respectively. To further confirm the structural packing of the PYD2Cz and PYD2Cz-d_{16}, the single-crystal X-ray diffraction analyses were performed (**Tables** 1, 2 and **Figure** 2.4). Fortunately, the crystal quality was high for both compounds (R = 3.65% for PYD2Cz and 3.63% for PYD2Cz-d_{16}), making the comparison of parameters possible. Thermal properties of PYD2Cz and PYD2Cz-d_{16} were examined by differential calorimetry (DSC) under a nitrogen atmosphere (**Figure** 2.3). On 2nd heating, the thermograms of PYD2Cz and PYD2Cz-

d_{16} both show a glass transition (T_g) at 74.3 and 72.6 ºC, respectively. On further heating, PYD2Cz presents a cold crystallization after the T_g and the compound does finally melt around 221 °C. Interestingly, PYD2Cz-d_{16} did not display cold crystallization and any melting processes in the temperature range of 0–240 ºC. This absence of cold crystallization and melting processes demonstrates the strong amorphous character of PYD2Cz-d_{16} in bulk, and this may be beneficial to the stable device operation even under high temperatures when compared to PYD2Cz.

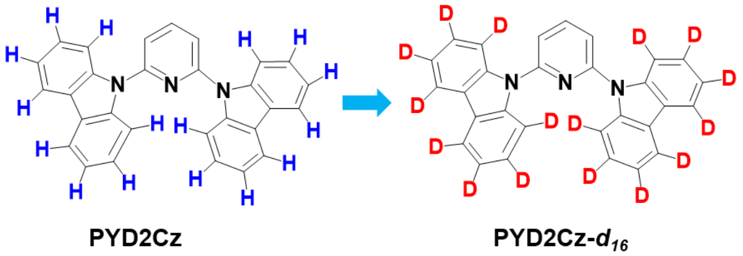

Figure 2.1 Chemical structures of PYD2Cz and PYD2Cz-*d*$_{16}$.

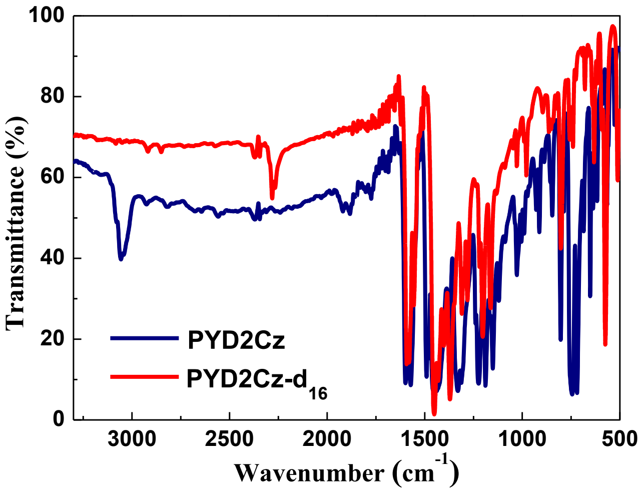

Figure 2.2 IR spectra of PYD2Cz and PYD2Cz-*d*$_{16}$.

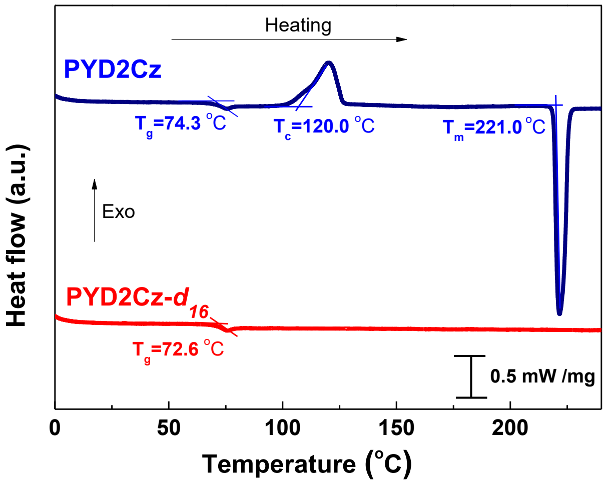

Figure 2.3. DSC curves of PYD2Cz and PYD2Cz-*d*$_{16}$ in 2nd heating, in which T_g, T_c, and T_m are glass transition temperature, cold crystallization temperature, and melting point, respectively.

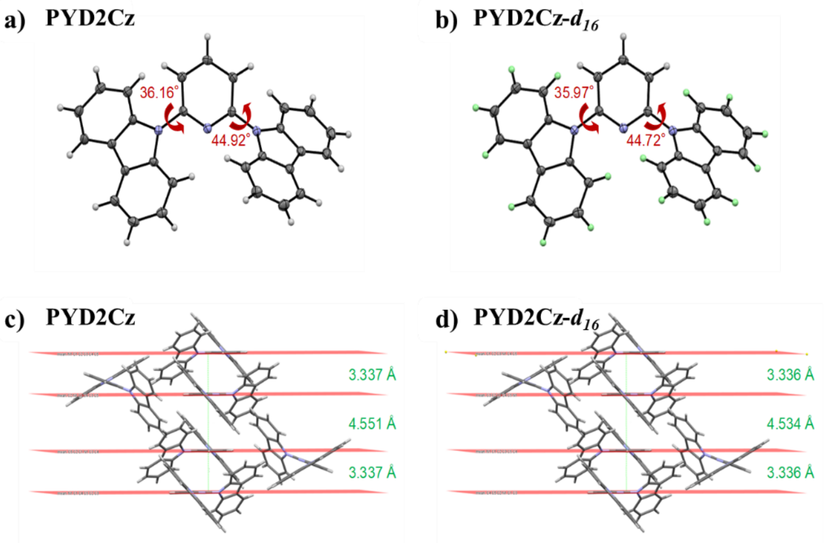

Figure 2.4 Single crystal structures of (a) PYD2Cz and (b) PYD2Cz-*d*$_{16}$. Packing structure and the distance between pyridine rings for (c) PYD2Cz and (d) PYD2Cz-*d*$_{16}$.

Table 2.1 Crystal data for PYD2Cz

Identification code	PYD2Cz
Empirical formula	$C_{29}H_{19}N_3$
Formula weight	409.47
Temperature	100 K
Wavelength	0.71075 Å
Crystal system	Monoclinic,
Space group	$P2_1/c$
Unit cell dimensions	$a = 13.0824(4)$ $\alpha = 90$
	$b = 19.0866(6)$ $\beta = 106.150(4)$
	$c = 8.5518(3)$ $\gamma = 90$
Volume	2051.10(12)
Z	4
Density (calculated)	1.326 g/cm^3
Absorption coefficient	0.079 mm^{-1}
F (000)	856
Crystal size	0.35 × 0.23 × 0.13 mm^3
Theta range for data collection	2.700 to 27.483°.
Index ranges	$-16 <= h <= 16$, $-23 <= k <= 24$, $-11 <= l <= 10$
Reflections collected	23535
Independent reflections	4692 [R(int) = 0.0287]
Completeness to theta = 27.483°	99.84
Absorption correction	Gaussian
Max. and min. transmission	1.000 and 0.556
Refinement method	Full-matrix least-squares on F^2
Data / restraints / parameters	4692 / 0 / 289
Goodness-of-fit on F^2	1.058
Final R indices [I>2sigma(I)]	$R_1 = 0.0365$, $wR_2 = 0.0933$
R indices (all data)	$R_1 = 0.0425$, $wR_2 = 0.0969$
Largest diff. peak and hole	0.275 and −0.256 e.Å^{-3}

Table 2.2 Crystal data for PYD2Cz-d_{16}

Identification code	PYD2Cz-d_{16}	
Empirical formula	$C_{29}H_3D_{16}N_3$	
Formula weight	425.57	
Temperature	100 K	
Wavelength	0.71075 Å	
Crystal system	Monoclinic,	
Space group	$P2_1/c$	
Unit cell dimensions	$a = 13.0807(4)$	$\alpha = 90$
	$b = 19.0973(5)$	$\beta = 106.108(3)$
	$c = 8.5270(3)$	$\gamma = 90$
Volume	2046.47(11)	
Z	4	
Density (calculated)	1.381 g/cm^3	
Absorption coefficient	0.079 mm^{-1}	
$F(000)$	856	
Crystal size	0.339 × 0.25 × 0.077 mm^3	
Theta range for data collection	2.133 to 27.481°.	
Index ranges	−16<=h<=16, −22<=k<=24, −10<=l<=11	
Reflections collected	22080	
Independent reflections	4678 [R(int) = 0.0286]	
Completeness to theta = 27.481°	99.86	
Absorption correction	Gaussian	
Max. and min. transmission	1.000 and 0.669	
Refinement method	Full-matrix least-squares on F^2	
Data / restraints / parameters	4678 / 0 / 289	
Goodness-of-fit on F^2	1.050	
Final R indices [I>2sigma(I)]	$R_1 = 0.0363$, $wR_2 = 0.0911$	
R indices (all data)	$R_1 = 0.0425$, $wR_2 = 0.0949$	
Largest diff. peak and hole	0.260 and −0.261 e.Å^{-3}	

2.2.2 Photophysical properties of H-G system

The ultraviolet-visible (UV-vis) absorption and photoluminescence (PL) spectra of PYD2Cz and PYD2Cz-d_{16} in toluene (10^{-5} M) were depicted in **Figure** 2.5. The absorption and emission spectra of PYD2Cz and PYD2Cz-d_{16} were almost identical. The T_1 energy of PYD2Cz and PYD2Cz-d_{16} was found to be 3.01 and 3.03 eV, respectively, which were determined from the highest energy vibronic peak of their phosphorescence spectra in toluene at 77 K (**Figure** 2.6).

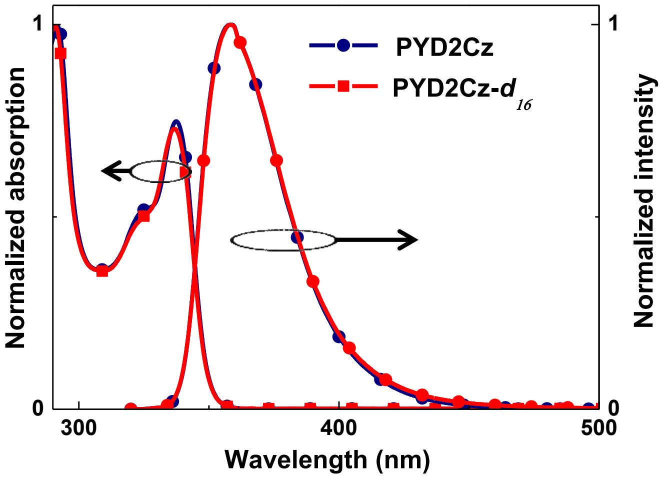

Figure 2.5 Absorption and photoluminescence spectra of PYD2Cz and PYD2Cz-d_{16} in toluene in 298 K (10^{-5} M), respectively.

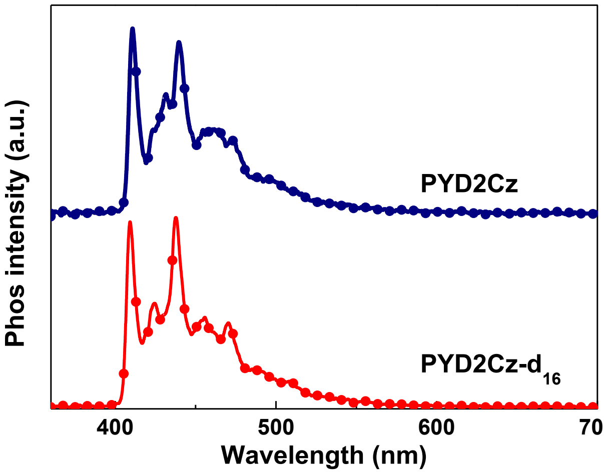

Figure 2.6 Phosphorescent spectra of PYD2Cz and PYD2Cz-d_{16} in toluene solution at 77 K.

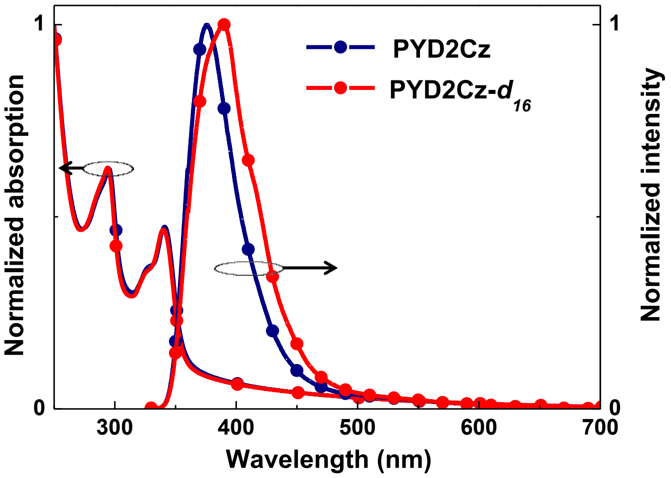

Figure 2.7 Absorption and photoluminescence spectra of PYD2Cz and PYD2Cz-d_{16} in neat films.

The UV-vis absorption spectrum of PYD2Cz-d_{16} in the neat film is as same as that of PYD2Cz, but the PL emission peak of PYD2Cz-d_{16} in the neat film is slightly redshifted by 15 nm (**Figure** 2.7), which indicated that the π-interaction in PYD2Cz-d_{16} in the neat film would be stronger than that of the PYD2Cz film. In fact, the crystal structure analysis revealed a small difference of dihedral angles between pyridine and carbazole rings, and intermolecular distances (**Figure** 2.4).

The HOMO energy levels of PYD2Cz and PYD2Cz-d_{16} were estimated to be –6.05 and –6.07 eV, respectively (**Figure** 2.8). The optical energy gaps were the same for both hosts (3.36 eV), and the LUMO energy levels of PYD2Cz and PYD2Cz-d_{16} were calculated to be –2.69 and –2.71 eV, respectively. The S_1 and T_1 of both hosts were high enough to confine the singlet and triplet excitons of green TADF emitter such as (4s,6s)-2,4,5,6-tetra(9H-carbazol-9-yl)isophthalonitrile (4CzIPN) (T_1 = 2.67 eV, S_1 = 2.71 eV)

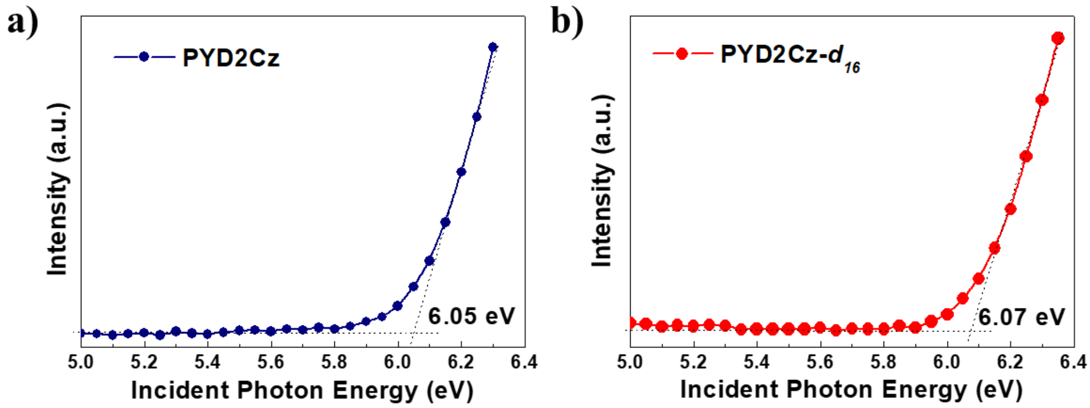

Figure 2.8. Photoelectron yield spectral measurements of (a) PYD2Cz and (b) PYD2Cz-d_{16} neat film under nitrogen atmosphere.

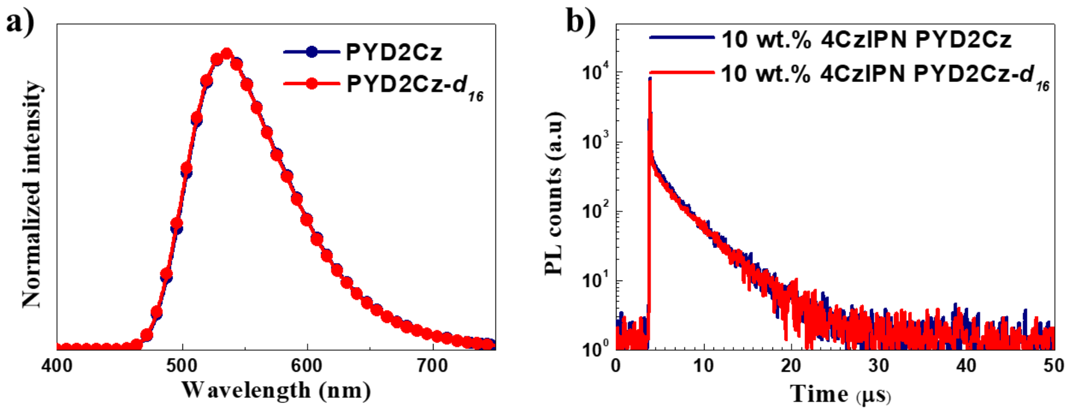

Figure 2.9 a) PL spectra and b) decay curves of vacuum-evaporated doped films with doping concentrations of 10 wt. % of 4CzIPN in PYD2Cz and PYD2Cz-d_{16} hosts at the excitation wavelength of 300 nm.

We then investigated the photophysical properties of vacuum-evaporated thin films of 4CzIPN doped in PYD2Cz and PYD2Cz-d_{16}. With a doping concentration of 10 wt. % of 4CzIPN, both doped films showed identical PL peaks at 534 nm, respectively (**Figure** 2.9a). The transient PL decay curves of both doped films were displayed in **Figure** 2.9b, in which the prompt and delayed components were clearly observed without any noticeable difference in these films, indicating almost no isotope effect on the PL properties in the co-deposited films. The detailed photophysical properties of both materials in solutions and in doped films were summarized in **Tabl**es 2.3 and 2.4. Note that 4CzIPN doped in a PYD2Cz-d_{16} host showed slightly higher photoluminescence quantum efficiency than that of a PYD2Cz host, probably due to the lower vibration energy of C-D.

Table 2.3 Physical properties of PYD2Cz and PYD2Cz-d_{16}.

	Fluo[a] λ_{max} (nm)	Fluo[b] λ_{max} (nm)	Phos[c] λ_{max}(nm)	T_1[d] (eV)	HOMO[e] (eV)	LUMO[f] (eV)
PYD2Cz	359	375	411	3.01	−6.05	−2.69
PYD2Cz-d_{16}	358	390	409	3.03	−6.07	−2.71

[a] Emission peak measured in 10^{-5} M toluene solutions at room temperature; [b] Measured on neat film samples at room temperature; [c] Measured in 10^{-5} M toluene solutions at 77 K; [d] Measure in solution at 77 K; [e] Measured on film samples using Riken-Keiki AC-3; [f] Estimated from the HOMO values and optical band gap.

Table 2.4 Physical properties of PYD2Cz or PYD2Cz-d_{16} doped films (10 wt.% 4CzIPN).

	PL_{max} (nm)	Φ_{PL} (%)	τ_p (ns)	τ_d (μs)	Φ_p (%)	Φ_d (%)	k_{ISC} (10^7 s^{-1})	k_{RISC} (10^6 s^{-1})
PYD-2Cz	534	94	27.4	2.7	20	74	2.87	1.74
PYD2Cz-d_{16}	534	98	27.0	2.8	21	77	2.87	1.69

PL_{max} : Photoluminescence peak; Φ_{PL} : Photoluminescence quantum yield; τ_p : Prompt emission decay lifetime; τ_d : delayed emission decay lifetime; Φ_p : Efficiency of prompt emission; Φ_d : Efficiency of delayed emission; k_{ISC} : intersystem crossing rate; k_{RISC} : reversed intersystem crossing rate.

To evaluate the isotope effect of host material on the device operational stability, green TADF-OLED devices were fabricated with a configuration as follows: ITO /

HAT-CN (10 nm) / tris-PCz (30 nm) / 10 wt. %-4CzIPN: PYD2Cz or PYD2Cz-d_{16} (30 nm) / T2T (10 nm) / BPy-TP2 (40 nm) / LiF (0.8 nm) / Al (70 nm) and details were depicted in **Figure** 2.10. In the device, HAT-CN, tris-PCz, T2T, BPy-TP2, and LiF were used as a hole-injection layer (HIL), a hole transport layer (HTL), a hole blocking layer (HBL), an electron-transporting layer (ETL), and an electron-injection layer (EIL), respectively. The EL spectrum in both devices, i.e., Commission Internationale de l'Éclairage (CIE) x, y coordinates of (0.35,0.59), and (0.36,0.58), were superimposable with their PL spectra, indicating the well-confinement of 4CzIPN excitons in the EMLs (**Figure** 2.11a, b, and c). Although both PYD2Cz and PYD2Cz-d_{16} devices exhibited similar maximum external EL quantum efficiencies (EQEs) of 11.7 % and 12.4 %, respectively, their device stabilities were totally different. The LT_{95} of the device based on PYD2Cz-d_{16} showed enhanced device stability of 134 h as shown in **Figure** 2.11d, which is 1.7-times longer than that of the PYD2Cz-based OLED (LT_{95} = 77 h) at an initial luminance of 1,000 cd m^{-2}. Green devices were evaluated at a constant current density of 1.4 mA cm^{-2}, in which the enhanced device stability was still displayed when PYD2Cz-d_{16} was used as the host material (**Figure** 2.12).

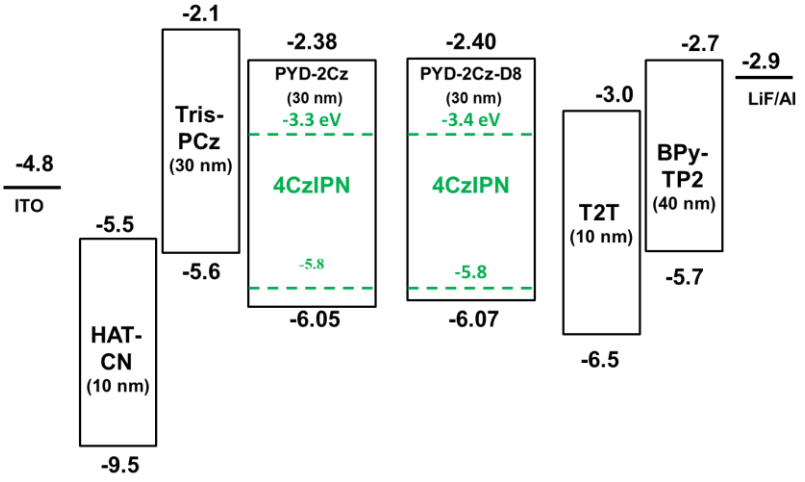

Figure 2.10 Energy level diagram of the fabricated devices.

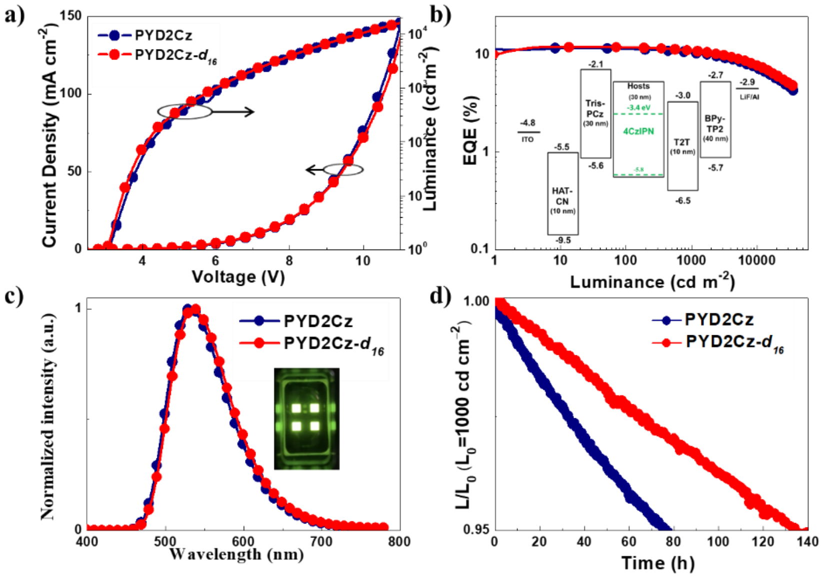

Figure 2.11 Device performance of deuterated PYD2Cz and PYD2Cz-d$_{16}$-based green TADF-OLED devices. a) Current density-voltage-luminance (J-V-L) curves. b) External quantum efficiency versus luminance. c) EL spectra of devices. d) Normalized luminance versus time (at an initial luminance of 1,000 cd m^{-2})

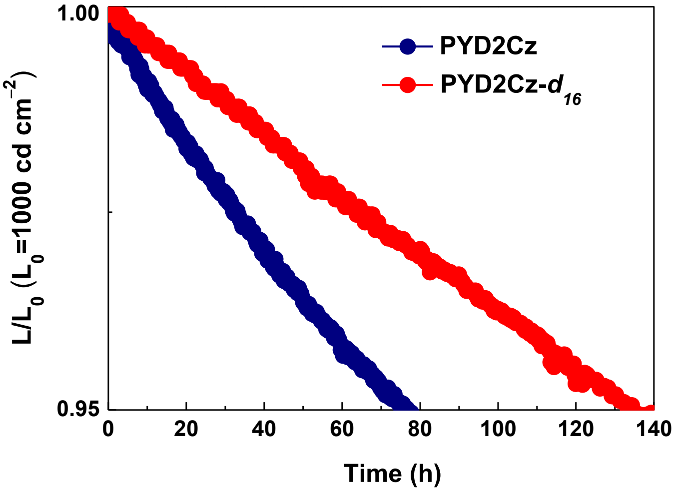

Figure 2.12 Normalized luminance versus time characteristics of PYD2Cz and PYD2Cz-d_{16} based green TADF-OLED devices at a constant current density of 1.4 mA cm^{-2}.

Several factors should be considered to explain the superior device lifetime of PYD2Cz-d16-based OLEDs. For example, it would be probable that PYD2Cz-d_{16} does not seriously aggregate during continuous driving of the OLEDs, even though Joule heating during operation, due to its non-crystallized state at a temperature above the glass transition temperature, which was confirmed both in DSC (**Figure** 2.3). Besides, the more kinetically stable C-D bond in PYD2Cz-d_{16} than the C-H bond in PYD2Cz would be considered as a reason for the enhanced device lifetime. Here, we point out the effect of the isotope substitution in the PYD2Cz on charge transport properties. The HODs and EODs were fabricated by employing two hosts with the device configuration shown in **Figure** 2.13. It was found that the PYD2Cz-d_{16}-based HODs/EODs displayed well-balanced charge transport properties than that of the PYD2Cz-based device. At 12 V, in the PYD2Cz-d_{16}, the ratio of current densities of the EODs to the HODs was close to 1, while it was only 0.12 in the PYD2Cz-based HODs/EODs. To explain this behavior, the thin film densities (ρ) of PYD2Cz and PYD2Cz-d_{16} were determined, and it was founded that the PYD2Cz-d_{16} film (ρ=1.189±0.006 g/cm^3) was denser than the PYD2Cz film (ρ=1.146±0.014 g/cm^3) (**Figure** 2.14 and see experimental section for the detailed experimental method). The difference in the density is not so large, but it has been reported that the slight difference critically affects the carrier transport properties in organic thin films. [18] As the film density increases, the probability of hopping transport between adjacent molecules also increases, thereby improving the carrier transport properties. It is worth noting that the crystal structure data supports a higher density for PYD2Cz-d_{16} due to its smaller volume (**Tables** 2.1 and 2.2). The crystal structures reveal a shorter intermolecular distance between pyridine rings in PYD2Cz-d_{16} compared to PYD2Cz. This shorter distance is believed to facilitate better electron transport, serving as a pathway for enhanced electron mobility. Therefore, the denser thin film of PYD2Cz-d_{16} thus could explain the more balanced carrier transporting properties of PYD2Cz-d_{16}, which was also consistent with the more redshifted PL emission in **Figure** 2.6. The crystal structures indicated a stronger interaction between pyridine rings for PYD2Cz-d_{16} than PYD2Cz, which is considered to be a path for the electron transport (**Figure** 2.4). We suppose that the balanced carrier transporting properties in PYD2Cz-d_{16} resulted in a more broaden recombination zone, hence a better device operational stability.[8]

In addition to the green TADF-OLEDs based on 4CzIPN, we further fabricated blue TADF-OLEDs containing an EML of 10 wt.%-penta(9H-carbazol-9-yl)benzonitrile (5CzBN) emitter in a PYD2Cz or PYD2Cz-d_{16} host. The device configuration is shown in the inset of **Figure** 2.15b. The device performance is summarized in **Figure** 2.15. Similar to the green TADF-OLEDs, both PYD2Cz and PYD2Cz-d_{16}-based OLEDs showed identical emission peak maxima of 491 nm and similar maximum EQEs of 9.1 and 11.2 %, respectively.

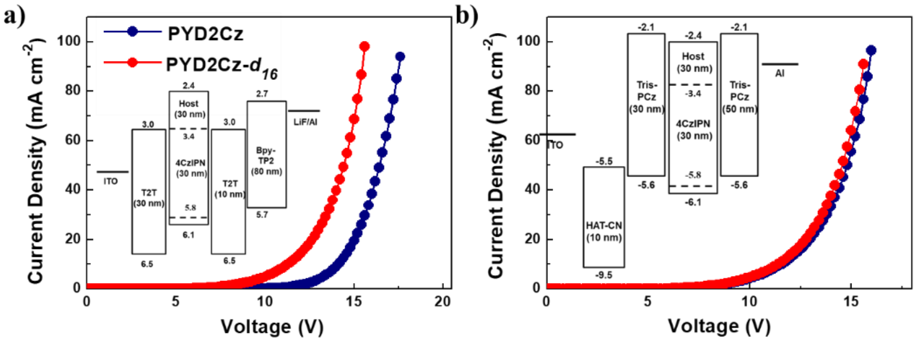

Figure 2.13 Current density – Voltage (J-V) characteristics of a) EODs and b) HODs for PYD2Cz and PYD2Cz-d_{16} doped with 10 wt. % 4CzIPN. Inset: energy diagram of a) EODs and b) HODs.

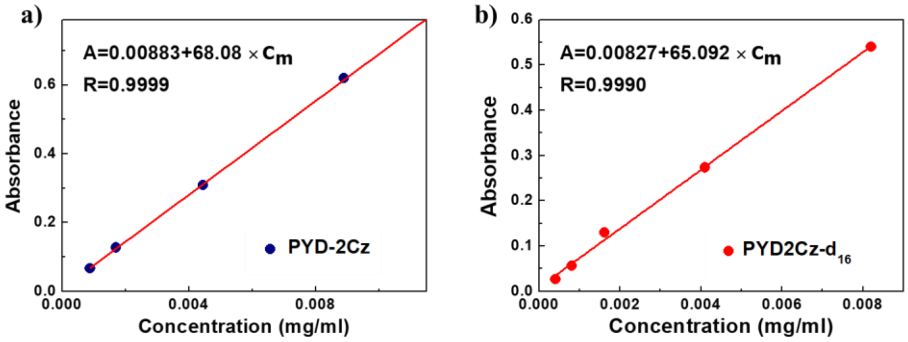

Figure 2.14. Calibration curves of absorption coefficient against concentration of (a) PYD2Cz and (b) PYD2Cz-d_{16} in toluene, respectively.

Nonetheless, two-fold enhanced device stability (LT_{50} at an initial luminance of 1,000 cd m^{-2}) was found (improved from 17 h to 40 h) when PYD2Cz-d_{16} was used as the host material. Meanwhile, it was noted that the current densities for the two devices are different at 1,000 cd m^{-2}. Therefore, the device stabilities of both blue devices were evaluated at a constant current density of 5.4 mA cm^{-2}, in which enhanced device stability was still displayed when PYD2Cz-d_{16} was used as the host material (**Figure** 2.16). These proved that deuterated host PYD2Cz-d_{16}, which has a high T_1 level with well-balanced charge carrier transport ability, is considered to be a potential candidate as a universal host for TADF-OLEDs to enhance the device operational stability.

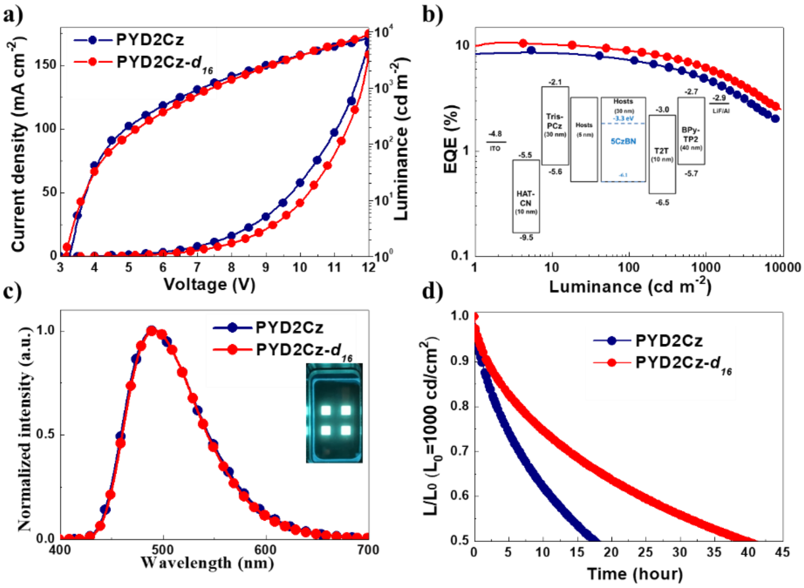

Figure 2.15. Device performance of PYD2Cz and deuterated PYD2Cz-d_{16}-based blue TADF-OLEDs. a) Current density-voltage-luminance (J-V-L) curves. b) External quantum efficiency versus luminance. Inset: Energy level diagram of the fabricated devices. c) EL spectra of devices. d) Normalized luminance versus time (at an initial luminance of 1,000 cd m^{-2})

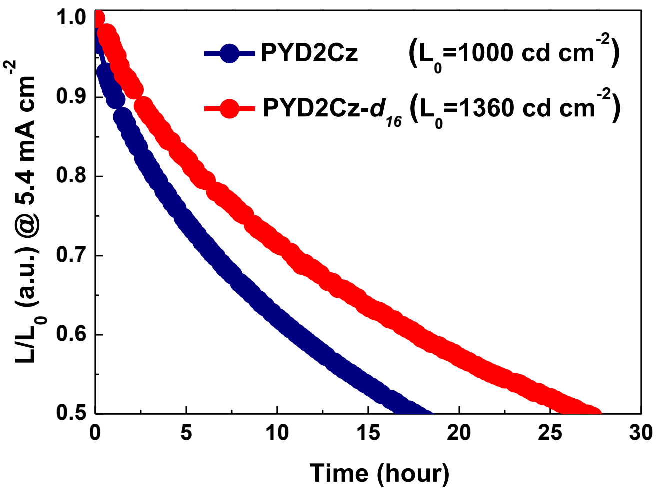

Figure 2.16. Normalized luminance versus time characteristics of PYD2Cz and PYD2Cz-d_{16} based blue TADF-OLEDs at a constant current density of 5.4 mA cm^{-2}.

2.3 Summary

In conclusion, we revealed the isotopic effect of host materials, i.e., PYD2Cz and PYD2Cz-d_{16}, on the OLED performances in the TADF-OLEDs. Although the photophysical properties of both hosts are almost identical, it was found that the physical properties of hosts in the thin film states were appreciably different. The deuterated host (PYD2Cz-d_{16}) showed non-crystalline and densely packed behaviors in a film state that was different from the non-deuterated host of PYD2Cz. Moreover, green TADF-OLEDs based on PYD2Cz-d_{16} displayed more balanced carrier transporting properties than that of PYD2Cz, which resulted in better device stability with a 1.7-times longer in LT$_{95}$ of 134 h at an initial luminance of 1,000 cd m^{-2}. The enhancement of the device operation lifetime by the deuterated host was also confirmed in the blue TADF-OLEDs. Our work could provide the explanations for why the hydrogen/deuterium isotope effect improves the stability of OLEDs in view of thermal and carrier transport properties. We, thus, believe that our study would give insight into achieving stable TADF/Ph/fluorescence-OLEDs through the deuteration of organic functional materials.

2.4 Experimental Section

2.4.1 Material and characterization

PYD2Cz was purchased from Lumtec. Corp. All reagents were used as received from commercial sources and were used without further purification. Chromatographic separations were carried out using silica gel (200–300 nm). The two materials investigated in this paper were synthesized by following the procedures described below. PYD2Cz and PYD2Cz-*d16* were purified twice by temperature gradient vacuum sublimation. ^{1}H nuclear magnetic resonance (NMR) spectra were obtained in CD_2Cl_2 with a Bruker Biospin Avance-III 500 NMR spectrometer at ambient temperature. Chemical shifts (δ) are given in parts per million (ppm) relative to tetramethylsilane (TMS; δ = 0) as the internal reference. Mass spectra were measured in positive-ion atmospheric-pressure chemical ionization (APCI) mode on a Waters 3100 mass detector. The purity of PYD2Cz-*d16* was confirmed by the high-performance liquid chromatography (HPLC) method. The experimental condition of HPLC is as follows; Column: InertSustain C18 (2.1 mm × 150 mm), Carrier: Acetonitrile: water = 83: 17, Rate: 0.2 ml/min, Temperature: 40 °C, Det.: 254 nm. AFM images of PYD2Cz and PYd2Cz-*d16* neat film were investigated by tapping mode AFM (nGauge AFM).

Scheme-1: PYD2Cz-*d16*

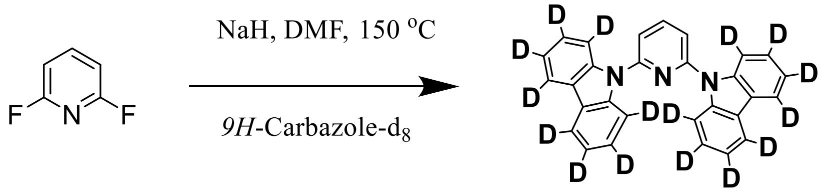

PYD2Cz-d_{16}

Under nitrogen atmosphere, 9*H*-carbazole-d_8 (2 mmol) was dissolved in dry *N*,*N*-dimethylformamide (30 mL) in a two-neck round-bottom flask equipped with a condenser. The reaction mixture was cooled to 0 °C, then NaH (2 mmol) was added. The reaction mixture was slowly warmed to room temperature and stirred for half an hour. After that, 2,6-difluoropyridine (1 mmol) was added and the reaction was heated to 150 °C for 16 hours. The reaction was quenched with water and the precipitate was filtered off. The crude product was purified by column chromatography. Yield: 341 mg (80%). ^{1}H NMR (500 MHz, CD_2Cl_2, 298 K, relative to Me_4Si): $\delta = 8.24$ (t, 1H, $J =$ 8Hz), 7.72 (d, 2H, $J = 8$ Hz). MS (APCI) calcd. For $C_{29}H_3D_{16}N_3$: m/z = 425.8; found: 426.4 $[M]^+$. Purity (HPLC): 99.74%.

Thermal gravimetry-differential thermal analysis (TG-DTA) was performed by Bruker TG-DTA 2400SA with a heating rate of 10 ºC min^{-1} under nitrogen atmosphere. Differential scanning calorimetry (DSC) analysis was performed by Netzsch DSC204 Phoenix calorimeter at a scanning rate of 5 °C min^{-1} under N_2 atmosphere.

X-ray diffraction data for PYD2Cz and PYD2Cz-d_{16} were collected on a Rigaku AFC HyPix-6000 diffractometer with Mo-Kα radiation ($\lambda = 0.71075$ Å) at 100 K. Single crystals suitable for X-ray analysis were grown by sublimation. The sublimation zone temperature was set at 200 °C and the constant flow of pure nitrogen carrier gas with the pressure was kept at 0.1 bar. After 24 h plate-like crystals were formed in the crystallization zone. Data collection, cell refinement, and data reduction were carried out using the software CrysAlisPro. The structure was solved by direct methods using the program SHELXT and refined by full-matrix least squares methods on F^2 using SHELXL-2014.[23] All materials for publication were prepared using the software Olex2.[24] All non-hydrogen atoms were refined anisotropically. The positions of all hydrogen atoms were calculated geometrically and refined as a riding model. Crystallographic data have been deposited with Cambridge Crystallographic Data Centre (CCDC): Deposition numbers CCDC 2036278-2036279. Copies of the data can be obtained free of charge via http://www.ccdc.cam.ac.uk/conts/retrieving.html.

2.4.2 Photophysical measurements

Toluene solutions containing two materials (10^{-5}M) were prepared to investigate their absorption and photoluminescence characteristics in the solution state. Thin-film samples (10% wt- doped in mCBP) were deposited on quartz glass substrates by vacuum evaporation to study their exciton confinement properties in the film state. Ultraviolet–visible absorption (UV-vis) and photoluminescence (PL) spectra were recorded on a Perkin-Elmer Lambda 950 KPA spectrophotometer and an FP-6500 fluorescence spectrophotometer. Phosphorescent spectra were recorded on a JASCO FP-6500 fluorescence spectrophotometer at 77 K. The optical energy gaps (S_1) are determined from the absorption edges of thin films. A UV photoelectron emission spectrometer (Riken Keiki AC-3) was used to determine the HOMO energy levels of the compounds in the neat films. Absolute PL quantum yields were measured on a Quantaurus-QY measurement system (C11347-11, Hamamatsu Photonics) under nitrogen flow and all samples were excited at 360 nm. The transient PL decay characteristics of solution and doped film samples at room temperature were recorded using a Quantaurus-Tau fluorescence lifetime measurement system (C11367-03, Hamamatsu Photonics). FT-IR spectra were measured using the KBr pellet method on a JASCO FT/IR-6000 infrared spectrophotometer.

2.4.3 Device fabrication and measurements

The OLEDs were fabricated by vacuum deposition process without exposure to ambient air. After fabrication, the devices were immediately encapsulated with glass lids using epoxy glue in a nitrogen-filled glove box (O_2~0.1ppm, H_2O~0.1ppm). The indium–tin oxide surface was cleaned ultrasonically and sequentially with acetone, isopropanol and deionized water, then dried in an oven, and finally exposed to ultraviolet light and ozone for about 10 min. Organic layers were deposited at a rate of 1 Å/s. Subsequently, Liq and Al were deposited at 0.3 and 1 Å/s, respectively. The device area is ~ 0.04 cm^2. The EQE and *J-V-L* measurements were performed using a Keithley 2400 source meter and an absolute external quantum efficiency (EQE) measurement system (C9920-12, Hamamatsu Photonics, Japan). For the device lifetime tests, the luminance and EL spectra of the driving devices in the normal direction were measured using a luminance meter (SR-3AR, TOPCON, Japan) under constant current density driving conditions with an initial luminance of 1000 cd m^{-2}.

2.4.4 Thin film density measurement

The measurement method for film density is based on a previous report.[25] Neat films of PYD2Cz and PYD2Cz-d_{16} deposited on Si substrate (~500 nm), the thicknesses of the neat films were determined using Variable angle spectroscopic ellipsometry (VASE). After that, the neat films were dissolved in 5 ml toluene and absorption spectra were measured with a spectrometer (LAMBDA 950, PerkinElmer). Comparing the absorbance with the calibration curves in Fig. S9, the film densities were calculated by dividing the mass by the volume.

2.5 References

1. Mikhnenko, O.V., Blom, P.W. & Nguyen, T.-Q. Exciton diffusion in organic semiconductors. *Energy Environ. Sci.* **8**, 1867-1888 (2015).
2. Reineke, S. et al. White organic light-emitting diodes with fluorescent tube efficiency. *Nature* **459**, 234-238 (2009).
3. Endo, A. et al. Efficient up-conversion of triplet excitons into a singlet state and its application for organic light emitting diodes. *Appl. Phys. Lett.* **98**, 42 (2011).
4. Goushi, K., Yoshida, K., Sato, K. & Adachi, C. Organic light-emitting diodes employing efficient reverse intersystem crossing for triplet-to-singlet state conversion. *Nat. Photon.* **6**, 253-258 (2012).
5. Uoyama, H., Goushi, K., Shizu, K., Nomura, H. & Adachi, C. Highly efficient organic light-emitting diodes from delayed fluorescence. *Nature* **492**, 234-238 (2012).
6. Wong, M.Y. & Zysman-Colman, E. Purely organic thermally activated delayed fluorescence materials for organic light-emitting diodes. *Adv. Mater.* **29**, 1605444 (2017).
7. Chan, C.-Y., Tanaka, M., Nakanotani, H. & Adachi, C. Efficient and stable sky-blue delayed fluorescence organic light-emitting diodes with CIEy below 0.4.

Nat. Commun. **9**, 5036 (2018).

8. Nakanotani, H., Masui, K., Nishide, J., Shibata, T. & Adachi, C. Promising operational stability of high-efficiency organic light-emitting diodes based on thermally activated delayed fluorescence. *Sci. Rep.* **3**, 2127 (2013).
9. Noda, H., Nakanotani, H. & Adachi, C. Excited state engineering for efficient reverse intersystem crossing. *Sci. Adv.* **4**, eaao6910 (2018).
10. Chatterjee, T. & Wong, K.T. Perspective on host materials for thermally activated delayed fluorescence organic light emitting diodes. *Adv. Opt. Mater.* **7**, 1800565 (2019).
11. Cui, L.-S. et al. Long-lived efficient delayed fluorescence organic light-emitting diodes using n-type hosts. *Nat. Commun.* **8**, 2250 (2017).
12. Ihn, S.G. et al. An Alternative Host Material for Long-Lifespan Blue Organic Light-Emitting Diodes Using Thermally Activated Delayed Fluorescence. *Adv. Sci.* **4**, 1600502 (2017).
13. Lee, J. et al. Hot excited state management for long-lived blue phosphorescent organic light-emitting diodes. *Nat. Commun.* **8**, 15566 (2017).
14. Zhang, Y., Lee, J. & Forrest, S.R. Tenfold increase in the lifetime of blue phosphorescent organic light-emitting diodes. *Nat. Commun.* **5**, 5008 (2014).
15. Tsuji, H., Mitsui, C. & Nakamura, E. The hydrogen/deuterium isotope effect of the host material on the lifetime of organic light-emitting diodes. *ChemComm.* **50**, 14870-14872 (2014).
16. Wang, P. et al. Synthesis of all-deuterated tris (2-phenylpyridine) iridium for highly stable electrophosphorescence: The “deuterium effect”. *J. Mater. Chem. C* **1**, 4821-4825 (2013).
17. Gomez-Gallego, M. & Sierra, M.A. Kinetic isotope effects in the study of organometallic reaction mechanisms. *Chem. Rev.* **111**, 4857-4963 (2011).
18. Esaki, Y., Komino, T., Matsushima, T. & Adachi, C. Enhanced electrical properties and air stability of amorphous organic thin films by engineering film density. *J. Phys. Chem.* **8**, 5891-5897 (2017).

Chapter 3

Impact of band alignment on the performance of organic-inorganic hybrid system

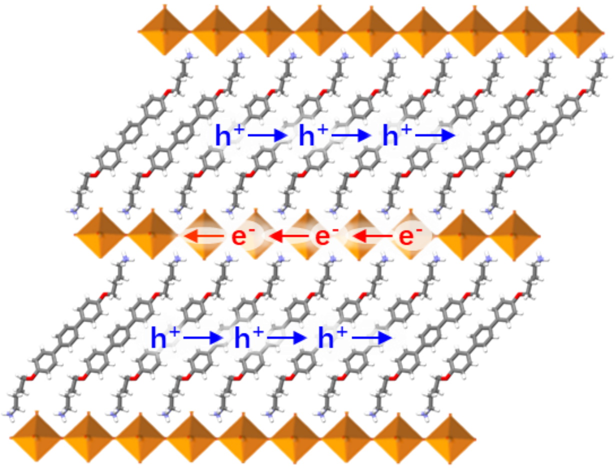

Chapter 3: Impact of band alignment on the performance of organic-inorganic hybrid system

3.1 Introduction

In the previous chapter, we delved into the organic-organic H-G system for light emission application. The use of a deuterated H-G system has been shown to result in more balanced carrier transport properties, leading to enhanced stable OLEDs. This work highlighted the crucial role of balancing carrier transport in determining the performance of the H-G system for practical application. It is well-known that inorganic materials exhibit much higher and more balanced carrier mobilities compared to conventional amorphous organic thin films. For instance, perovskite materials have been demonstrated to have not only high carrier mobility but also balanced hole and electron mobilities[1]. The previous research by Matsushima et al.[2] has demonstrated the excellent carrier transport properties of perovskite materials, leading to its use as a host material in a hybrid inorganic-organic H-G system. The system holds great potential for enhancing the performance of OLEDs. However, in such a system, the organic emitters are often dispersed randomly between the inorganic grain boundaries, making it prone to induce phase separation between organic and inorganic components, ultimately leading to poor device performance. To address this issue and fully leverage the advantages of perovskites, the organic guest molecules should ideally incorporate themselves as a part of the crystalline structure, rather than merely disperse on the boundaries in the inorganic-organic hybrid system. This would help prevent phase separation and ensure optimal use of perovskite's unique characteristics as a hybrid material containing both organic and inorganic components.

This chapter presents the synthesis of a hybrid perovskite with an inorganic-organic hybrid system in a 2D perovskite structure, consisting of inorganic monolayers of metal-halide octahedra separated by organic 4,4'-([1,1':4',1''-terphenyl]-4,4''-diylbis(oxy))bis(butan-1-aminium)dibromide (M1). Our study focuses on investigating the band alignment effect on this hybrid structure and exploring its electronic and photophysical properties using experimental and theoretical investigations. Furthermore, we probed the charge transport properties of this hybrid structure using hole-only and electron-only devices (HODs/EODs). Our findings demonstrate that this hybrid perovskite material presents two intercalated separate pathways for electrons and holes, which can migrate within the inorganic and organic sublayers, respectively. The results of this study provide insights into the band alignment effect on the inorganic-organic hybrid system, which is of paramount importance for future optoelectronic applications.

3.2 Results and Discussion

3.2.1 Synthesis and structure analyses of hybrid system

As a first step, the terphenyl-based diammonium organic cation M1 (**Figure** 3.1a) was designed and synthesized via the synthetic route given in the experimental section. The hybrid thin film of M1/PB was prepared by the typical one-step spin-coating method from the precursor solutions with a 1:1 ratio between the diammonium salt M1 and $PbBr_2$ (see experimental section). The structure of the obtained thin film was investigated by X-ray diffraction (XRD) and Grazing-incidence wide-angle X-ray scattering (GIWAXS) measurements. As shown in **Figure** 3.1b, the X-ray pattern shows a series of intense, sharp, and equidistant reflections corresponding to the (*h*00) spacing of the 2D layered perovskite structure, indicating a long-range lamellar order with high crystallinity. This pattern is also clearly different from those of the M1 and $PbBr_2$ neat films (**Figure** 3.2), confirming the formation of a new 2D perovskite phase with an interlayer *d*-spacing of 22.3 Å. The GIWAXS pattern corroborates the lamellar structure of M1/PB and, more importantly, confirms the preferential orientation of the lamellae, parallel to the substrates in the spin-coated films as shown by the exclusive concentration of the lamellar reflections on the pattern meridian and the vertical distribution of the other (*hkl*) reflection series (**Figure** 3.1c).

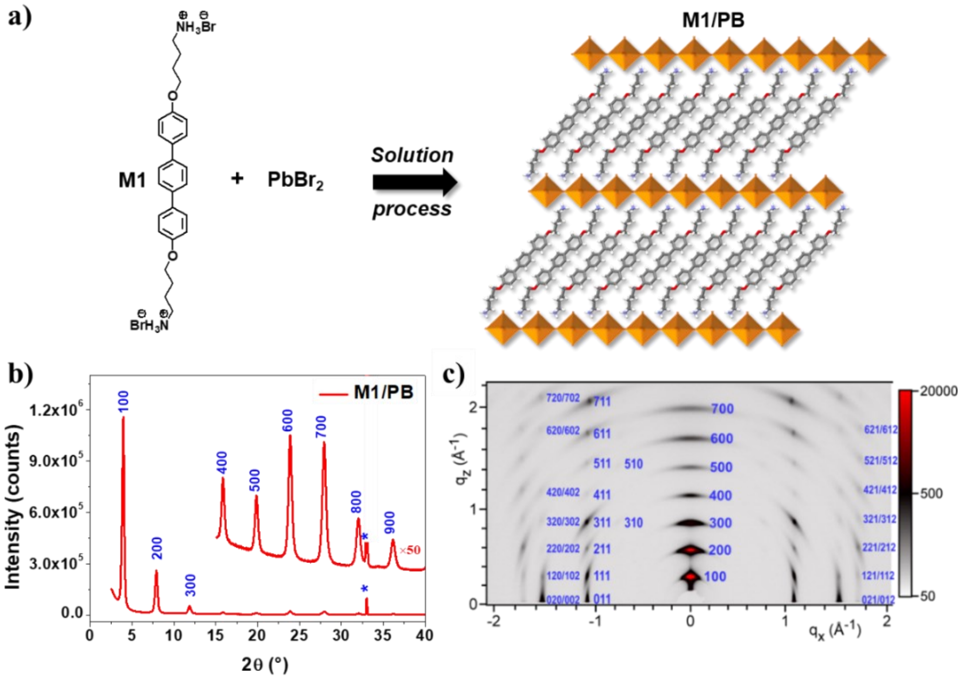

Figure 3.1. 2D M1/PB perovskite: (a) Chemical structure of M1 and schematic representation of M1/PB structure. (b) X-ray diffraction pattern of M1/PB thin films. (The blue labels on the top of peaks indicate their Miller indices and the sharp peak at 33° is the signature of the silicon substrate). (c) GIWAXS patterns of M1/PB film. (The blue labels on the right of spots indicate their Miller indices)

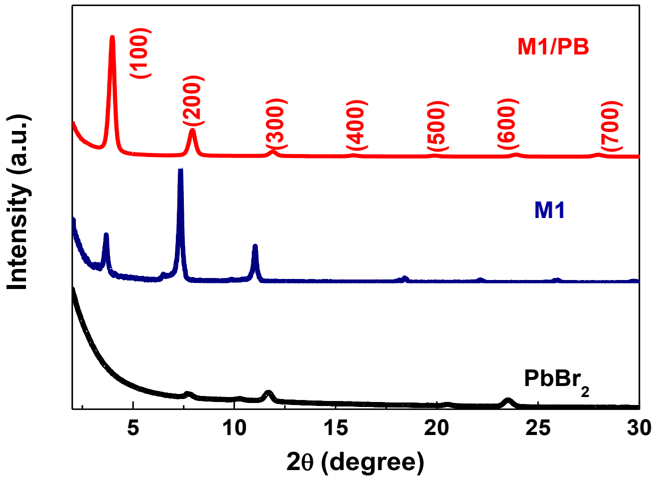

Figure 3.2. X-ray diffraction pattern of M1/PB thin films compared to M1 and PbBr$_2$ films.

The absorption spectrum of the hybrid M1/PB thin film (**Figure** 3.3) exhibits a sharp excitonic absorption peak at 401 nm, firmly evidencing the formation of the 2D perovskite structure. [3] Additionally, the absorption spectrum of hybrid M1/PB presents a strong absorption band at around 300 nm principally originating from the M1 organic salt. These results confirmed that an organic M1 layer was successfully incorporated into the perovskite lattice as the organic spacer.

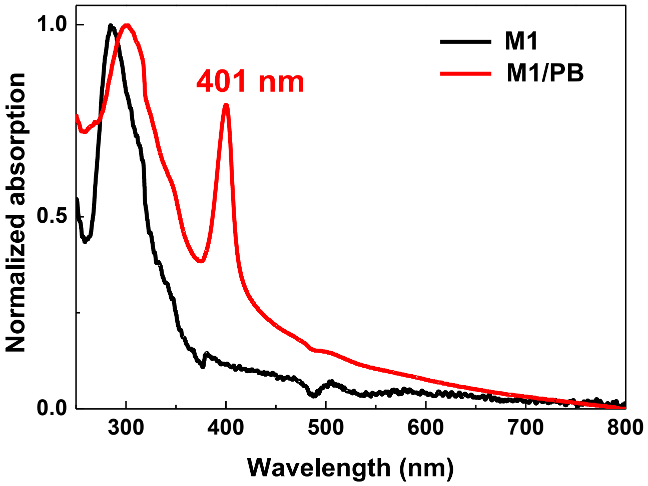

Figure 3.3. UV-vis absorption spectra of the diammonium organic salt M1 and hybrid M1/PB neat films.

The stability of this novel hybrid system was also considered in view of practical applications. In this regard, a thin film of M1/PB was continuously exposed to an ambient environment and its degradation was monitored by XRD. As a result, the hybrid 2D perovskite showed very good stability, since no decrease of the first-order diffraction peak was observed in the XRD patterns, even after a few months of exposure to air (**Figure** 3.4). To gain a better insight into the structure of M1/PB, the single crystals with the size of several hundred micrometers were grown by the anti-solvent diffusion method as described in Experimental section. The optical image of a typical platelet-like M1/PB crystal is shown in **Figure** 3.5. The structure of this large and thin crystal was determined by single-crystal X-ray diffraction and it confirms the layered organization of hybrid M1/PB consisting of inorganic $PbBr_4$ monolayers separated by

M1 monolayers (**Figure** 3.6). The structure is monoclinic and belongs to the $P2_1/c$ space group, with the lattice parameters a, b, and c which are equal to 22.1620(5) Å, 8.1266(2) Å, and 8.1029(2) Å, respectively, and β = 90.156(2)°. The terphenyl-based organic cation M1 clearly shows herringbone packing with a tilted angle of about 43° with respect to the inorganic $PbBr_4$ monolayer (**Figures** 3.7 and 3.8). This organization is close to that of other 2D perovskites incorporating large diammonium organic cations.[4, 5] The additional detailed crystallographic data and parameters of the M1/PB structure are summarized in **Table** 3.1.

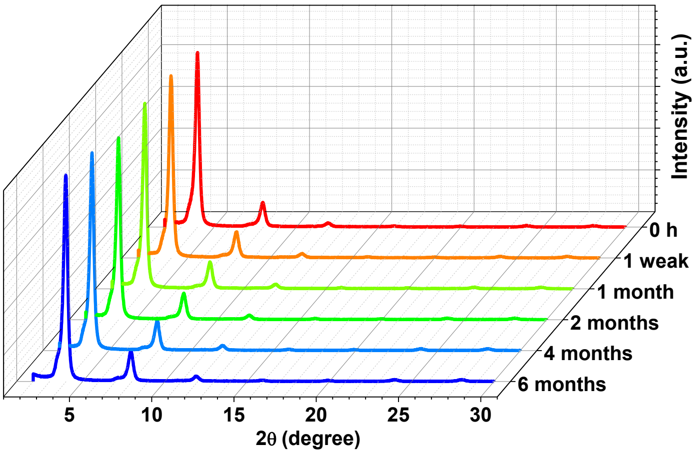

Figure 3.4 Stability measurement of M1/PB perovskite film exposed to air environment (ambient condition) monitored by XRD.

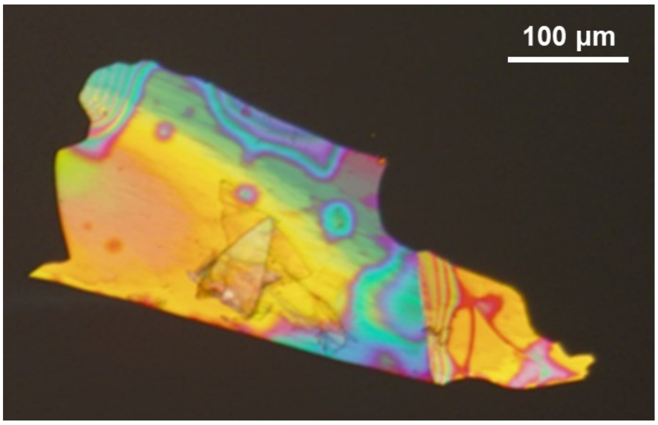

Figure 3.5. Optical image under crossed polarizers of M1/PB single crystal.

Table 3.1. Crystal data and structure refinement for M1/PB.

Identification code	M1/PB
Empirical formula	$C_{26}H_{34}Br_4N_2O_2Pb$
Formula weight	933.38
Temperature/K	200.0
Crystal system	monoclinic
Space group	$P2_1/c$
a/Å	22.1620(5)
b/Å	8.1266(2)
c/Å	8.1029(2)
α/°	90
β/°	90.1564(12)
γ/°	90
Volume/$Å^3$	1459.34(6)
Z	2
$\rho_{calc}g/cm^3$	2.124
μ/mm^{-1}	17.859
F(000)	884.0
Crystal size/mm^3	0.11 × 0.08 × 0.02
Radiation	CuKα (λ = 1.54178)
2Θ range for data collection/°	7.978 to 136.764
Index ranges	$-26 \leq h \leq 26$, $-9 \leq k \leq 9$, $-9 \leq l \leq 8$
Reflections collected	15229
Independent reflections	2656 [$R_{int} = 0.0499$, $R_{sigma} = 0.0412$]
Data/restraints/parameters	2656/0/162
Goodness-of-fit on F^2	1.070
Final R indexes [I>=2σ (I)]	$R_1 = 0.0308$, $wR_2 = 0.0843$
Final R indexes [all data]	$R_1 = 0.0334$, $wR_2 = 0.0857$
Largest diff. peak/hole / e $Å^{-3}$	1.32/-0.97

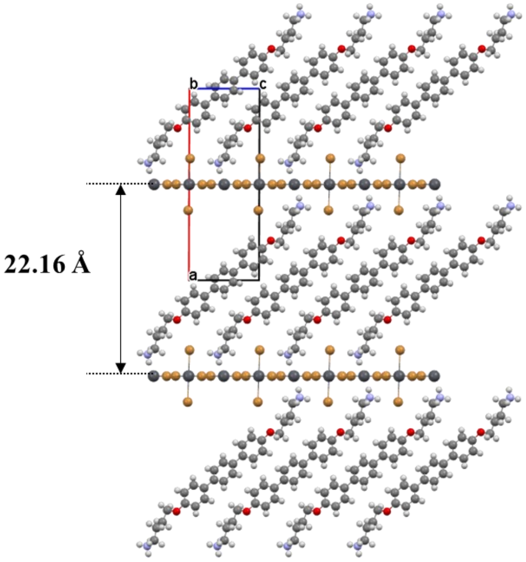

Figure 3.6 Crystal structure of 2D M1/PB.

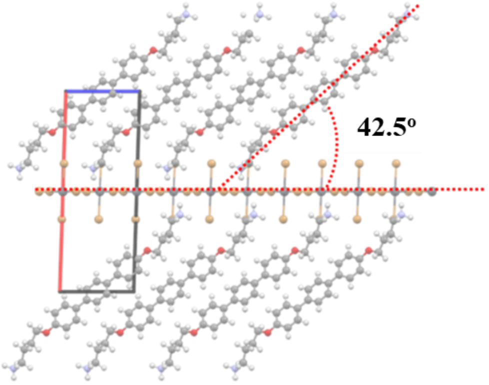

Figure 3.7 Inclination of the organic diammonium salt M1 compared to the inorganic plane in the M1/PB crystal structure.

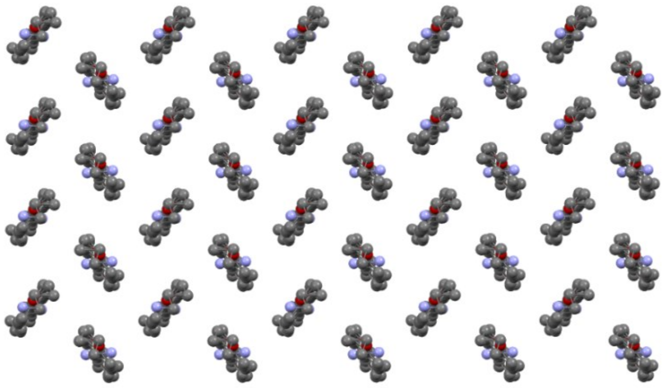

Figure 3.8 Top view of the molecular packing of terphenyl-based organic salt M1 within the organic monolayer in M1/PB crystal structure.

To have more information on the orientation of the crystallographic axes and unit cells within the crystal, we performed topographic atomic force microscopy (AFM) measurements on the top of the platelet-like M1/PB single crystal (**Figure** 3.9a). Not surprisingly, the crystal surface shows very large flat and smooth domains (above micrometric scale), and only a few "molecular" steps of around 2.2 nm were observed in good agreement with the lamellar periodicity measured by XRD and GIWAXS on M1/PB thin films. These results clearly show that the longest axis of the unit cell is perpendicular to the larger facets of the crystal, corresponding to the smallest dimension of the platelet, while the *b* and *c* axes are in the plane of the crystal. Consequently, the layered structure of M1/PB is oriented parallel to the larger facets of the crystal and the layers formed by the herringbone packing of the terphenyl units are in the plane of the platelet-like crystals (**Figure** 3.9b).

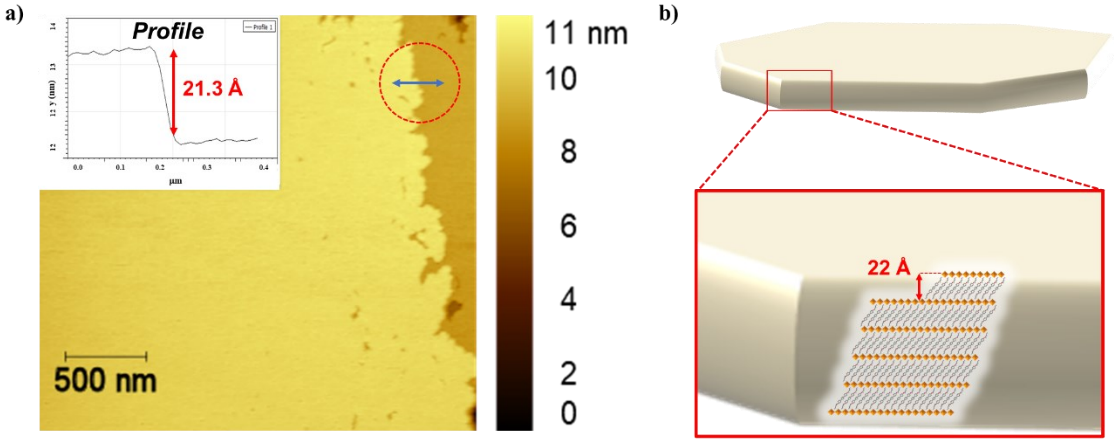

Figure 3.9. (a) Topography AFM images of M1/PB 2D perovskite single crystal. The terraces were measured with a height of 21.3 Å. (b) Schematic representation of the M1/PB layered structure orientation within the platelet-like crystals; The organic and inorganic layers are oriented in the plane of the crystal.

The hybrid M1/PB thin films maintain the same structure as the single crystal with nearly unchanged lattice parameters (a = 22.2 ± 0.1 Å, $c \approx b$ = 8.15 ± 0.3 Å, β = 90.5 ± 0.5°), as determined from GIWAXS and in agreement with the lamellar periodicity from the out-of-plane XRD ($d \approx a$ = 22.3 Å). Here, the tiny variation can be explained by the different measurement temperatures (200 K for single crystal and room temperature for thin films) and by a possible influence of sample fabrication. The thin film morphology revealed by GIWAXS consists of a mosaic of crystallites, which are oriented with the (*b*,*c*)-plane parallel to the substrate and of roughly 20 nm in-plane size, as deduced from (111) spot width by using the Scherrer equation with shape factor $K = 0.9$.

3.2.2 Energy band structures and charge-carrier dynamics

Previous reports indicated that the band alignment formed by organic and inorganic layers is one of the key parameters for tuning the optical and electrical properties of 2D hybrid perovskite materials.[2,9] Therefore, we measured the highest occupied molecular orbital energy level (HOMO) and lowest unoccupied molecular orbital (LUMO) for organic M1 and hybrid M1/PB perovskite films by photoelectron spectroscopy (PES) and low-energy inverse photoemission spectroscopy (LEIPS), respectively. The LUMO of M1 and M1/PB layers were measured to be -2.50 eV and -2.66 eV, respectively, suggesting that the measured energy level in M1/PB by LEIPS corresponds to the conduction band of the inorganic perovskite monolayer. The HOMOs of M1 and M1/PB layers were estimated to be -5.94 eV and -5.97 eV, respectively, as shown in **Figures** 3.10a and 3.10b. The HOMO and LUMO energy levels are summarized in **Table** 3.2. Based on these similar values, it is difficult to determine the accurate band alignment between organic M1 and the inorganic sublayer. Therefore, to clearly identify the roles of organic spacers and inorganic layers in the band alignment, we studied the electronic properties of M1/PB by density functional theory (DFT) calculations (See more computational details in the Experimental section). We first validate the calculation for M1/PB based on its crystal structure (**Table** 3.1). The predicted lattice parameters by DFT with Perdew-Burke-Ernzerhof (PBE) functional and D3 dispersion correction are in good agreement with the XRD experimental values, where the deviation is within 1.7% or lower (**Table** 3.3) and most likely caused by the temperature. [6]

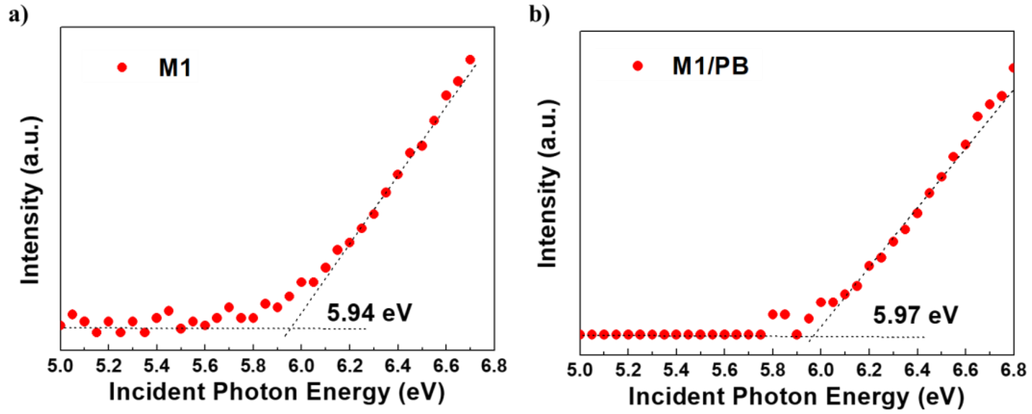

Figure 3.10 PES of a) M1 organic ligand and b) 2D M1/PB perovskite films.

Table 3.2 Summary of HOMO and LUMO energy levels of (BA)$_2$PbBr$_4$, M1, and 2D M1/PB neat films by PES and low-energy inverse photoemission LEIPS) spectroscopy methods.

Compound	PES	LEIPS
	HOMO (eV)	LUMO (eV)
(BA)$_2$PbBr$_4$	-6.08	-2.78
M1 salt	-5.94	-2.50
M1/PB	-5.97	-2.66

Table 3.3 Lattice parameters of M1/PB extracted from experimental (XRD) and DFT (PBE+D3) relaxed structures.

	a (Å)	*b* (Å)	*c* (Å)	*α* (°)	*β* (°)	*γ* (°)
Experimental	22.1620	8.1266	8.1029	90	90.156	90
DFT	21.9031	8.1281	8.1003	90.000	91.718	90.000

Then, the band structure was computed from this optimized M1/PB configuration. In addition to the PBE + D3 method, the spin-orbit coupling (SOC) effect was also included to account for the relativistic effect in the Pb and Br p orbitals (**Figure** 3.11 and **Figure** 3.12). [7] The valence band maximum (VBM) and conduction band minimum (CBM) are plotted with different colors in **Figure** 3.11b and a direct band gap can be observed at the Ί point. Consistently with the PES and LEIPS measurements, these calculations confirm that the terphenyl dications act as a donor of electrons and that the inorganic layers contribute exclusively to the CBM. They also demonstrate that the valence band of the inorganic $PbBr_4$ layer is deeper than the HOMO of the M1 layer (**Figure** 3.13), leading to a rare example of type IIb heterostructure, a particular case of the type II band alignment in which electrons and holes can localize on inorganic and organic sublayers, respectively. [8-11] To visualize the orbital contributions to VBM and CBM, the corresponding wavefunction was extracted and displayed in **Figure** 3.14. This representation distinctly shows the localization of the VBM on the π-conjugated aromatic core of M1 units while lead and bromine orbitals contribute to the CBM. Based on the previous reports, [3, 12] the perovskite with type II heterostructures may show different photophysical behaviors when compared with conventional perovskite structures.

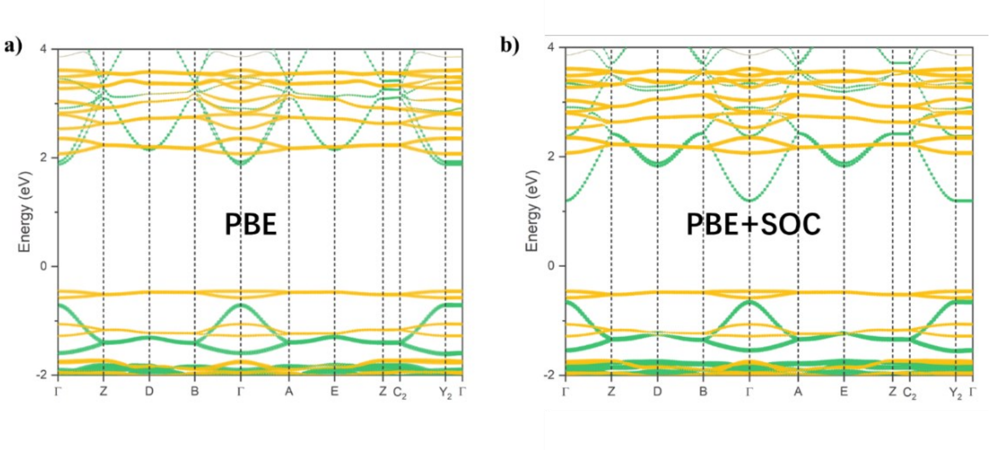

Figure 3.11. Energy band structures of the configuration of 2D M1/PB determined by DFT implementation with a) Perdew–Burke-Ernzerhof (PBE) functional and b) PBE functional taking into account the spin-orbit coupling (SOC) interaction.

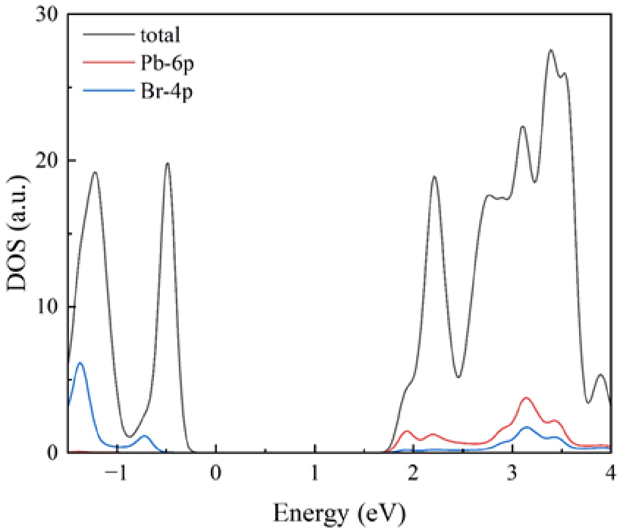

Figure 3.12 Computed projected density of states (PDOS) of M1/PB based on Perdew–Burke-Ernzerhof (PBE) scheme.

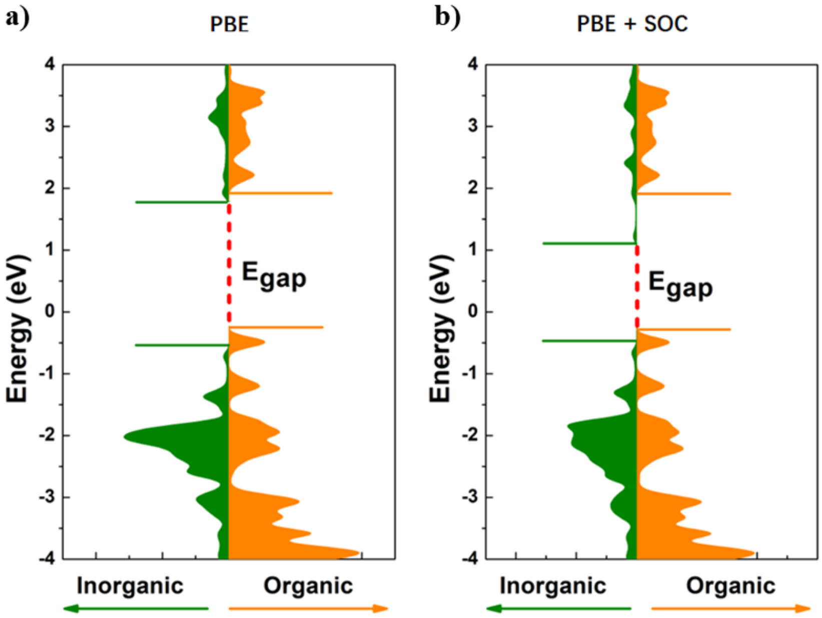

Figure 3.13. Band alignments for 2D M1/PB determined by DFT implementation with a) Perdew–Burke-Ernzerhof (PBE) functional and b) PBE functional taking into account the spin-orbit coupling (SOC) interaction.

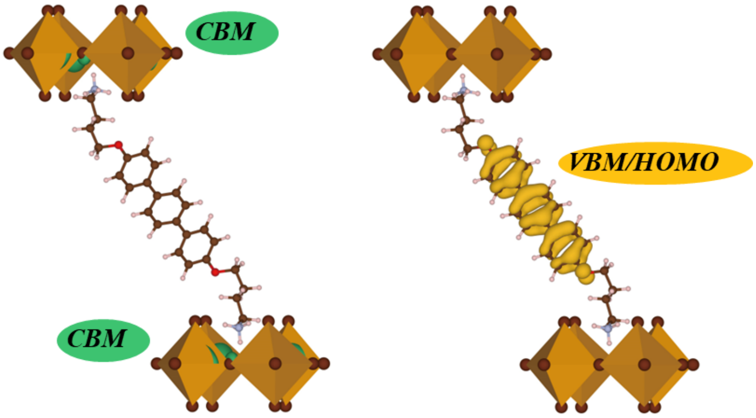

Figure 3.14 Charge density for VBM corresponding to HOMO and CBM in M1/PB.

3.2.3 Photophysical properties

To further investigate the photophysical properties of the hybrid M1/PB system, additional optical characterizations were performed. Here, a butylammonium (BA) based 2D $(BA)_2PbBr_4$ perovskite was prepared and used for comparison. $(BA)_2PbBr_4$ is well known to form a type I heterostructure by combining wide-bandgap BA derivatives and $PbBr_4$ according to the previous report. [13] An illustration of its band alignment is shown in **Figure** 3.15a. As shown in **Figure** 3.15c, a sharp excitonic peak around 400 nm is observed from the $(BA)_2PbBr_4$ film, indicating the stabilization of excitons in the quantum well structure. As already described, a similar excitonic absorption peak is also observed in the absorption spectrum of an M1/PB film. When the $(BA)_2PbBr_4$ and M1/PB thin films were excited with λ_{ex}=280 nm, it resulted in the excitation of both organic and inorganic components and the photoluminescence (PL) spectra of these films are shown in **Figure** 3.15d. We observed a sharp and intense peak for the $(BA)_2PbBr_4$ film, which is associated with the excitonic emission from the $PbBr_4$ inorganic layers. Compared to $(BA)_2PbBr_4$, on the other hand, M1/PB perovskite, which presents a type II heterostructure (**Figure** 3.15b), shows a distinct PL behavior. A broader and weaker emission is detected from the M1/PB thin film which can be ascribed to the M1 organic component.

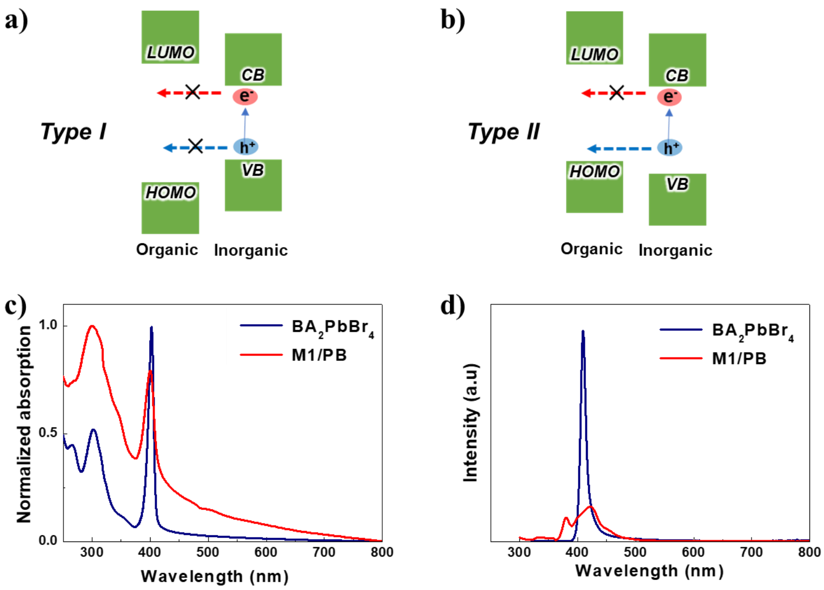

Figure 3.15. The illustration of the band alignment for (a) $(BA)_2PbBr_4$ and (b) M1/PB. (c) Absorption and (d) PL spectra of the $(BA)_2PbBr_4$ and M1/PB thin films.

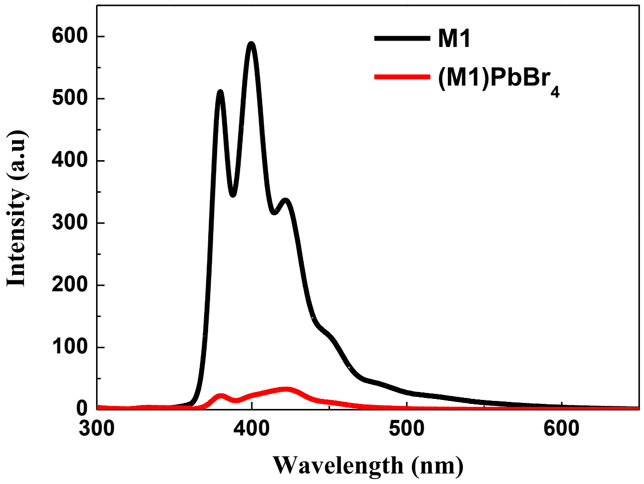

Figure 3.16 PL spectra of the M1 diamine organic salt and 2D M1/PB neat films.

The PL quantum efficiency (PLQY) of the neat film of a pure M1 organic ligand was measured to be 90%. However, it was significantly reduced to 2% in the M1/PB perovskite film associated with a significant quenching of the PL intensity as shown in **Figure** 3.16. The PL average lifetime estimated from the time-resolved transient PL decay curves (**Figure** 3.17) is determined to be 1.5 ns for the M1/PB perovskite film, which is shorter than 3.2 ns of the pure M1 ligands. The shorter PL average lifetime with the quenched PL intensity in an M1/PB perovskite film compared to those of M1 ligands suggests exciton dissociation at the interface between the organic M1 and $PbBr_4$ inorganic layers due to the formation of a type II structure. However, other quenching mechanisms cannot be ruled out at this stage and further investigations should be carried out to clarify in detail this issue.

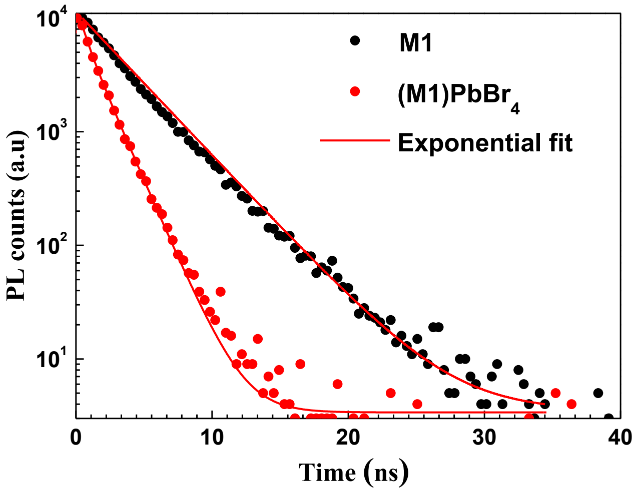

Figure 3.17 Time-resolved PL decay curves for M1 and M1/PB neat films.

3.2.4 Electrical properties

The type II heterostructures of M1/PB should promote the spatial charge separation of electrons and holes at the heterointerface and subsequently transport electrons and holes through distinct conductive channels. Thus, such a system with efficient charge separation and transport has great potential for optoelectronic device applications. In the case of M1/PB with type IIb heterostructure, electrons can be directly transported through the $PbBr_4$ inorganic layers, while holes can be transported through organic M1 layers as shown in **Figure** 3.18. To know the ability of charge injection and transport in the M1/PB structure, gap-type single carrier devices such as an electron-only device (EOD) and a hole-only device (HOD) were fabricated. We prepared EOD and HOD with the structures of Au/C60/M1/PB/C60/Au and Au/MoOx/M1/PB/MoOx/Au, respectively, as shown in **Figures** 3.19a and 3.19b. Note that the planar electrode architecture of the devices is well adapted by considering the preferential orientation of the hybrid M1/PB layered structure in the plane of the thin films as evidenced by the GIWAXS experiments. The corresponding energy level of both device types is shown in **Figure** 3.20.

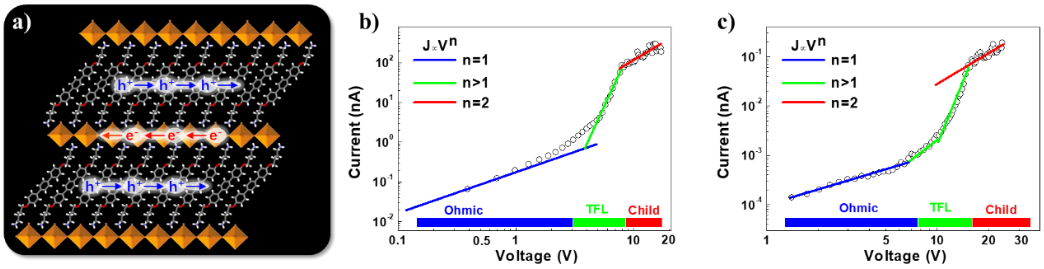

Figure 3.18 (a) Illustration of the charge transport in M1/PB thin films and single crystals. Current-Voltage (J-V) characteristics of (b) EOD and (c) HOD prepared with M1/PB single crystals.

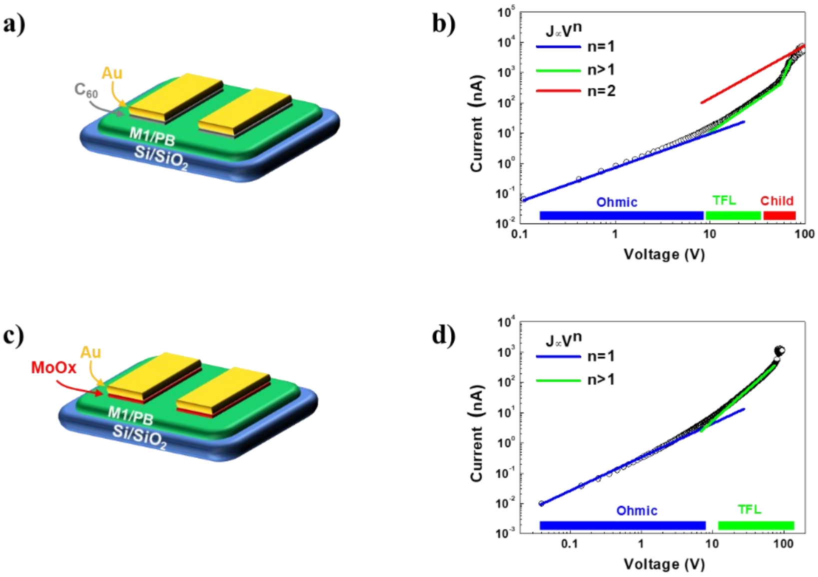

Figure 3.19 Current-voltage (J-V) characteristics of (a) EOD and (b) HOD prepared with M1/PB thin films.

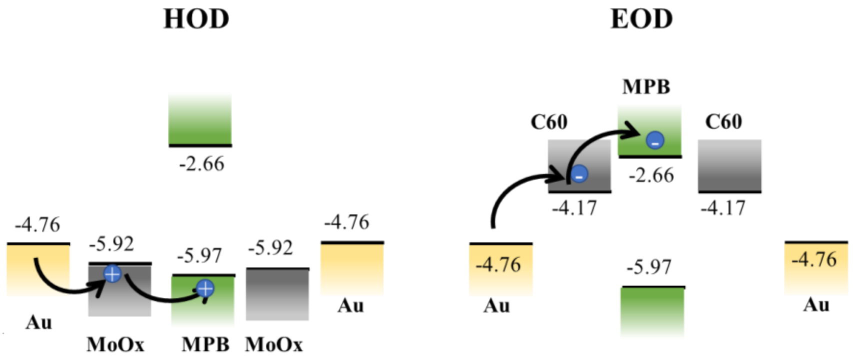

Figure 3.20 Energy diagram of HOD (left) and EOD (right).

First, in the case of M1/PB-based EOD, three distinct regions were observed from the I-V curve as shown in **Figure** 3.18. At low applied voltage, it is probable that thermally generated free carriers inside the M1/PB film contribute to the current, leading to a linear relationship ($J \propto V^n$, n=1, blue color) of I-V following Ohm's law. With an increase in the applied voltage, the carrier injection from the electrode contributes to filling the traps and reach to the trap-filled limit (TFL) ($J \propto V^n$, n>1, green color). With further increase of the applied voltage, all traps are filled and the conduction becomes space-charge-limited (child's law), which shows a linear relationship with the square of the voltage ($J \propto V^n$, n=2, red color). The current from the space charge limited current (SCLC) region is mainly driven by the injected charge carriers from the electrode. From these I-V characteristics, the carrier mobility can be estimated by Geurst's SCLC model for a Gap-type structure: [14-16]

$$I = (2W\varepsilon\varepsilon_{\circ}\mu V^{2})/(\pi L^{2)})$$

where μ is the carrier mobility, W and L are the device width and length, ε is the vacuum permittivity, and ε_o is the relative dielectric constant of the conducting layers. For the M1/PB film, the electron mobility was calculated to be 1.9 ±1 x 10^{-4} cm^2 V^{-1} s^{-1}. However, with the maximum voltage of 100 V, the I-V curve obtained from HOD shows only two regions including the ohmic and TFL regions as shown in **Figure** 3.19. The I-V curve could not reach the SCLC region probably due to the high resistance and low mobility of the M1/PB film. From the AFM image in **Figure** 3.21, the thin film shows a rather rough surface with a polycrystalline structure composed of many grain boundaries. The rough surface and grain boundaries would restrict the charge injection and transport, [17] causing low mobility of the film. Usually, single crystals with a flat surface and without grain boundaries are more efficient for electrical contact.

Thus, the single crystals obtained with M1/PB were used for the fabrication of EODs and HODs. The I-V curves obtained from M1/PB single crystal show similar behaviors to the M1/PB film as presented in **Figures** 3.18b and 3.19a. Importantly, the I-V curves from both EOD and HOD show the SCLC region, indicating the higher mobility of the single crystal than the film. Based on the SCLC region, the electron and hole mobilities are calculated to be 0.3 ±0.2 cm^2 V^{-1} s^{-1} and 7.0 ±3 x 10^{-4} cm^2 V^{-1} s^{-1}, respectively.

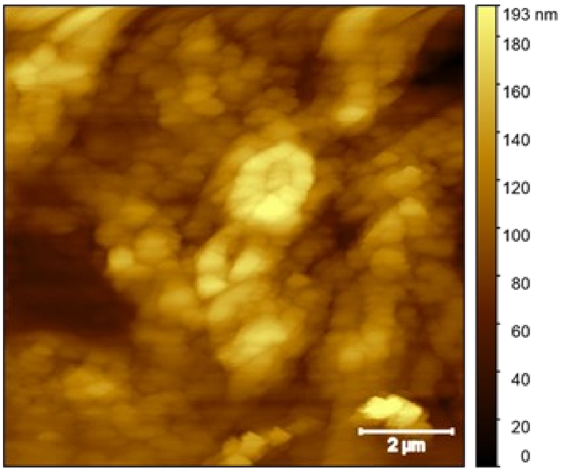

Figure 3.21. Topography AFM image of 2D M1/PB perovskite film.

We noted that the I-V curves show slight fluctuation at high voltage, and this phenomenon also exists in other reports. [18, 19] The fluctuation of the current is probably associated with the degradation of the perovskite at high voltage. In the case of M1/PB with type II heterostructure, the electrons should be transferred through the inorganic $PbBr_4$ layers. The lower electron mobility obtained from the M1/PB single crystal than the conventional 3D perovskite might be caused by the large electron injection barrier between C_{60} and M1/PB single crystal (**Figure** 3.20). In the future, by using a suitable electron injection layer, a lower injection barrier may further improve the electron mobility. The hole mobility originating from the organic layers of M1/PB single crystal shows almost three orders of magnitude lower than electron mobility. In order to know the reason for the lower hole mobility than the electron, the effective masses of the electrons and holes were calculated. The calculated hole effective mass along the Γ-B direction (50.85) is significantly larger than the electron (0.27). Based on the charge transport mechanism, the charge mobility is inversely proportional to the effective mass.[20] Therefore, the higher hole effective mass is consistent with the lower hole mobility of the organic part. To better understand the reason for the low mobility in the organic sublayers, the charge transport properties of a single crystal of an M1 homologue derivative without diammonium groups, named M1', were also investigated by SCLC (**Figure** 3.22). M1' shows a hole mobility as high as 2.4 ±1 $cm^2\ V^{-1}\ s^{-1}$ which is four orders of magnitude higher than that measured in M1/PB. The packing of M1 ligands confined in the perovskite structure is strongly constrained by its double grafting to the perovskite sublayers and by the large discrepancy of the width (cross-sectional area) of the organic cation with the area provided by the inorganic substructure, as evidenced by the large tilt of the terphenyl dications in the organic layers (**Figure** 3.7). The smaller hole mobility obtained from the organic part in M1/PB could be explained by this peculiar tilted arrangement that limits the transfer integral overlap of the π-conjugated systems. This assumption is consistent with the high mobility observed in the single crystal of M1' which shows a much lower titled angle of the terphenyl units than in M1/PB (**Figure** 3.23). As a result, the introduction of organic ligands with a larger cross-sectional area of their aromatic system could be considered in the future to enhance their π-interactions and improve the mobility of the organic part in 2D hybrid perovskite structures.

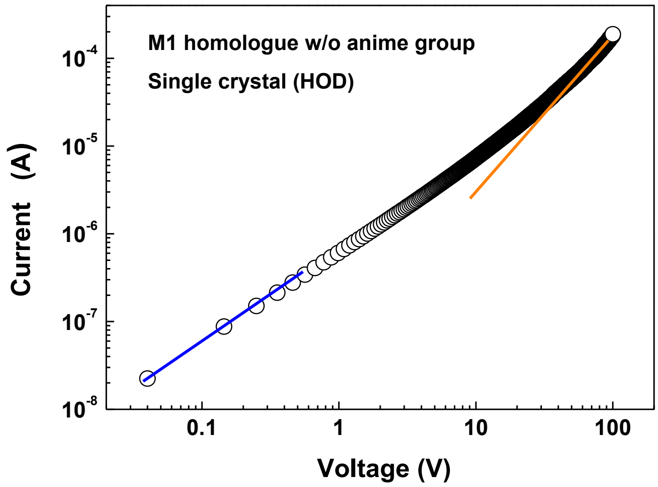

Figure 3.22. I-V curve of a HOD based on a single-crystal of M1'.

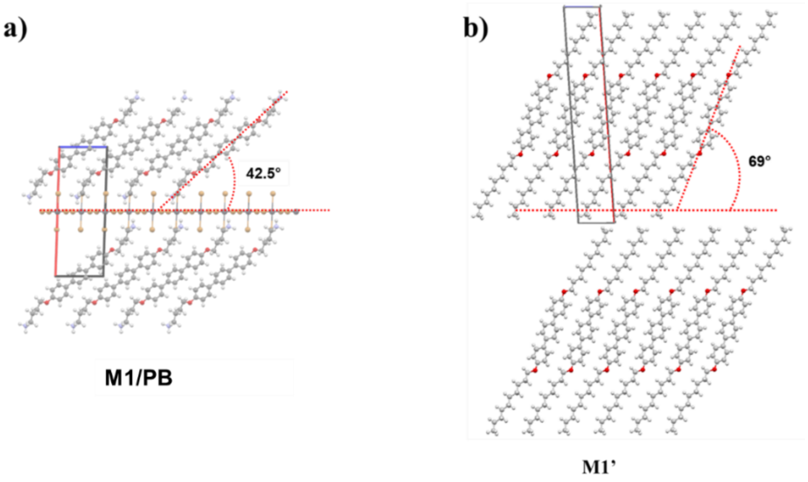

Figure 3.23. Crystal structures of a) M1/PB and b) M1' and illustrations of the tilt angle of the terphenyl cores in the layered structure.

3.3 Summary

In conclusion, we have prepared a rare example of an organic-inorganic hybrid 2D perovskite structure composed of inorganic monolayers of metal-halide octahedra separated by monolayers of terphenyl-based diammonium organic cations. We investigated its thin film and single-crystal structure and confirmed the excellent stability of this 2D hybrid perovskite. The investigations of its electronic and photophysical properties by experimental measurements and DFT simulations evidenced the unusual type IIb band alignment between the organic donor and inorganic acceptor components. As a result, this type II 2D perovskite heterostructure presents two intercalated separate pathways for electrons and holes which can migrate within the inorganic and organic sublayers, respectively. The investigations of the charge transport properties of such a type II heterostructure were performed for the first time by the SCLC method with hole-only and electron-only devices (HODs/EODs) based on both thin films and single crystals and maximum electron and hole mobilities of about 0.3 and 7.0 x 10^{-4} cm^2 V^{-1} s^{-1}, respectively, were obtained. We believe that this work gives an important insight into designing an organic-inorganic hybrid system which is of paramount importance for future light emission applications.

3.4 Experimental section

3.4.1 Materials synthesis

All commercially available chemicals and reagents were used without further purification. All reactions were monitored by analytical thin layer chromatography (TLC) purchased from Merck & Co., Inc. Purification was carried out using a silica gel (200-300 nm) column. The organic semiconductor ligand investigated in this paper were synthesized by following the procedures described below.

Scheme-1: Synthesis of intermediate 3

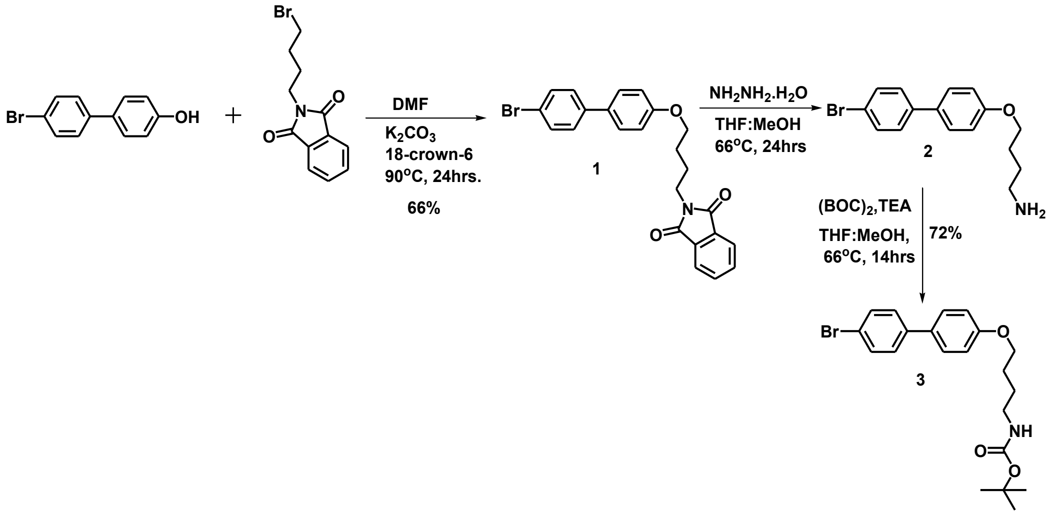

2-(4-((4'-bromo-[1,1'-biphenyl]-4-yl)oxy)butyl)isoindoline-1,3-dione (1)

A 100 mL two-neck flask was charged with 4'-bromo-[1,1'-biphenyl]-4-ol (5.0 g, 20.07mmol), 2-(4-bromobutyl) isoindoline-1,3-dione (5.6 g, 20.07 mmol), K_2CO_3 (8.32 g, 60.21mmol) and 18-crown-6 (0.53 g, 2.07 mmol) in 60 mL of dry DMF were stirred under argon at 90 °C for 24 h. The reaction was cooled to room temperature and removed solvent by a rotary evaporator. The crude mixture was extracted with dichloromethane (200mL) and washed with water (3×200mL), then dried over MgSO4. After the removal of the solvent under reduced pressure, the crude product was sonicated in methanol for 3 minutes, and the resulted white solid was collected by filtration, yielding a white solid (5.95 g, 66%). ^{1}H NMR (400 MHz, Chloroform-d) δ 7.85 (dd, J = 5.5, 3.1 Hz, 2H), 7.71 (dd, J = 5.4, 3.1 Hz, 2H), 7.52 (d, J = 8.2 Hz, 2H), 7.45 (d, J = 8.4 Hz, 2H), 7.39 (d, J = 8.2 Hz, 2H), 6.94 (d, J = 8.4 Hz, 2H), 4.03 (t, J = 5.8 Hz, 2H), 3.78 (t, J = 6.6 Hz, 2H), 1.89 (m, 4H). ^{13}C NMR (101 MHz, CDCl3) δ 168.44, 158.75, 139.76, 133.93, 132.42, 132.12, 131.76, 128.27, 127.93, 123.22, 120.73, 114.99, 114.92, 67.27, 37.65, 26.63, 25.33.

4-((4'-bromo-[1,1'-biphenyl]-4-yl)oxy)butan-1-amine (2)

Compound 1 (5.0 g, 11.10 mmol) was dissolved in 60 mL of THF in a 250 ml flask at 65 °C under argon. Then 40 mL of methanol was added at the same temperature and stirred for 20 minutes. Hydrazine monohydrate (64%) (4.2 mL, 55.5 mmol) was injected into the reaction mixture, and stirred for 24 hrs. under argon at the same temperature. After cooled to room temperature, solvents were removed under reduced pressure. After drying, the crude product was used in the next step without further purification. HRMS calcd for $C_{16}H_{18}BrNO$ $[M+H]^+$ 320.0644; found 320.0646.

Tert-butyl (4-((4'-bromo-[1,1'-biphenyl]-4-yl)oxy)butyl)carbamate (3)

The intermediate 2 (4.66 g, 14.56 mmol) and di-tert-butyl decarbonate (7.94 g, 36.4 mmol) were dissolved in a mixture of THF (60 mL) and methanol (40 mL) at 66 °C under argon. Triethyl amine (3.85 mL, 27.6 mmol) was added dropwise to the reaction mixture, then stirred for 24 hrs. After completion of the reaction, solvents were removed under reduced pressure, then extracted with water and dichloromethane. The organic layer was dried over anhydrous $MgSO_4$, filtered through celite and then the solvent was removed under reduced pressure. The crude material was purified by silica gel column chromatography eluting with dichloromethane and ethyl acetate to give compound 3 as a white solid (3.36 g, 72 %). ^{1}H NMR (400 MHz, Chloroform-*d*) δ 7.52 (d, *J* = 8.5 Hz, 2H), 7.47 (d, *J* = 8.7 Hz, 2H), 7.40 (d, *J* = 8.5 Hz, 2H), 6.95 (d, *J* = 8.6 Hz, 2H), 4.61 (s, 1H), 4.02 (t, *J* = 6.2 Hz, 2H), 3.21 (m, 2H), 1.84 (m, 2H), 1.73 – 1.64 (m, 2H), 1.45 (s, 9H). ^{13}C NMR (101 MHz, $CDCl_3$) δ 158.76, 156.03, 139.75, 132.46, 131.77, 128.28, 127.96, 120.76, 114.89, 67.60, 28.44, 26.87, 26.57. HRMS calcd for $C_{21}H_{26}BrNO_3$ $[M+Na]^+$ 442.0988; found 442.0989.

2-(4-(4-bromophenoxy)butyl)isoindoline-1,3-dione (4)

A 500 mL two-neck flask was charged with 2-(4-bromobutyl) isoindoline-1,3-dione (1) (37 g, 131.14 mmol), 4-bromophenol (24.95 g, 144 mmol), K_2CO_3 (45.3 g, 327.8 mmol) and 18-crown-6 (3.46 g, 13.1 mmol), in 150 mL of acetone and refluxed the reaction under argon at 70°C for 24hrs. The reaction was cooled to room temperature and removed solvent by a rotary evaporator. The crude mixture was extracted with dichloromethane (200mL) and washed with water (3×200mL), then dried over $MgSO_4$, and filtered. The crude product was purified by column chromatography over silica gel with cyclohexane and dichloromethane as the eluent, giving a highly viscous liquid. It was then sonicated with pentane for 5 minutes, yielding a white solid (38.5 g, 78 %). ^{1}H NMR (400 MHz, Chloroform-*d*) δ 7.87 (dd, *J* = 5.4, 3.0 Hz, 2H), 7.74 (dd, *J* = 5.4, 3.0 Hz, 2H), 7.36 (d, *J* = 9.0 Hz, 2H), 6.78 (d, *J* = 9.0 Hz, 2H), 3.98 (t, *J* = 5.9 Hz, 2H), 3.79 (t, *J* = 6.7 Hz, 2H), 2.00 – 1.75 (m, 4H). ^{13}C NMR (101 MHz, $CDCl_3$) δ 168.41, 158.00, 133.93, 132.19, 132.09, 123.21, 116.30, 112.76, 67.39, 37.59, 26.51, 25.25. HRMS calcd. for $C_{18}H_{16}BrNO_3$ $[M+NH_4]^+$ 391.0657; found 391.0652

Scheme-2: Synthesis of intermediate 7

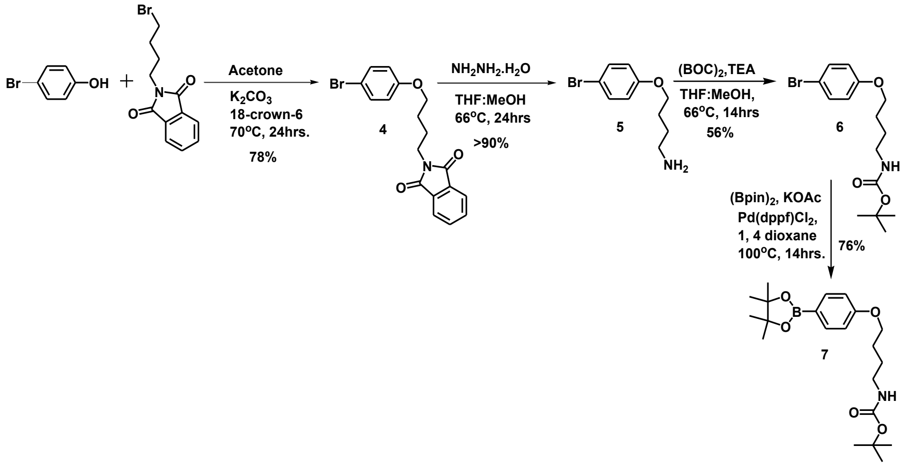

4-(4-bromophenoxy)butan-1-amine (5)

Compound 4 (10.0 g, 26.73 mmol) was dissolved in 60 mL of THF in a 250 ml flask at 65 °C under argon. Then 40 mL of methanol was added at the same temperature and stirred for 20 minutes. Hydrazine monohydrate (64%) (10.13 mL, 133.68 mmol) was injected into the reaction mixture, and stirred for 24 hrs. under argon. The reaction was stirred until no starting material, was monitored by TLC. After completion of the reaction, the solvents were removed under reduced pressure. After drying, the crude product was used in the next step without further purification.

Tert-butyl (4-(4-bromophenoxy)butyl)carbamate (6)

In a 250 mL three-neck flask, intermediate 5 (5.52 g, 26.7 mmol) and di-tert-butyl decarbonate (14.57 g, 66.76 mmol) were dissolved in a mixture of THF (60 mL) and methanol (40 mL) under argon. Triethyl amine (9.3 mL, 66.76 mmol) was added dropwise to the reaction mixture, then stirred for 24 hrs at 66 °C. After the completion of the reaction, solvents were removed under reduced pressure, then extracted with water and dichloromethane. The organic layer was dried over anhydrous $MgSO_4$, filtered through celite and then the solvent was removed under reduced pressure. The crude material was purified by silica gel column chromatography eluting with dichloromethane and ethyl acetate to give intermediate 6 as a white solid (5.1 g, 56 %).

^{1}H NMR (400 MHz, Chloroform-d) δ 7.35 (d, J = 8.8 Hz, 1H), 6.76 (d, J = 8.9 Hz, 1H), 4.58 (s, 1H), 3.93 (t, J = 6.2 Hz, 1H), 3.18 (s, 1H), 1.80 (dd, J = 8.7, 6.1 Hz, 1H), 1.69 – 1.56 (m, 2H). ^{13}C NMR (101 MHz, CDCl3) δ 158.02, 156.01, 132.22, 116.28, 112.76, 67.72, 28.42, 26.82, 26.47. HRMS calcd for $C_{18}H_{16}BrNO_3$ $[M+Na]^+$ 366.0657; found 366.0675.

Tert-butyl (4-(4-(4,4,5,5-tetramethyl-1,3,2-dioxaborolan-2-yl)phenoxy)butyl) carbamate (7)

In a 250 mL three-neck flask, intermediate 6 (4.96 g, 14.4 mmol), bispinacalato diboron (5.48 g, 21.6 mmol), and KOAc (4.23 g, 43.2 mmol) in 100 mL of 1,4 dioxane was degassed with argon gas for 20 minutes, then Pd(dppf)Cl_2 (0.21 g, 0.28 mmol) was added. The reaction mixture was stirred under argon at 100°C for 24 h. After cooling to room temperature, the crude product was passed through a plug of Celite® and washed with dichloromethane. The solvent was removed under reduced pressure, then extracted with dichloromethane and water. The solvents were evaporated from the crude product under reduced pressure. The residue was purified by column chromatography on silica gel with dichloromethane/methanol, yielding 7 as a colorless oily solid (4.3g, 76%). ^{1}H NMR (400 MHz, Chloroform-d) δ 7.73 (d, J = 8.2 Hz, 2H), 6.87 (d, J = 8.3 Hz, 2H), 4.59 (s, 1H), 4.00 (t, J = 6.2 Hz, 2H), 3.19 (t, 2H), 1.88 – 1.77 (m, 2H), 1.67 (m, 2H), 1.44 (s, 9H), 1.33 (s, 12H). ^{13}C NMR (101 MHz, CDCl3) δ 161.49, 156.06, 136.69, 136.50, 114.88, 113.83, 83.54, 77.23, 67.26, 28.43, 26.82, 26.52, 24.85. HRMS calcd for $C_{21}H_{34}BNO_5$ $[M+H]^+$ 392.2603; found 392.2605.

Scheme-3: Synthesis of M1

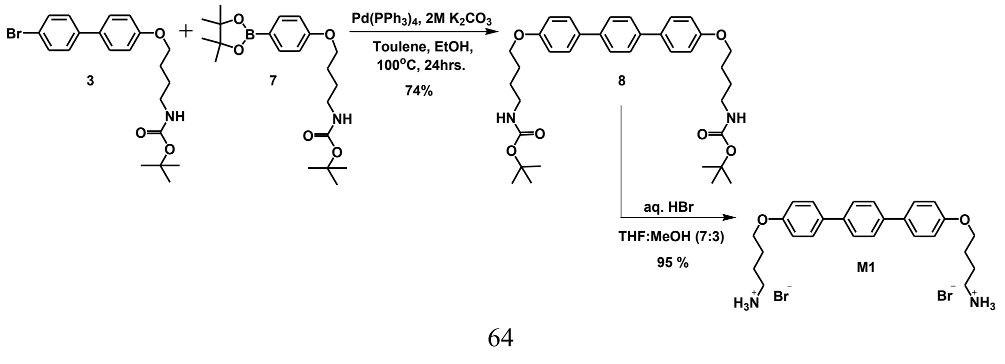

Di-tert-butyl (([1,1':4',1''-terphenyl]-4,4''-diylbis(oxy))bis(butane-4,1-diyl)) dicarbamate (8)

In a 250 mL three-neck flask, intermediate 3 (4.96 g, 14.4 mmol) and 7 (4.96 g, 14.4 mmol), were dissolved in a mixture of 100 mL of toluene and 20 mL of EtOH. Then Na_2CO_3 (3.02 g, 28.5 mmol) was dissolved in 5 mL of deionized water, and was added into the reaction flask. The solution was degassed with argon gas for 20 minutes, then Pd $(PPh_3)_4$ (0.21 g, 0.28 mmol) was added and stirred under argon at 100 °C for 24 h. The solvent was removed under reduced pressure, then extracted with dichloromethane and water, and dried over $MgSO_4$. The solution was passed through a plug of Celite® and washed with dichloromethane. The solvent was evaporated and the residue was purified by column chromatography on silica gel with dichloromethane/methanol, yielding a white solid. It was further purified by washing with MeOH (2.13g, 74.2%). ^{1}H NMR (400 MHz, Chloroform-d) δ 7.60 (s, 4H), 7.55 (d, J = 8.5 Hz, 4H), 6.97 (d, J = 8.6 Hz, 4H), 4.61 (s, 2H), 4.03 (t, J = 6.2 Hz, 4H), 3.21 (t, 4H), 1.85 (m, 4H), 1.75 – 1.65 (m, 4H), 1.45 (s, 18H). ^{13}C NMR (101 MHz, CDCl3) δ 158.49, 156.03, 139.11, 133.30, 127.97, 126.98, 114.81, 77.22, 67.58, 40.13, 28.44, 26.89, 26.61. HRMS calcd for $C_{36}H_{48}N_2O_6$ $[M+Na]^+$ 627.3405; found 627.3413.

4,4'-([1,1':4',1''-terphenyl]-4,4''-diylbis(oxy))bis(butan-1-aminium)dibromide (M1)

In a 250 mL two-neck flask fitted with a condenser, compound 8 (2.02 g 3.34 mmol) was dissolved in 60 mL THF at 45 ºC, then methanol (30 mL) was added under argon. The solution of aq. HBr (48%) (7.55 mL, 66.8 mmol) was injected into the reaction mixture, and stirred for 24 hrs. under argon. After cooled to room temperature, solvents were removed under reduced pressure, then precipitated in a mixture of methanol (10%) and dichloromethane (90%). The resulting product was further purified by washing with a mixture of methanol (10%) and dichloromethane (90%) (100 mL ×2), diethyl ether (100 mL) and finally pentane to yield a bright white solid (1.78 g, 94.6%). ^{1}H NMR (400 MHz, DMSO-d6) δ 7.72 (s, 6H), 7.69 (s, 4H), 7.66 (d, J = 8.6 Hz, 4H), 7.05 (d, J = 8.6 Hz, 4H), 4.06 (t, J = 6.0 Hz, 4H), 2.89 (t, J = 7.4 Hz, 4H), 1.77 (m, 8H). ^{13}C

NMR (101 MHz, DMSO) δ 158.62, 138.52, 132.50, 128.03, 127.02, 115.43, 67.45, 39.09, 26.17, 24.39. HRMS calcd for $C_{26}H_{32}N_2O_2$ (-2HBr) $[M+H]^+$ 405.2537; found 405.2537.

Scheme-4: Synthesis of M1’

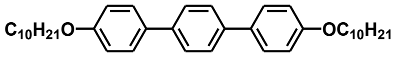

M1'

4,4''-bis(decyloxy)-1,1':4',1''-terphenyl (M1’)

This compound was prepared according to the reference [21].

^{1}H NMR (400 MHz, Chloroform-*d*) δ 7.60 (s, 4H), 7.55 (d, J = 8.4 Hz, 4H), 6.98 (d, J = 8.4 Hz, 4H), 4.01 (t, J = 6.6 Hz, 4H), 1.81 (t, J = 7.3 Hz, 4H), 1.27 (d, J = 12.4 Hz, 34H), 0.89 (t, J = 6.4 Hz, 6H).

2D M1/PB perovskite thin film fabrication: M1/PB perovskite precursor solutions (0.1 M) were prepared by dissolving the M1 salts and lead bromide ($PbBr_2$) (99,999%, Aldrich) with a 1:1 molar ratio in anhydrous DMSO. The solutions were stirred for 3 hours until the complete dissolution of the precursors. Anhydrous DMSO (99.8%, Sigma–Aldrich) was purchased in a septum-sealed bottle and stored in a nitrogen-filled box prior to use. All the depositions were performed in the glove box. Quartz substrates were cleaned ultrasonically and sequentially with acetone, isopropanol and deionized water, then dried in an oven, and finally exposed to ultraviolet light and ozone for about 10 min. The perovskite materials were then deposited by spin-coating the precursor solutions at 3000 rpm for 60 seconds. The perovskite layers were formed after annealing at 70 °C for 10 minutes and 100 °C for 5 minutes. The thickness of the perovskite film measured using a surface profilometer (DektakXT, Bruker) was ~ 30 nm. For comparison, a $(BA)_2PbBr_4$ film was prepared using the same conditions mentioned earlier, resulting in a similar film thickness (~30 nm). M1 salt reference layers were obtained by dissolving M1 salt in anhydrous DMSO. The M1 solution was then deposited on quartz by spin-coating at 2000 rpm for 60 seconds, followed by annealing at 70 °C for 10 minutes and 100 °C for 5 minutes. The thickness of the M1 film measured using a surface profilometer (DektakXT, Bruker) was ~ 30 nm.

3.4.2 Hybrid M1/PB and M1' single crystal preparation

Single crystals were grown using an anti-solvent crystallization method based on the previous report [22]. 0.01 M solution of M1/PB was prepared by dissolving M1 and $PbBr_2$ with 1: 1 molar ratio in anhydrous DMSO. The solution was stirred for 3 hours until the complete dissolution of the precursors. The vial containing the solution was then placed in a bigger vessel filled with Dichloromethane (DCM). After 1 week of anti-solvent diffusion, transparent crystals were collected by washing with DCM 5 times. Single crystals of M1' were grown by slow evaporation of a quasi-saturated dichloromethane solution of M1' for several days at room temperature under ambient atmosphere.

3.4.3 Characterization

NMR spectra: ^1H and ^{13}C NMR spectra were measured with a Bruker Avance 400 MHz spectrometer in $CDCl_3$ or DMSO-d_6. Chemical shifts were reported in δ ppm and referenced to the solvent residual peak at δ 7.26 ppm for ^1H and 77.0 ppm for ^{13}C NMR spectra in $CDCl_3$; at δ 2.50 ppm for ^1H and 39.6 ppm for ^{13}C NMR spectra in DMSO-d_6, respectively.

Mass spectra: High-resolution mass spectrometry (HRMS) by fast atom bombardment was performed using a JEOL JMS-700 spectrometer.

UV-vis absorption spectra and steady-state PL spectra: UV-vis absorption spectra for all the samples were measured on Lambda 950 KPA spectrophotometer (PerkinElmer, USA). Steady-state PL spectra were recorded using an FP-8600 PL spectrometer (JASCO, Japan).

PL quantum yield and time-resolved spectroscopy measurements: Absolute PL quantum yields (PLQYs) were measured on a Quantaurus-QY measurement system (C11347-11, Hamamatsu Photonics) under nitrogen flow and all samples were excited at 280 nm. The transient PL decay characteristics of solution and film samples were recorded at room temperature using a Quantaurus-Tau fluorescence lifetime measurement system (C11367-03, Hamamatsu Photonics). All the samples were excited at 280 nm and the detection wavelength was 400 nm, 420 nm, and 410 nm for M1, M1/PB, and $(BA)_2PbBr_4$, respectively.

PES and LEIPS: The energy levels of all the films used in this study were measured by photoelectron yield spectroscopy (AC-3, Riken Keiki) or low-energy inverse photoemission spectroscopy (LE-1, ALS Technology) and the samples used for the energy-level measurements consisted of 10-nm-thick films spin-coated on ITO-coated glass substrates.

Atomic force microscopy (AFM): The morphology of 2D perovskite thin films, which were spin-coated on SiO_2/Si substrates in a nitrogen-filled glove box with oxygen and moisture levels less than 1 ppm, were measured using an atomic force microscope (JSPM-5400, JEOL) in amplitude-modulation mode.

Out-of-plane and in-plane X-ray diffraction (XRD): Out-of-plane and in-plane XRD patterns of 2D perovskite thin films were measured with a Rigaku Smart Lab using a Cu Kα source (λ = 1.542 Å). All the manipulations of XRD measurement were performed under ambient conditions.

Grazing Incidence Wide-Angle X-ray Scattering (GIWAXS): GIWAXS measurements were carried out at the PLS-II 9A U-SAXS beamline of Pohang Accelerator Laboratory (PAL) in Korea. Samples consisted of layers on a silicon wafer of twenty to forty nanometers in thickness. The X-rays from the vacuum undulator (IVU) were monochromated using Si(111) double crystals and focused on the detector using K-B-type mirrors. Patterns were recorded with a Rayonix 2D SX 165 CCD detector. The sample-to-detector distance was about 221 mm for energy of 11.08 keV (1.119 Å).

Single-crystal XRD: A very thin single crystal of compound M1/PB and M1' was selected, mounted onto a cryoloop, and transferred in the cold nitrogen gas stream of an Oxford Cryostream. Intensity data were collected with a BRUKER Kappa-APEXII diffractometer with micro-focused Cu-Kα radiation (λ=1.54178 Å) at 200K. APEX 3 suite and SAINT program (BRUKER) were used to carry out data collection, unit-cell parameters refinement, integration and data reduction. SADABS (BRUKER) was used for scaling and multi-scan absorption corrections. In the Olex2 suite [23], the structure was solved with SHELXS [24] program and refined by full-matrix least-squares methods using SHELXL-14 [25]. All non-hydrogen atoms were refined anisotropically. Hydrogen atoms were visible on the Fourier difference map, and they were placed at calculated positions and refined with a riding model.

Electron- and hole-only devices (EOD and HOD) fabrication and measurements: Device fabrication was performed inside a nitrogen-filled glove box with oxygen and water level less than 1 ppm. The Si wafers coated with a 300 nm SiO_2 dielectric layer were used as substrates for film preparation. The substrates were cleaned sequentially by ultrasonication in detergent solution, pure water, acetone, and isopropanol for 10 min each, and dried using a nitrogen gun. Then, the substrates were treated with UV-ozone for 30 min, and transferred into a glove box for further use. The perovskite materials were then deposited on the Si wafer by spin-coating the precursor solutions at 3000 rpm for 60 seconds. The perovskite layers were then formed after annealing at 70 °C for 10 minutes and 100 °C for 5 minutes. The EOD and HOD were fabricated by vacuum deposition process without exposure to ambient air. MoO_X (20 nm) and Au (100 nm) were deposited above the 2D MPB film or single crystal at 0.2 and 1 Å/s, respectively. The thickness of the single crystal measured using a surface profilometer (DektakXT, Bruker) was ~ 400 nm. The shadow mask with a 30 μm gap and 2 mm width was used for EOD and HOD fabrication. Regarding devices based on single crystals, the effective width was measured by using an optical microscope. The *I-V* measurements were measured with forward and reverse scans using a semiconductor parameter analyzer (B1500A or 4156C, Agilent Technologies). For the calculation of the carrier mobility by Geurst's SCLC model, two values of the relative dielectric constant ε_o were considered ($\varepsilon_o = 25$ for the electron mobility in the inorganic perovskite layers [26] and $\varepsilon_o = 3$ for the hole mobility in the organic layers [27])

3.4.4 Computation method

We used the density functional theory in Vienna Ab-initio Simulation Package (VASP) [28-32] to calculate band structures and densities of states (DOS) for M1/PB. Starting from the single crystal structure, the computational structure was obtained by relaxing them to the nearest local minimum of the structure on the Born-Oppenheimer surface. The Generalized gradient approximation (GGA), as implemented by Perdew-Burke-Ernzerhof (PBE) was selected for the exchange correlation functional. The electron-ion interaction was described using the projection-enhanced plane wave (PAW) pseudopotential. The valence electron configurations involved in the calculations were chosen as $1s^1$ of H, $2s^2p^2$ of C, $2s^2p^3$ of N, $2s^2p^4$ of O, $4s^24p^5$ of Br and $5d^{10}6s^26p^2$ of Pb. The cutoff energy for the plane wave basis was set as 500 eV. The cell volume, shape, and atomic positions were allowed to relax until the forces on any atom became less than 0.01 eV/Å. The convergence criterion of the self-consistent calculations for ionic relaxations was 10^{-5} eV between two consecutive steps. The first Brillouin zone was sampled using a gamma-centered method to generate *k*-point meshes. In the structural optimization, the Γ-centered k-point sampling for M1/PB was 1×3×3. Dense *k*-point grids of 1×6×6 were used for the band structure and DOS calculations. The spin-orbit coupling (SOC) effect was included to account for the relativistic effect of heavy elements. [33] The influence of intermolecular forces was considered by using the zero damping DFT-D3 method of Grimme to perform a van der Waals correction.[30] The effective masses were computed considering the parabolic approximation of the bands near the band extrema. Some data-post processing methods were used with the help of VASPKIT and VESTA packages.[34, 35]

3.5 References

1. Matsushima, T. et al. High performance from extraordinarily thick organic light-emitting diodes. *Nature* **572**, 502-506 (2019).
2. Matsushima, T. et al. Enhanced Electroluminescence from Organic Light-Emitting Diodes with an Organic–Inorganic Perovskite Host Layer. *Adv. Mater.* **30**, 1802662 (2018).
3. Mitzi, D.B., Chondroudis, K. & Kagan, C.R. Organic-inorganic electronics. *IBM J. Res. Dev.* **45**, 29-45 (2001).
4. Mitzi, D.B., Chondroudis, K. & Kagan, C.R. Design, structure, and optical properties of organic− inorganic perovskites containing an oligothiophene chromophore. *Inorg. Chem.* **38**, 6246-6256 (1999).
5. Chondroudis, K. & Mitzi, D.B. Electroluminescence from an organic−inorganic perovskite incorporating a quaterthiophene dye within lead halide perovskite layers. *Chem. Mater.* **11**, 3028-3030 (1999).
6. Safdari, M. et al. Layered 2D alkyldiammonium lead iodide perovskites: synthesis, characterization, and use in solar cells. *J. Mater. Chem.* **4**, 15638-15646 (2016).
7. Xu, Z., Chen, M. & Liu, S.F. First-principles study of enhanced out-of-plane transport properties and stability in Dion–Jacobson two-dimensional perovskite semiconductors for high-performance solar cell applications. *J. Phys. Chem.* **10**, 3670-3675 (2019).
8. Liu, C. et al. Tunable semiconductors: control over carrier states and excitations in layered hybrid organic-inorganic perovskites. *Phys. Rev. Lett.* **121**, 146401 (2018).

9. Saparov, B. & Mitzi, D.B. Organic–inorganic perovskites: structural versatility for functional materials design. *Chem. Rev.* **116**, 4558-4596 (2016).

10. Deng, S. et al. Long-lived charge separation in two-dimensional ligand-perovskite heterostructures. *J. Chem. Phys.* **152**, 044711 (2020).

11. Ju, M.-G. et al. Lead-free low-dimensional tin halide perovskites with functional organic spacers: breaking the charge-transport bottleneck. *J. Mater. Chem. A* **7**, 16742-16747 (2019).

12. Han, D., Chen, S. & Du, M.-H. Role of Polycyclic Aromatic Alkylammonium Cations in Tuning the Electronic Properties and Band Alignment of Two-Dimensional Hybrid Perovskite Semiconductors. *J. Phys. Chem. Lett.* **12**, 9754-9760 (2021).

13. Gao, Y. et al. Molecular engineering of organic–inorganic hybrid perovskites quantum wells. *Nat. Chem.* **11**, 1151-1157 (2019).

14. Geurst, J. Theory of space-charge-limited currents in thin semiconductor layers. *Phys. Status Solidi B Basic Res.* **15**, 107-118 (1966).

15. Lee, L. et al. Wafer-scale single-crystal perovskite patterned thin films based on geometrically-confined lateral crystal growth. *Nat. Commun.* **8**, 15882 (2017).

16. Zubair, M., Ang, Y.S. & Ang, L.K. Thickness dependence of space-charge-limited current in spatially disordered organic semiconductors. *IEEE Trans Electron Devices* **65**, 3421-3429 (2018).

17. Chiu, F.-C. A review on conduction mechanisms in dielectric films. *Adv. Mater. Sci. Eng.* **2014**, 578168 (2014).

18. Lin, Y. et al. Unveiling the operation mechanism of layered perovskite solar cells. *Nat. Commun.* **10**, 1008 (2019).

19. Wang, Y. et al. Metal oxide charge transport layers in perovskite solar cells—optimising low temperature processing and improving the interfaces towards low temperature processed, efficient and stable devices. *J. Phys. Energy* **3**, 012004 (2020).

20. Vehoff, T. et al. Charge transport in self-assembled semiconducting organic

layers: Role of dynamic and static disorder. *J. Phys. Chem. C* **114**, 10592-10597 (2010).

21. Andersch, J. & Tschierske, C. Synthesis and liquid crystalline properties of novel laterally connected twins. *Liq. Cryst.* **21**, 51-63 (1996).

22. Liu, Y., Yang, Z. & Liu, S. Recent progress in single-crystalline perovskite research including crystal preparation, property evaluation, and applications. *Adv. Sci.* **5**, 1700471 (2018).

23. Dolomanov, O.V., Bourhis, L.J., Gildea, R.J., Howard, J.A. & Puschmann, H. OLEX2: a complete structure solution, refinement and analysis program. *J. Appl. Crystallogr.* **42**, 339-341 (2009).

24. Sheldrick, G.M. A short history of SHELX. *Acta Crystallogr.* **64**, 112-122 (2008).

25. Sheldrick, G.M. SHELXT–Integrated space-group and crystal-structure determination. *Acta Crystallogr.* **71**, 3-8 (2015).

26. Ma, K. et al. Organic Cation Engineering for Vertical Charge Transport in Lead-Free Perovskite Quantum Wells. *S Small Sci.* **1**, 2000024 (2021).

27. Li, Y., Clevenger, R.G., Jin, L., Kilway, K.V. & Peng, Z. Unusually high SCLC hole mobility in solution-processed thin films of a polycyclic thiophene-based small-molecule semiconductor. *J. Mater. Chem. C* **2**, 7180-7183 (2014).

28. Perdew, J.P. et al. Restoring the density-gradient expansion for exchange in solids and surfaces. *Phys. Rev. Lett.* **100**, 136406 (2008).

29. Perdew, J.P., Burke, K. & Ernzerhof, M. Generalized gradient approximation made simple. *Phys. Rev. Lett.* **77**, 3865 (1996).

30. Grimme, S., Antony, J., Ehrlich, S. & Krieg, H. A consistent and accurate ab initio parametrization of density functional dispersion correction (DFT-D) for the 94 elements H-Pu. *J. Chem. Phys.* **132**, 154104 (2010).

31. Kresse, G. & Joubert, D. From ultrasoft pseudopotentials to the projector augmented-wave method. *Phys. Rev. b* **59**, 1758 (1999).

32. Blöchl, P.E. Projector augmented-wave method. *Phys. Rev. B* **50**, 17953 (1994).

33. Brivio, F., Butler, K.T., Walsh, A. & Van Schilfgaarde, M. Relativistic quasiparticle self-consistent electronic structure of hybrid halide perovskite photovoltaic absorbers. *Phys. Rev. B* **89**, 155204 (2014).
34. Momma, K. & Izumi, F. VESTA: a three-dimensional visualization system for electronic and structural analysis. *J. Appl. Crystallogr.* **41**, 653-658 (2008).
35. Wang, V., Xu, N., Liu, J.-C., Tang, G. & Geng, W.-T. VASPKIT: A user-friendly interface facilitating high-throughput computing and analysis using VASP code. *Comput. Phys. Commun.* **267**, 108033 (2021).

Chapter 4

Molecular engineering for the orientation of the organic-inorganic hybrid perovskite for light emission

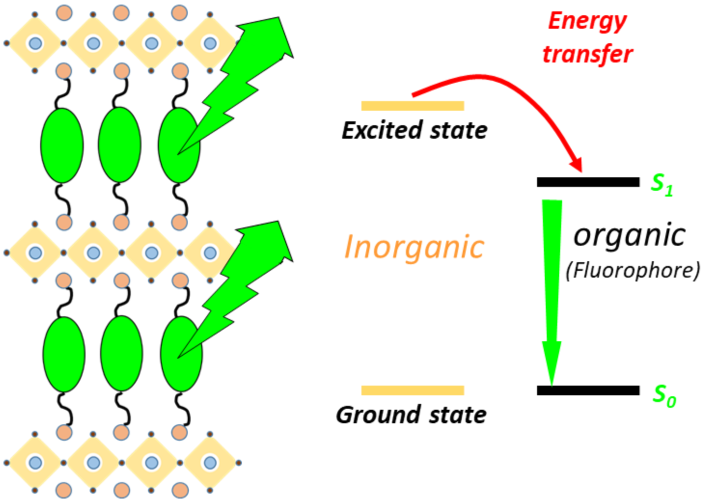

Chapter 4: Molecular engineering for the orientation of the organic-inorganic hybrid perovskite for light emission

4.1 Introduction

In the field of materials science, the quest for efficient and versatile luminescent materials has been a longstanding endeavor. Luminescent materials, which emit light when excited by an external energy source, have found applications in a wide range of technologies, including lighting, displays, sensors, and optoelectronic devices[1, 2]. Over the years, researchers have explored various classes of materials to harness their luminescent properties, aiming to develop materials with enhanced efficiency, stability, and tunability [1-4]. Among them, 2D hybrid halide perovskites with alternating organic and inorganic layers have created enormous excitements owing to their solution processability, structure-property tunability and excellent luminescent properties [5-10]. In most cases, the organic parts play solely a structural role in determining the quantum well structure because of its low dielectric constant. Recently, numerous molecules with tunable functionalities have been developed, giving more possibilities to 2D perovskite for light emission [11-13]. Agranovich et al. predicted that efficient energy transfer could happen between inorganic layers and organic layers through the exchange of Wannier-type excitons in inorganic layers and Frenkel-type excitons in organic layers of perovskite structure [14]. In the case of inorganic semiconductors, due to the high charge carrier mobilities and large density of electron-hole pairs that are generated by electrical injection, they are exceptionally suited as excitation sources. In contrast, most organic semiconductors that possess strong light-matter coupling and tunable functionalities are suitable for the role of the light emitter. The combination of organic and inorganic materials provides a platform for investigating energy transfer between them, and also exhibits superior potential for light emission. Our group reported that the OLEDs with a perovskite host doped with an organic fluorescent emitter exhibited a high singlet generation efficiency (SGE) of 40%, which broke the SGE limitation of 25% for conventional fluorescence-based OLEDs [15]. This result indicates that the combination of inorganic perovskite and organic fluorophores has great potential in LEDs. However, such a combination allows energy transfer from perovskites to organic emitters through the grain boundaries. This energy transfer process will lead to lots of unexpected nonradiative decay caused by the traps on the grain boundaries. Therefore, the organic fluorophores should ideally be used as a part of the perovskite structure to allow energy transfer through the inner structure as we introduced in the last chapter. Recently, efficient fluorescence and room temperature phosphorescence have also been achieved in the 2D hybrid perovskites with functional organic emitters [16, 17]. However, the devices using the hybrid perovskites for LEDs showed extremely low EQE, which is associated with a type II heterostructure formed by organic and inorganic components[18]. Our last chapter also confirms that the excitons will be dissociated at the type II heterointerface in the hybrid M1PB perovskite material, resulting in low PLQY. Therefore, a hybrid system with such band alignment is not suitable for light emission. Except for the band alignment of the inorganic layer and the organic layer, several other factors also limit the 2D hybrid perovskite system in light emission applications. Low charge mobilities are believed in low dimensional perovskites. The main reasons for such low charge mobilities could be ascribed to the horizontal orientation of the perovskite in which the charge carrier will be restricted by the organic components in a sandwich structure [19, 20]. Furthermore, organic components in perovskite hybrid structures should also possess high PLQY which is essential to the light emission. Consequently, to fabricate an efficient hybrid system in perovskite structure for light emission application, the system should meet several requirements, such as fast charge transport, efficient energy transfer from the inorganic part to the organic emitter, and high PLQY.

To meet these requirements, we designed several organic emitters named BT and 4mBT with two diamino groups. The hybrid system was successfully fabricated based on an organic-inorganic composition with the inorganic framework hosting these organic emitters. We found that the hybrid system, named BT/PB, and 4mBT/PB, respectively, formed a vertically oriented structure that allows the carriers to travel through the conducting inorganic layers in a sandwich structure. Additionally, these 2D perovskite films with type I heterostructure enable efficient energy transfer from an inorganic layer to an organic layer, resulting in high PLQYs of around 30%. The vertical-oriented films with efficient interlayer energy transfer show great potential for future light emission applications.

4.2 Results and Discussion

4.2.1 Synthesis and structure analyses of hybrid system

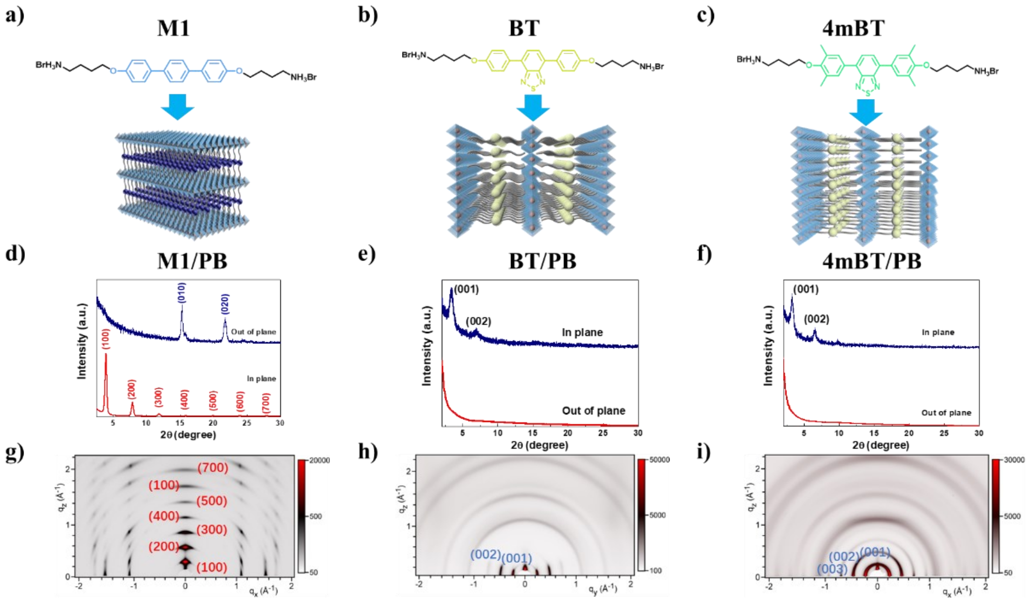

Figure 4.1. (a) Schematic diagram of M1 and 2D M1/PB perovskite structures; (b) Schematic diagram of BT and 2D BT/PB perovskite structures; (c) Schematic diagram of 4mBT and 2D 4mBT/PB perovskite structures; X-ray diffraction pattern of M1/PB (d), BT/PB (e), and 4mBT/PB (f) perovskite films, respectively. GIWAXS patterns of M1/PB (g), BT/PB (h), and 4mBT/PB (i) perovskite films.

The chemical structures of the designed diamine ligands, M1, BT, and 4mBT, are shown in **Figure** 1a-c. The synthesis and characterizations of these molecules are described in Experimental section. Using these newly designed organic fluorophores, hybrid films have been successfully fabricated through a simple spin-coating method. To examine the structure of these hybrid systems, we employed XRD and GIWAXS measurements, as shown in **Figure** 1d-i. The presence of a (*l*00) diffraction peak in XRD and the corresponding GIWAX map confirmed the formation of a horizontally-oriented M1/PB film. Interestingly, the BT/PB and 4mBT/PB films exhibited an unusual vertical-orientated structure. Additionally, the absorption spectra exhibited a distinct and sharp excitonic absorption peak, providing further evidence of the formation of a layered perovskite structure (**Figure** 4.2).

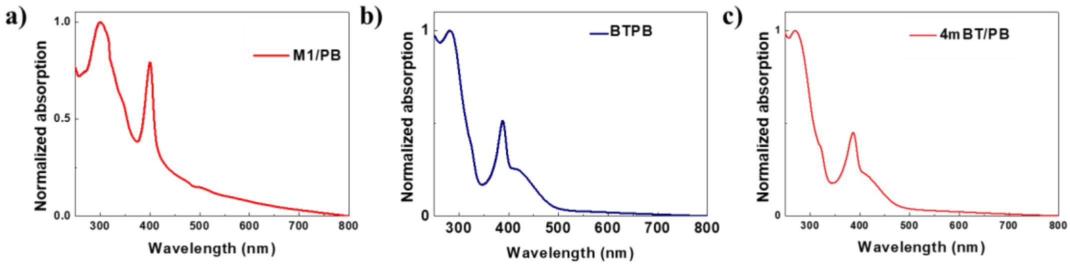

Figure 4.2 UV-vis absorption spectra of 2D M1/PB (a), BT/PB (b), and 4mBT/PB (c) neat films.

In order to gain a deeper understanding of the mechanisms underlying the unusual vertically oriented structures observed in BT/PB and 4mBT/PB, we conducted additional analyses, taking into account the effects of solvent, molecular composition, and temperature. Previous studies have noted that solvents can influence the orientation of perovskite films [19]. In our case, due to the strong π–π interactions and very low solubility in DMF (dimethylformamide), we opted to dissolve the M1/PB precursor in a highly polar solvent, DMSO (dimethyl sulfoxide), while using DMF for the BT/PB and 4mBT/PB precursors. To assess the impact of solvent on the orientation, we mixed DMF with DMSO during the formation of the BT/PB film. However, as evidenced by the XRD patterns depicted in **Figure** 4.3, no significant changes in the lamellar signals were observed, indicating that altering the solvent had minimal effect on the orientation of our perovskite films. Typically, most reported 2D perovskite films employing monoamine ligands exhibit a horizontal orientation, with the inorganic layer aligned parallel to the substrate. The primary reason for this horizontal orientation can be attributed to the weak van der Waals forces between two organic layers [21-23].

Furthermore, some studies have revealed that perovskite structures with enhanced interlayer molecular interactions tend to favor the formation of vertical orientation in low-dimensional perovskite structures [24, 25].

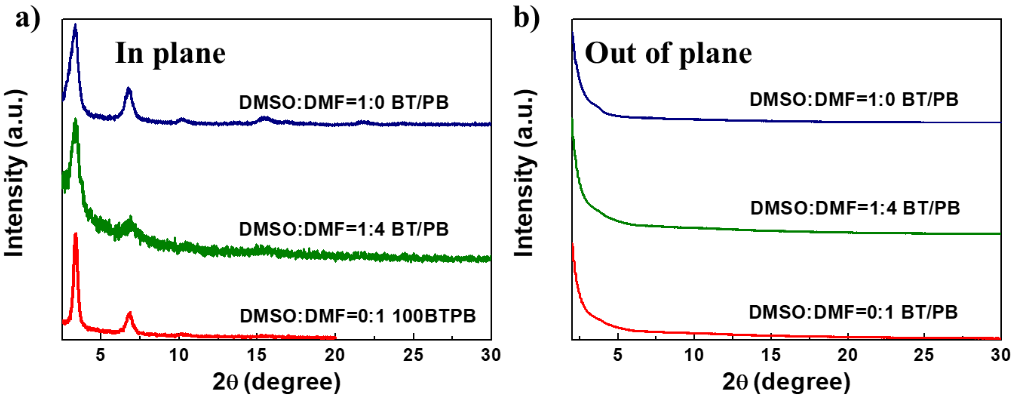

Figure 4.3 X-ray diffraction pattern of a BT/PB perovskite film fabricated by different ratios of DMF and DMSO.

In our study, we employed the diamine ligands BT and 4mBT, which possess relatively bulky substituents, resulting in weak intermolecular interactions, for the fabrication of perovskite films. The distinct orientation behaviors observed in M1/PB, BT/PB, and 4mBT/PB films suggest that the preferred direction of crystal growth varies depending on the organic diamine ligands used. Therefore, in an effort to understand the intermolecular interactions within the perovskite structures, we attempted to calculate intermolecular interactions. However, we were unable to obtain large crystals of BT/PB and 4mBT/PB that are suitable enough for single-crystal X-ray diffraction analysis, and only small powders were obtained from the anti-solvent diffusion method. This limitation can be attributed to the substantial steric hindrance introduced by the wide ligand, which hinders crystal growth to a significant size. To address this, we utilized the single crystal structure of M1/PB as a starting point and replaced M1 with BT and 4mBT, allowing us to obtain computational structures by relaxing them to the nearest local minimum. These computational structures of M1/PB, BT/PB, and 4mBT/PB align well with our experimental data, with interlayer spacing deviations of less than 3%, as depicted in **Figures** 4.4, 4.5, 4.6, and **Table** 4.1. These computational structures are sufficiently consistent with experimental results and can be used for further calculations.

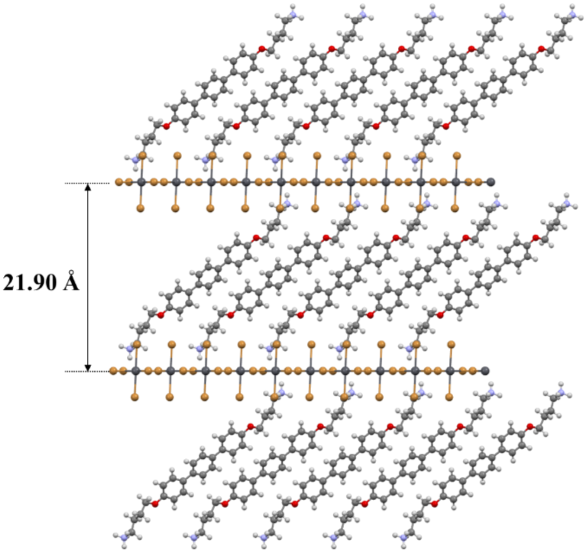

Figure 4.4 The crystal structure of M1/PB from density functional theory (DFT) calculation.

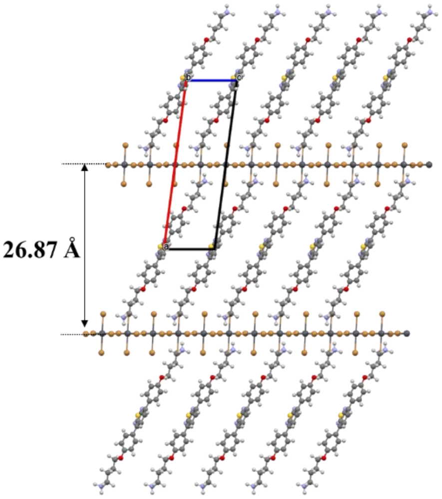

Figure 4.5 The crystal structure BT/PB from DFT calculation.

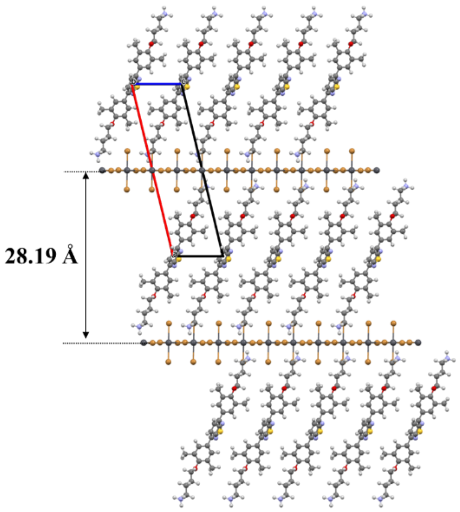

Figure 4.6 The crystal structure of 4mBT/PB from DFT calculation.

Table 4.1 The deviation in the interlayer spacing between experimental data and computational data for M1/PB, BT/PB, and 4mBT/PB.

Interlayer spacing	M1/PB	BT/PB	4mBT/PB
Experimental (XRD)	22.57 Å	26.14 Å	27.65 Å
Computational (DFT)	21.90 Å	26.87 Å	28.19Å
Deviation	2.9%	2.7%	1.9%

Based on these computational structures, we proceeded to calculate the intermolecular interaction on the (010) plane of the 2D perovskite structures using established methods from previous research [24]. As shown in **Figure** 4.7, the M1/PB perovskite exhibited the strongest intermolecular interaction of -6.40 eV on the (010) plane. BT/PB demonstrated a weaker intermolecular interaction of -5.97 eV on the (010) plane, while 4mBT/PB exhibited the weakest intermolecular interaction of -5.90 eV on the (010) plane. Conversely, we observed less change in the calculated organic-inorganic intermolecular forces on the (001) plane of M1/PB, BT/PB, and 4mBT/PB, as depicted in **Figure** 4.8. All the calculated data are summarized in **Table** 4.2. The different intermolecular interfaces observed on the (010) crystal planes play a role in influencing the balance of crystal growth. As illustrated in **Figures** 4.7d-f, the strong intermolecular interaction on the (010) plane dominates the crystal growth of M1/PB, resulting in a horizontal orientation. On the other hand, for BT/PB and 4mBT/PB, the decreased intermolecular interaction on the (010) planes likely alter the balance of preferential crystal growth direction, leading to a vertical orientation. Consequently, it appears that the strong intermolecular interaction on the (010) plane may promote the horizontal growth of perovskite crystals, such as in a 2D M1/PB perovskite film, whereas the weaker intermolecular interaction on the (010) plane may favor vertical growth, as observed in BT/PB and 4mBT/PB perovskite films.

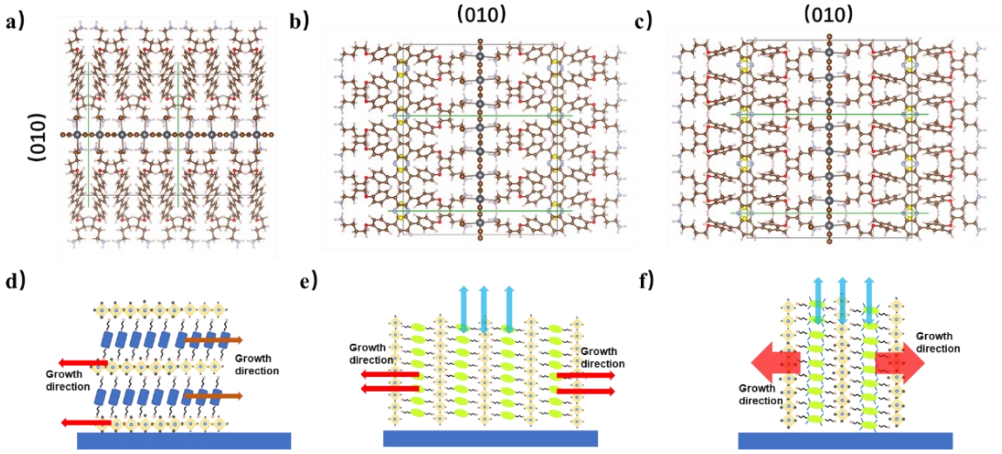

Figure 4.7 Ball-and-stick style models from DFT for intermolecular interaction of M1/PB (a), BT/PB (b), and 4mBT/PB (c), respectively. Schematic diagram of the proposed crystal growth mechanism for structure system of M1/PB (d), BT/PB (e), and 4mBT/PB (f), respectively.

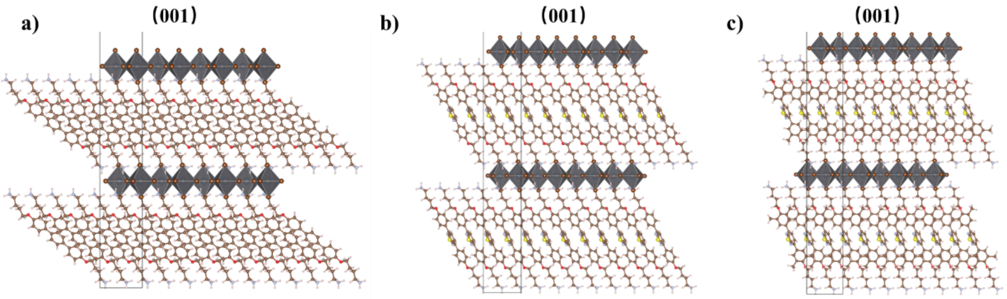

Figure 4.8 Ball-and-stick style models from DFT calculation for intermolecular interaction of M1/PB (a), BT/PB (b), and 4mBT/PB (c).

Table 4.2 Binding energy obtained from DFT calculation for M1/PB, BT/PB, and 4mBT/PB from different crystal planes.

Binding energy	M1/PB	BT/PB	4mBT/PB
(010)	6.40 eV	5.97 eV	5.90 eV
(001)	19.45 eV	19.27 eV	19.59 eV

According to previous reports [26], we recognize that additional parameters, such as the interaction between organic ligands and substrate, as well as annealing temperature, plays a crucial role in perovskite crystal growth and can significantly influence the perovskite orientation. In certain cases, if an organic ligand exhibits a preferential orientation that maximizes interactions between the crystal and the substrate, it can lead to a vertical orientation of the perovskite film. However, in this particular case, it is expected that BT and 4mBT may result in a horizontal orientation on the substrate due to their special interaction with the Si substrate. To assess the interaction between organic ligands and the substrate, we examined the orientation of pure ligands on the Si substrate. As shown in **Figure** 4.9, all ligands demonstrated a vertical orientation with the molecules perpendicular to the substrate, indicating that BT or 4mBT molecules do not exhibit strong interaction with the Si substrate. Then, we conducted investigations to explore the effect of annealing temperature on the orientation of the 2D perovskite films. As depicted in **Figure** 4.10, we observed no change in orientation for M1/PB and 4mBT/PB as the annealing temperature increased from 100 °C to 200 °C. These samples were referred to as 200M1/PB and 200-4mBT/PB, respectively. In contrast, the BT/PB perovskite film displayed a shift in orientation from vertical to horizontal when the annealing temperature was elevated from 100 °C to 200 °C, and we denoted this sample as 200BT/PB. Additionally, we noted a distinct change in a pure BT film, which exhibited lamellar signals in the out-of-plane XRD spectrum when annealed at 100 °C, but these signals vanished upon annealing at 200 °C (**Figure** 4.11). This disappearance suggests a transformation in the molecular packing of BT with varying annealing temperatures. Hence, one plausible explanation for the orientation change in the BT/PB film could be attributed to the altered molecular packing of BT.

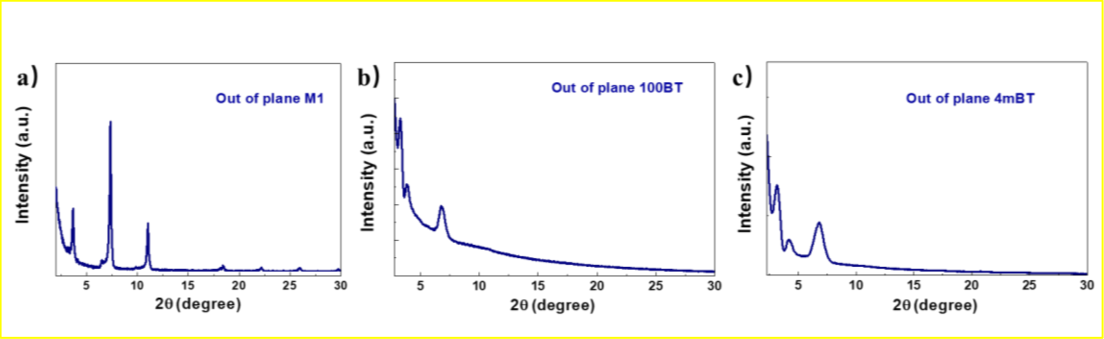

Figure 4.9 X-ray diffraction patterns of pure M1, BT, and 4mBT salt films annealed at 100 °C.

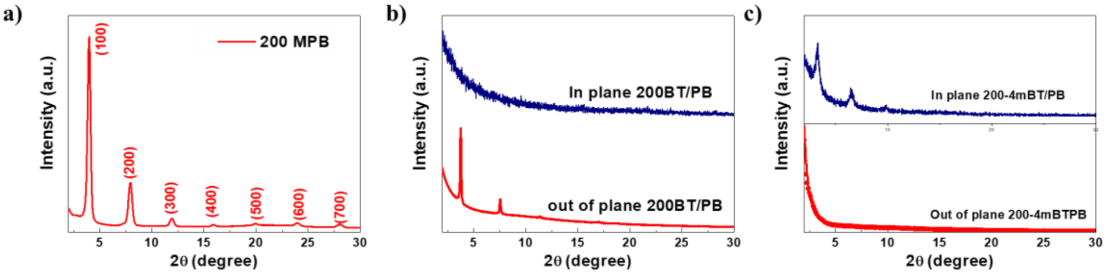

Figure 4.10 X-ray diffraction pattern of 200M1/PB (a), 200BT/PB (b), and 200-4mBT/PB(c) films.

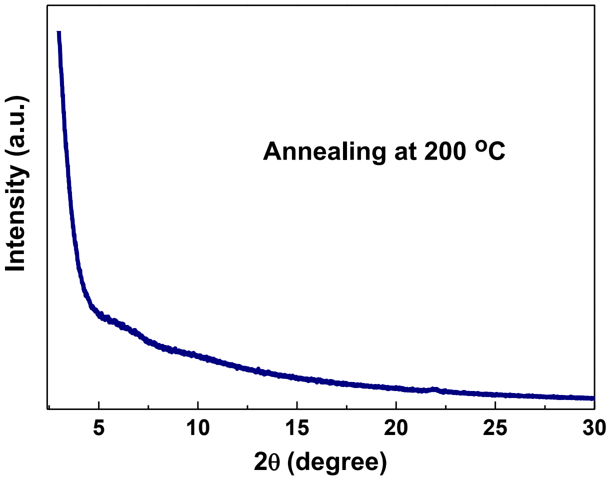

Figure 4.11 X-ray diffraction patterns of pure BT salt film annealed at different temperatures.

4.2.2 Energy band structures and charge-carrier dynamics

By employing a device with a sandwiched structure with two electrodes, we can assess the carrier transport properties through the conducting inorganic layers, independent of any constraints imposed by the organic layers when the film possesses a vertical orientation. On the other hand, horizontally oriented films are better suited for a planar structure that facilitates horizontal carrier transport. Therefore, it is valuable to evaluate the carrier transport properties of our 2D perovskite films using both electrode geometries. Given that previous findings have demonstrated the significance of band alignment between organic and inorganic components in carrier injection and transportation [27, 28], we initially estimated this alignment. For this purpose, we employed PES and LEIPS to evaluate the HOMO and LUMO of the perovskite films, as illustrated in **Figures** 4.12, 4.13, 4.14, 4.15 and **Table** 4.3.

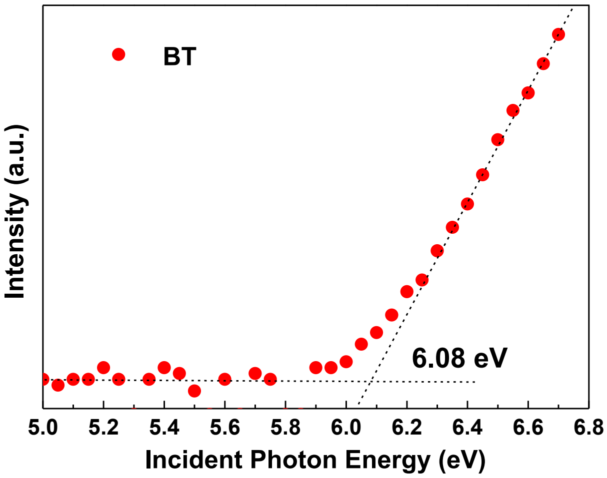

Figure 4.12 PES of pure BT salt film.

Table 4.3. Energy levels of 2D perovskite films.

	BT	4mBT	BT/PB	4mBT/PB
HOMO (eV)	-6.08	-6.08	-5.96	-5.96
LUMO (eV)	-2.53	-2.59	-2.71	-2.79

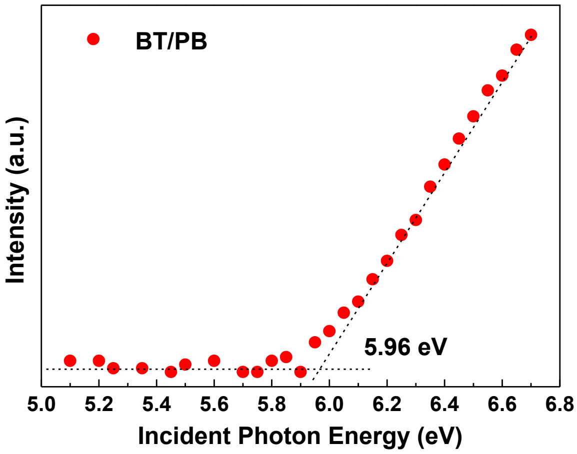

Figure 4.13 PES of 2D BT/PB perovskite film.

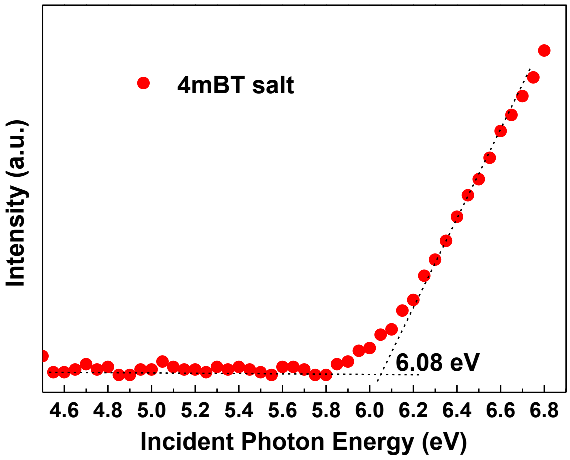

Figure 4.14 PES of pure 4mBT salt film.

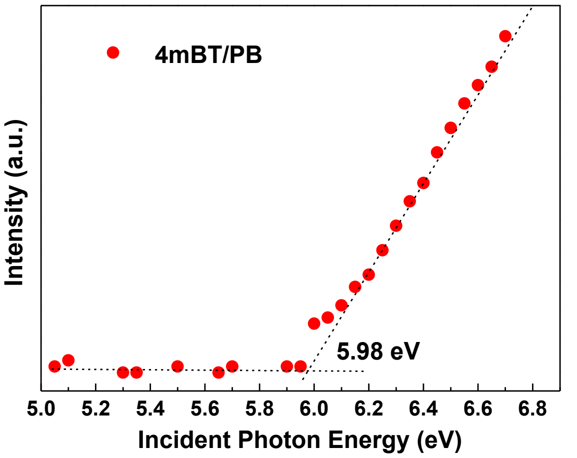

Figure 4.15 PES of 2D 4mBT/PB perovskite film.

The band alignment illustrations presented in **Figure** 4.16 reveal that the BT/PB and 4mBT/PB films exhibit a type I heterostructure, indicating that electrons and holes are predominantly confined within the inorganic layers. To understand the carrier transport behavior in our 2D perovskite films, we employed the dark space charge limited current (SCLC) method to evaluate their carrier transport properties. Previous studies have indicated that the Mott-Gurney law is sensitive to film thickness and may underestimate carrier mobilities when the film is very thin. In contrast, Geurst's SCLC model is thickness-independent and predicts more accurate values for carrier mobility [29, 30]. Therefore, we fabricated gap-type single carrier devices, specifically hole-only devices (HOD), which enable holes to transport horizontally. The structure of the HOD is depicted in **Figure** 4.17a, consisting of Au/MoOx/perovskite film/MoOx/Au layers. The corresponding energy levels of the HOD are illustrated in **Figure** 4.17b. In our investigation, we focused on BT/PB, 4mBT/PB, 200BT/PB, and 200-4mBT/PB perovskite films. The resulting current-voltage (I-V) curves are displayed in **Figure** 4.18. Among all the 2D perovskite films, only the 200BT/PB film exhibits an SCLC region in the I-V curves. Using Geurst's model, we calculated a hole mobility value of 0.7 $cm^2 \cdot S^{-1} \cdot V^{-1}$ as shown in the equation provided. [29-33].

$$I = (2W\varepsilon\varepsilon_{\circ}\mu V^2)/(\pi L^{2)})$$

where μ is the carrier mobility, W and L are the device width and length, ε is the vacuum permittivity, and $\varepsilon_{\circ}$ is the relative dielectric constant of 2D perovskite ($\varepsilon_{\circ}$=24) [34].

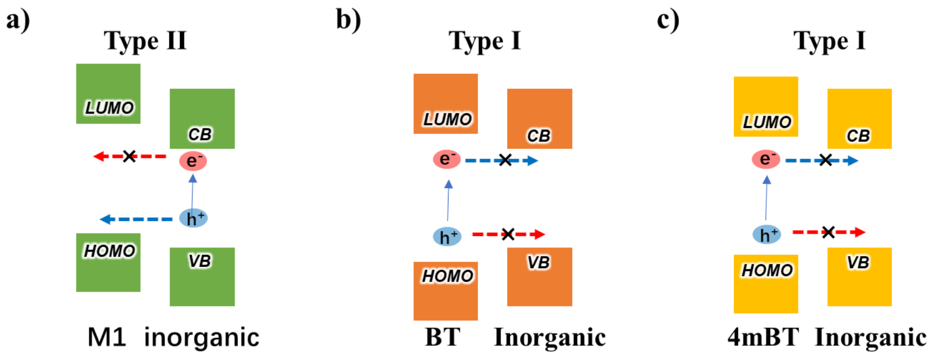

Figure 4.16 The band alignment of M1/PB (a), BT/PB (b), and 4mBT/PB (c) perovskite films.

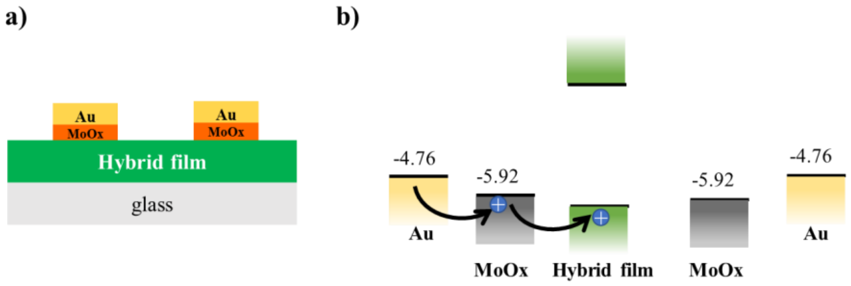

Figure 4.17 HOD structure (a) and the corresponding energy diagram (b).

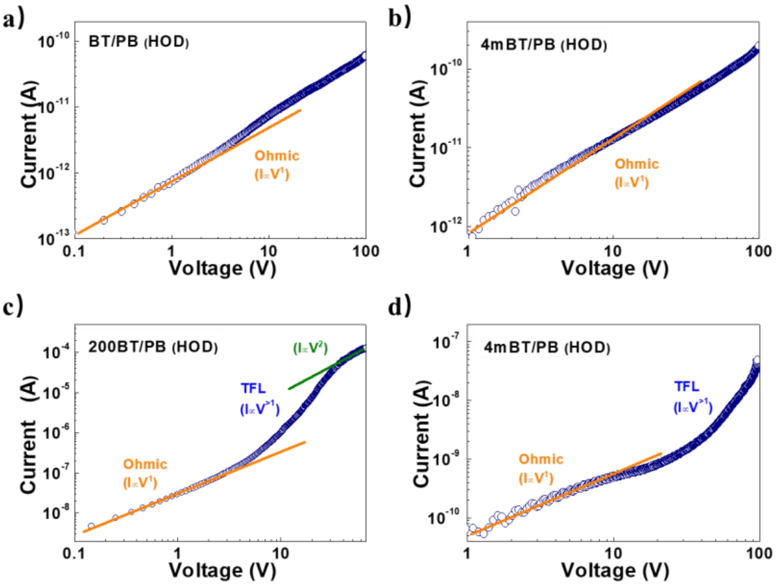

Figure 4.18 Current – Voltage (J-V) characteristics of BT/PB (a), 4mBT/PB (b), 200BT/PB (c), and 200-4mBT/PB (d) perovskite films.

By analyzing the ohmic region, we were able to calculate the electrical conductivity of our 2D perovskite films (**Table** 4.4). Notably, the 200BT/PB film, which exhibits a horizontal orientation, displayed the highest conductivity. Its conductivity was approximately five orders of magnitude higher than that of BT/PB and 4mBT/PB films with vertical orientation, and three orders of magnitude higher than that of the 200-4mBT/PB film. We also observed that the 200-4mBT/PB film exhibited higher electrical conductivity than the 4mBT/PB film. This difference could be attributed to the larger grain size and fewer grain boundaries observed in the AFM images of the 200-4mBT/PB film (**Figure** 4.19). The substantial contrast in conductivities between the horizontally and vertically oriented films aligns with previous findings [22, 35]. These results indicate that the 200BT/PB film, with its horizontal orientation, facilitates efficient carrier transport through planar structures. This characteristic renders it suitable for applications such as field-effect transistors (FETs), photodetectors, and light-emitting transistors (LETs). Conversely, vertically oriented BT/PB, 4mBT/PB, and 200-4mBT/PB films are more conducive to carrier transport within sandwich structures, making them well-suited for applications like light-emitting diodes (LEDs) and solar cells.

Table 4.4. Conductivities of 2D perovskite films.

Material	BT/PB	200BT/PB	4mBT/PB	200-4mBT/PB
Electrical conductivity (S/cm)	$2.44\text{x}10^{-9}$	$3.63\text{x}10^{-4}$	$5.78\text{x}10^{-9}$	$2.65\text{x}10^{-7}$

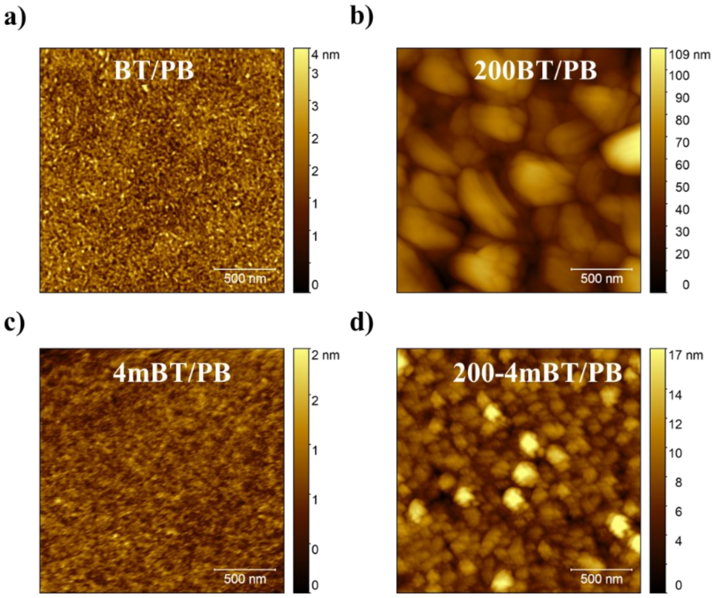

Figure 4.19 AFM images of BT/PB (a), 200BT/PB (b), 4mBT/PB (c), and 200-4mBT/PB (d) perovskite films.

4.2.3 Photophysical properties

In addition to carrier transport properties, the photophysical properties of our 2D perovskite films are also of great importance for future light emission applications. The optical spectra of these films are depicted in **Figure** 4.20. By analyzing the onset of the PL spectra (**Figure** 4.2), we were able to calculate the singlet state energy of the organic layers and the excited state energy level of the inorganic layers, as shown in **Figure** 4.20. Previous studies have suggested the potential for energy transfer between Wannier-type excitons in the inorganic layer and Frenkel-type excitons in the organic layers through FRET [14]. In our case, the emission observed in the M1/PB film likely originates from both the organic and inorganic components due to the presence of a Type II heterointerface between the organic and inorganic layers, as discussed in the previous Chapter 3.

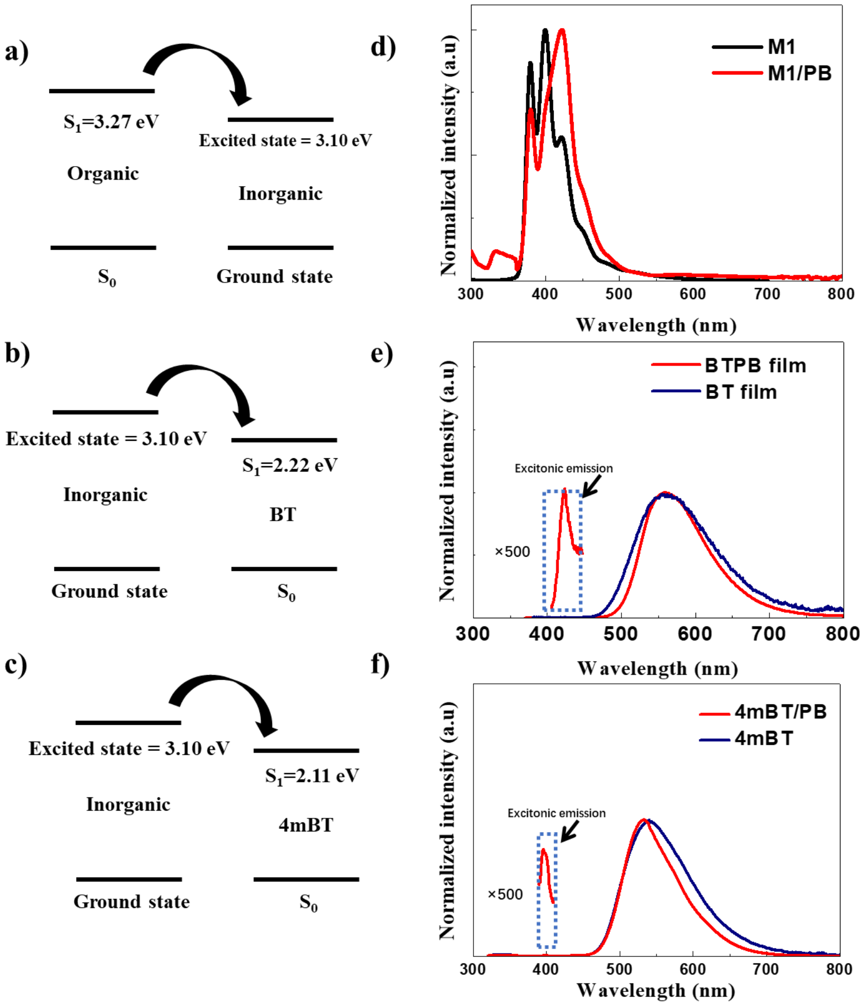

Figure 4.20 The excited-state energies for M1/PB (a), BT/PB (b), and 4mBT/PB (c) perovskite films. (d) normalized PL spectra of M1 and M1/PB films, (e) normalized PL spectra of BT and BT/PB films, (f) normalized PL spectra of 4mBT and 4mBT/PB films.

However, for BT/PB and 4mBT/PB films, we observed a broad emission spectrum similar to that of a BT molecule, along with a small residual excitonic peak originating from the inorganic layer. This suggests the occurrence of FRET from the inorganic to organic layers. The efficiency and time of energy transfer can be calculated using $\Phi_{ET} = 1 - \tau/\tau_0$ or $\Phi_{ET} = 1 - \eta/\eta_0$, $1/\tau = 1/\tau_0 + 1/\tau_{ET}$, where τ, and τ_0 represent the PL lifetime with and without quenchers, respectively. τ_{ET} is the energy transfer time, and η and η_0 are the corresponding quantum yields [11, 36]. To investigate the energy transfer efficiency and time, we utilized the **BT/PB**, a conventional 2D perovskite film with emission originating from the inorganic component, as a reference.

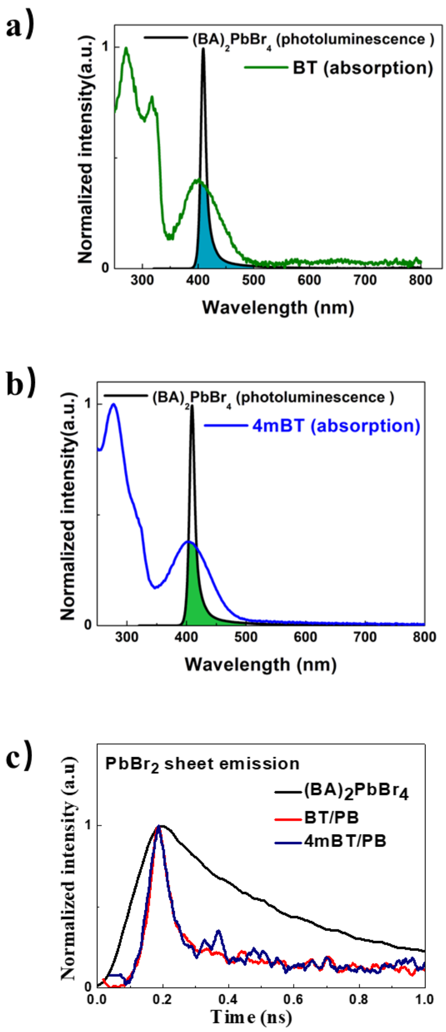

Figure 4.21 (a) The absorption spectrum of BT film and the emission spectrum of

BT/PB film. (b) The absorption spectrum of 4mBT film and the emission spectrum of BT/PB. (c) Time-resolved transient PL decay curves of the $PbBr_2$ emission for BT/PB, BT/PB, and 4mBT/PB perovskite films.

As shown in **Figures** 4.21a and b demonstrate significant spectrum overlaps between the BT/PB emission and the BT, and 4mBT absorption, indicating the FRET can happen between them. Time-resolved measurement was conducted on BT/PB, 4mBT/PB, and conventional 2D perovskite BT/PB films. As shown in **Figure** 4.21c, the shorter lifetime of inorganic emission in BTPB perovskite film indicates a high energy transfer efficiency Φ_{ET}= 89.7% from the inorganic to the organic layer. These high energy transfer efficiencies demonstrate that a significant portion of inorganic cations has been transferred to the organic singlet states. A similar trend was observed in 200BTPB and 200-4mBTPB films, as depicted in **Figure** 4.22. The energy transfer time, energy transfer efficiency, and PLQY of these 2D perovskite films are summarized in **Table** 4.5. 4mBT/PB film exhibits an energy transfer efficiency (Φ_{ET}) of 89.7%, while 200BT/PB and 200-4mBT/PB films display Φ_{ET} values of 90.2% and 90.4%, respectively. Furthermore, the PLQY of BTPB, 4mBTPB, 200BTPB, and 200-4mBTPB films are approximately 30%, 14%, 39%, and 17%, respectively. The relatively lower PLQY of 4mBTPB compared to BTPB can be attributed to different packing behaviors of organic fluorophores within the perovskite structures. The M1/PB perovskite film exhibits a very low PLQY of only 2%, which can be attributed to energy quenching at the type II interface. It is noteworthy that our systems consist solely of pure organic molecules, which can induce strong concentration quenching in the 2D perovskite structure. Therefore, introducing a "host" to reduce the fluorophore concentration in the 2D perovskite system could potentially improve the PLQY in future studies. BTPB and 4mBTPB perovskite films with vertical orientation and high PLQY hold promise for future light emission applications.

Table 4.5 Energy transfer time and efficiencies from inorganic layer to organic layer.

Material	BT/PB	200BT/PB	4mBT/PB	200-4mBT/PB
Energy transfer time (ps)	51	48	63	47
Energy transfer efficiency (%)	89.7	90.2	87.5	90.4

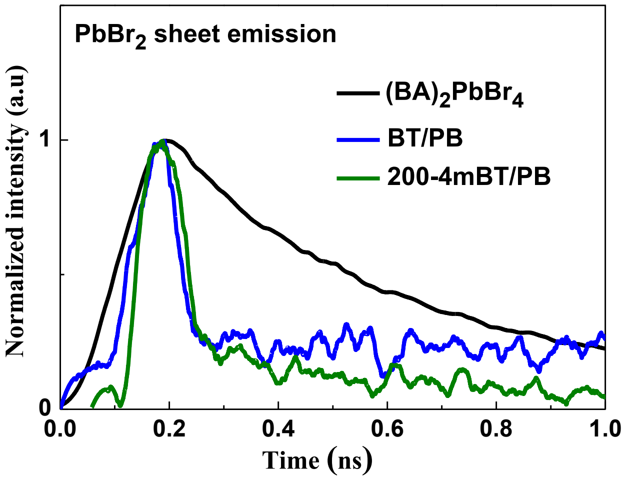

Figure 4.22 Time-resolved transient photoluminescence decay curves of the $PbBr_2$ emission for BT/PB, 200BT/PB, and 200-4mBT/PB perovskite films.

4.2.4 Photostability of the hybrid system

Light stability is a crucial factor for the successful implementation of these materials in practical applications. Therefore, we conducted light stability tests on all perovskite films by subjecting them to continuous excitation at 280 nm for several days, as depicted in **Figure** 4.23. Among the films, 200-4mBT/PB exhibited significantly higher photoluminescence (PL) stability, with a T_{50} value of approximately 110 hours. The 2D perovskite films annealed at 200 °C displayed enhanced PL stability compared to those annealed at 100 °C. This improvement can be attributed to the increased grain size and reduced formation of trapping sites when annealed at higher temperatures, as observed in **Figure** 4.19. In order to understand the distinct stability performances of the perovskite films, we conducted measurements on the stability of the pure organic film as well. As depicted in **Figure** 4.24, it is evident that among the organic films, the 200-4mBT film displays the longest PL lifetime. This indicates that the 200-4mBT film possesses inherent stability, which translates to a stable perovskite film structure. The combination of inorganic and organic fluorophores in these films demonstrates exceptional PL stability, underscoring their immense potential for future device applications.

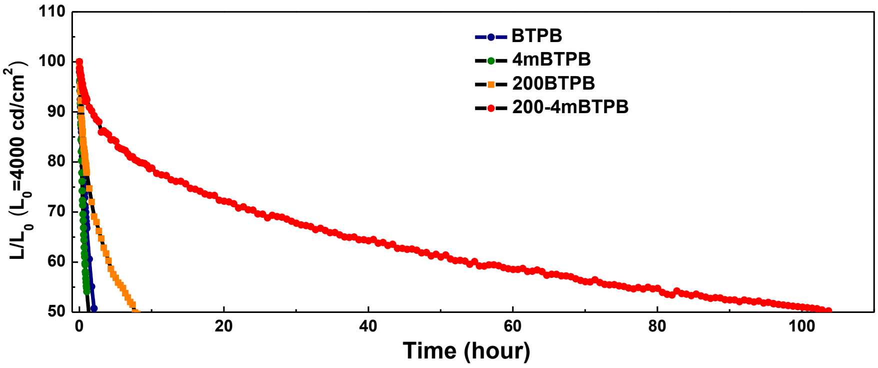

Figure 4.23 PL stability of BT/PB, 4mBT/PB, 200BT/PB, and 200-4mBT/PB films, respectively.

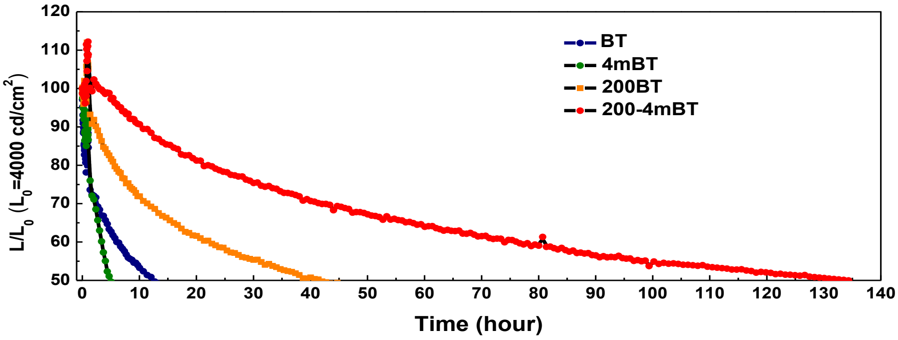

Figure 4.24 PL stability of BT, 4mBT, 200BT, and 200-4mBT films, respectively.

4.3 Summary

In summary, the incorporation of diamine ligands serves as an effective means to control the orientation of hybrid systems in the perovskite structure. Computational analysis suggests that the strong intermolecular interaction within the (010) plane promotes the horizontal growth of perovskite crystals, as observed in the 2D M1/PB perovskite film. Conversely, the weaker intermolecular interaction within the (010) plane favors vertical growth, as seen in the BT/PB and 4mBT/PB perovskite films. The distinctive conductivities exhibited by our 2D perovskite films align with their respective orientations in the gap-type device. Furthermore, the optical properties of these 2D perovskite films differ significantly. The broad emission observed in the BT/PB and 4mBT/PB films indicates energy transfer from the inorganic to organic layers, characteristic of a type I heterostructure. The energy transfer efficiencies within the perovskite structure are estimated to be approximately 90% from the inorganic to organic layers. These vertically oriented 2D perovskite films, with efficient interlayer energy transfer, hold great promise for future light emission applications utilizing such materials.

4.4 Experimental section

4.4.1 Materials and Methods

All commercially available chemicals and reagents were used without further purification. All reactions were monitored by analytical thin layer chromatography (TLC) purchased from Merck & Co., Inc.. Purification was carried out using a silica gel (200-300 nm) column.

4,4'-((benzo[c][1,2,5]thiadiazole-4,7-diylbis(4,1-phenylene))bis(oxy))bis(butan-1-aminium) bromide (BT) :

In a 250 mL two-neck round bottom flask fitted with a condenser, compound 6 (2.27 g 3.42 mmol) was dissolved in a mixture of THF (100 mL) and methanol (60 mL) at 45 oC under argon. The solution of aq. HBr (48%) (7.74 mL, 68.4 mmol) was injected into the reaction mixture, and stirred for 24 hrs. under argon. After cooled to room temperature, solvents were removed under reduced pressure, then precipitated in a mixture of methanol (10%) and dichloromethane (90%). The resulted product was further purified by washing with a mixture of methanol (10%) and dichloromethane (90%) (100 mL X 2), acetonitrile, isopropanol and diethyl ether (100 mL X 1) and finally pentane to yield a bright yellow solid (2.03g, 95.0%). 1H NMR (400 MHz, DMSO-d6) δ 8.01 (d, J = 9.2 Hz, 4H), 7.90 (s, 2H), 7.75 (s, 6H), 7.14 (d, J = 8.6 Hz, 4H), 4.12 (t, J = 6.1 Hz, 4H), 2.92 (t, J = 7.5 Hz, 4H), 1.85 (m, 4H), 1.77 (m, 4H). 13C NMR (101 MHz, DMSO) δ 159.13, 153.93, 131.69, 130.77, 129.74, 127.96, 115.05, 67.50, 39.13, 26.16, 24.41. HRMS calcd. for C26H30N4O2S (-2HBr) [M+H]+ 463.2162; found 463.2161

4,4'-((benzo[c][1,2,5]thiadiazole-4,7-diylbis(2,6-dimethyl-4,1-phenylene))bis(oxy)) bis(butan-1-aminium)dibromide (4mBT)

A 250 mL two-neck flask fitted with a condenser, compound 6 (5.5 g 7.65 mmol) was dissolved in 120 mL THF at 45 °C, then methanol (80 mL) was added under argon. The solution of aq. HBr (48%) (17.32 mL, 153.12 mmol) was injected to the reaction mixture, and stirred for 24 hrs. under argon. After cooled to room temperature, solvents were removed under reduced pressure, then precipitated in a mixture of methanol (10%) and dichloromethane (90%). The resulted product was further purified by washing with a mixture of methanol (10%) and dichloromethane (90%) (100 mL X 2), dichloromethane (100 mL X 1), acetone (100 mL X 1), diethyl ether (100 mL X 1) and finally pentane to yield a bright yellow solid (4.54 g, 86.5%). ^{1}H NMR (400 MHz, DMSO-*d*$_6$) δ 7.87 (s, 2H), 7.78 (s, 6H), 7.69 (s, 4H), 3.86 (t, *J* = 5.0 Hz, 4H), 2.93 (t, *J* = 6.4 Hz, 4H), 2.35 (s, 12H), 1.84 (m, 8H). ^{13}C NMR (101 MHz, DMSO) δ 156.21, 153.87, 132.75, 132.10, 130.91, 129.97, 128.35, 71.67, 39.29, 27.43, 24.56, 16.75. HRMS calcd for $C_{30}H_{38}N_4O_2S$ (-2HBr) $[M+H]^+$ 519.2788; found 519.2773.

2D perovskite thin films fabrication: M1/PB, BT/PB and 4mBT/PB perovskite precursor solutions (0.1 M) were prepared by dissolving the organic salts and lead bromide ($PbBr_2$) (99,999%, Aldrich) with a 1: 1 molar ratio in anhydrous DMSO or DMF. The solutions were stirred for 3 hours until the complete dissolution of the precursors. Anhydrous DMSO (99.8%, Sigma–Aldrich) or DMF (99.8%, Sigma–Aldrich) was purchased in a septum-sealed bottle and stored in a nitrogen-filled box prior to use. All the depositions were performed in a glove box. Quartz substrates were cleaned ultrasonically and sequentially with acetone, isopropanol and deionized water, then dried in an oven, and finally exposed to ultraviolet light and ozone for about 10 min. The perovskite materials were then deposited by spin-coating the precursor solutions at 3000 rpm for 60 seconds. The perovskite layers were formed after annealing at 70 °C for 10 minutes 100 °C for 5 minutes. Organic salt reference layers were obtained by dissolving organic salt in anhydrous DMSO. The organic solution was then deposited on quartz by spin-coating at 2000 rpm for 60 seconds, followed by annealing at 70 °C for 10 minutes 100 °C for 5 minutes.

4.4.2 Characterization

UV-vis absorption spectra and steady-state PL spectra: UV-vis absorption spectra for all the samples were measured on Lambda 950 KPA spectrophotometer (PerkinElmer, USA). Steady-state PL spectra were recorded using an FP-8600 PL spectrometer (JASCO, Japan).

PES and LEIPS: The energy levels of all the films used in this study were measured by photoelectron yield spectroscopy (AC-3, Riken Keiki) or low-energy inverse photoemission spectroscopy (LE-1, ALS Technology) and the samples used for the energy-level measurements consisted of 10-nm-thick films spin-coated on ITO-coated glass substrates.

Atomic force microscopy (AFM): The morphology of 2D perovskite thin films, which were spin-coated on SiO_2/Si substrates in a nitrogen-filled glove box with oxygen and moisture levels less than 1 ppm, were measured using an atomic force microscope (JSPM-5400, JEOL) in amplitude-modulation mode.

Out-of-plane and in-plane X-ray diffraction (XRD): Out-of-plane and in-plane XRD patterns of 2D perovskite thin films were measured with a Rigaku Smart Lab using a Cu Kα source (λ = 1.54056 Å). All the manipulations of XRD measurement were performed under ambient condition.

Grazing Incidence Wide-Angle X-ray Scattering (GIWAXS): GIWAXS measurements were carried out at PLS-II 9A U-SAXS beamline of Pohang Accelerator Laboratory (PAL) in Korea. Samples consisted of layers on silicon wafer of twenty to forty nanometers in thickness. The X-rays coming from the vacuum undulator (IVU) were monochromated using Si(111) double crystals and focused on the detector using K-B type mirrors. Patterns were recorded with a Rayonix 2D SX 165 CCD detector. The sample-to-detector distance was about 221 mm for energy of 11.08 keV (1.119 Å).

Computational method. The first-principles calculations were performed using the plane-wave pseudopotential method within the framework of DFT as implemented in the Vienna Ab initio Simulation Package. The intermolecular interaction was described using frozen-core projected augmented-wave pseudopotentials44. The generalized gradient approximation formulated by Perdew, Burke and Ernzerhof was used as the exchange-correlation functional. We used a kinetic energy cutoff of 400 eV for wavefunction expansion and a 4×4×1 Monkhorst–Pack k-point mesh for electronic Brillouin zone integration of 2D hybrid halide perovskites. The structures (including lattice parameters and internal atomic positions) were fully optimized via total energy minimization, with the total energy converged to less than 0.0001 eV.

Hole-only device (HOD) fabrication and measurements: Device fabrication was performed inside a nitrogen-filled glove box with oxygen and water level less than 1 ppm. The Si wafers coated with a 300 nm SiO_2 dielectric layer were used as substrates for film preparation. The substrates were cleaned sequentially by ultrasonication in detergent solution, pure water, acetone, and isopropanol for 10 min each, and dried using a nitrogen gun. Then, the substrates were treated with UV-ozone for 30 min, and transferred into a glove box for further use. The perovskite materials were then deposited on the Si wafer by spin-coating the precursor solutions at 3000 rpm for 60 seconds. The perovskite layers were then formed after annealing at 70 °C for 10 minutes

100 °C for 5 minutes. The HOD was fabricated by vacuum deposition process without exposure to ambient air. MoO_X and Au were deposited above the 2D perovskite films at 0.2 and 1 Å/s, respectively. The mask with 30 μm gap HOD fabrication. The *I-V* measurements were performed using a Keithley 2400 source meter and an absolute external quantum efficiency (EQE) measurement system (C9920-12, Hamamatsu Photonics, Japan).

4.5 References

1. Feldmann, C., Jüstel, T., Ronda, C.R. & Schmidt, P.J. Inorganic luminescent materials: 100 years of research and application. *Adv. Funct. Mater.* **13**, 511-516 (2003).
2. Kitai, A. Luminescent materials and applications. (John Wiley & Sons, 2008).
3. Blasse, G. The physics of new luminescent materials. *Mater. Chem. Phys.* **16**, 201-236 (1987).
4. Edgar, A. Luminescent materials. *Springer Handb. Electron. Photon. Mater*. **1**, 1(2017).
5. Liu, Y. et al. Surface-tension-controlled crystallization for high-quality 2D perovskite single crystals for ultrahigh photodetection. *Matter* **1**, 465-480 (2019).
6. Passarelli, J.V. et al. Enhanced out-of-plane conductivity and photovoltaic performance in n=1 layered perovskites through organic cation design. *J. Am. Chem. Soc.* **140**, 7313-7323 (2018).
7. Wang, K. et al. Lead-free organic–perovskite hybrid quantum wells for highly stable light-emitting diodes. *ACS nano* **15**, 6316-6325 (2021).
8. Wang, N. et al. Perovskite light-emitting diodes based on solution-processed self-organized multiple quantum wells. *Nat. Photon.* **10**, 699-704 (2016).
9. Yu, D. et al. Broadband and sensitive two-dimensional halide perovskite photodetector for full-spectrum underwater optical communication. *Nano Res.* **14**, 1210-1217 (2021).

10. Zhang, L. et al. Room-temperature electrically switchable spin–valley coupling in a van der Waals ferroelectric halide perovskite with persistent spin helix. *Nat. Photon.* **16**, 529-537 (2022).

11. Hu, H. et al. Efficient Room-Temperature Phosphorescence from Organic–Inorganic Hybrid Perovskites by Molecular Engineering. *Adv. Mater.* **30**, 1707621 (2018).

12. Li, X. et al. Two-dimensional halide perovskites incorporating straight chain symmetric diammonium ions,$(NH_3CmH_2mNH_3)(CH_3NH_3)_{n-1}Pb_nI_{3n+1}$(m=4-9; n=1-4). *J. Am. Chem. Soc.* **140**, 12226-12238 (2018).

13. Nussbaum, S. et al. Tuning Napththalenediimide Cations for Incorporation into Ruddlesden–Popper-Type Hybrid Perovskites. *Chem. Mater.* **34**, 3798-3805 (2022).

14. Agranovich, V., La Rocca, G. & Bassani, F. Efficient electronic energy transfer from a semiconductor quantum well to an organic material. *J. Exp. Theor. Phys. Lett.* **66**, 748-751 (1997).

15. Matsushima, T. et al. Enhanced Electroluminescence from Organic Light-Emitting Diodes with an Organic–Inorganic Perovskite Host Layer. *Adv. Mater.* **30**, 1802662 (2018).

16. Ema, K., Inomata, M., Kato, Y., Kunugita, H. & Era, M. Nearly perfect triplet-triplet energy transfer from Wannier excitons to naphthalene in organic-inorganic hybrid quantum-well materials. *Phys. Rev. Lett.* **100**, 257401 (2008).

17. Saparov, B. & Mitzi, D.B. Organic–inorganic perovskites: structural versatility for functional materials design. *Chem. Rev.* **116**, 4558-4596 (2016).

18. Liu, C. et al. Tunable semiconductors: control over carrier states and excitations in layered hybrid organic-inorganic perovskites. *Phys. Rev. Lett.* **121**, 146401 (2018).

19. Chen, A.Z. & Choi, J.J. Crystallographic orientation and layer impurities in two-dimensional metal halide perovskite thin films. *J. Vac. Sci. Technol. A: Vac. Surf. Films* **38**, 010801 (2020).

20. Ajayakumar, A., Muthu, C., V. Dev, A., Pious, J.K. & Vijayakumar, C. Two-Dimensional Halide Perovskites: Approaches to Improve Optoelectronic Properties. *Chem. Asian J.* **17**, e202101075 (2022).
21. Gedda, M. et al. Ruddlesden–Popper-Phase Hybrid Halide Perovskite/Small-Molecule Organic Blend Memory Transistors. *Adv. Mater.* **33**, 2003137 (2021).
22. Matsushima, T. et al. Intrinsic carrier transport properties of solution-processed organic–inorganic perovskite films. *Appl. Phys. Express.* **10**, 024103 (2017).
23. Xu, Y., Wang, M., Lei, Y., Ci, Z. & Jin, Z. Crystallization kinetics in 2D perovskite solar cells. *Adv. Energy Mater.* **10**, 2002558 (2020).
24. Ren, H. et al. Efficient and stable Ruddlesden–Popper perovskite solar cell with tailored interlayer molecular interaction. *Nat. Photon.* **14**, 154-163 (2020).
25. Ji, T. et al. Crystallization regulation of solution-processed two-dimensional perovskite solar cells. *J. Mater. Chem. A* **10**, 13625-13650 (2022).
26. Tsai, H. et al. High-efficiency two-dimensional Ruddlesden–Popper perovskite solar cells. *Nature* **536**, 312-316 (2016).
27. Dunlap-Shohl, W.A. et al. Tunable internal quantum well alignment in rationally designed oligomer-based perovskite films deposited by resonant infrared matrix-assisted pulsed laser evaporation. *Mater. Horiz.* **6**, 1707-1716 (2019).
28. Lédée, F. et al. Tetrazine molecules as an efficient electronic diversion channel in 2D organic–inorganic perovskites. *Mater. Horiz.* **8**, 1547-1560 (2021).
29. Geurst, J. Theory of space-charge-limited currents in thin semiconductor layers. *Phys. Status Solidi (B)***15**, 107-118 (1966).
30. Zuleeg, R. & Knoll, P. Space-charge-limited currents in heteroepitaxial films of silicon grown on sapphire. *Appl. Phys. Lett.* **11**, 183-185 (1967).
31. Lee, L. et al. Wafer-scale single-crystal perovskite patterned thin films based on geometrically-confined lateral crystal growth. *Nat. Commun.* **8**, 15882 (2017).
32. Fu, L. et al. Both Boceprevir and GC376 efficaciously inhibit SARS-CoV-2 by targeting its main protease. *Nat. Commun.* **11**, 4417 (2020).
33. Zubair, M., Ang, Y.S. & Ang, L.K. Thickness dependence of space-charge-

limited current in spatially disordered organic semiconductors. *IEEE Trans. Electron Devices* **65**, 3421-3429 (2018).

34. Ma, K. et al. Organic Cation Engineering for Vertical Charge Transport in Lead-Free Perovskite Quantum Wells. *Small Sci.* **1**, 2000024 (2021).

35. Lin, Y. et al. Unveiling the operation mechanism of layered perovskite solar cells. *Nat. Commun.* **10**, 1008 (2019).

36. Schlesinger, R. et al. Efficient light emission from inorganic and organic semiconductor hybrid structures by energy-level tuning. *Nat. Commun.* **6**, 6754 (2015).

Chapter 5:

Multi-component organic layers based on H-G systems in organic-inorganic 2D perovskites for efficient light emission

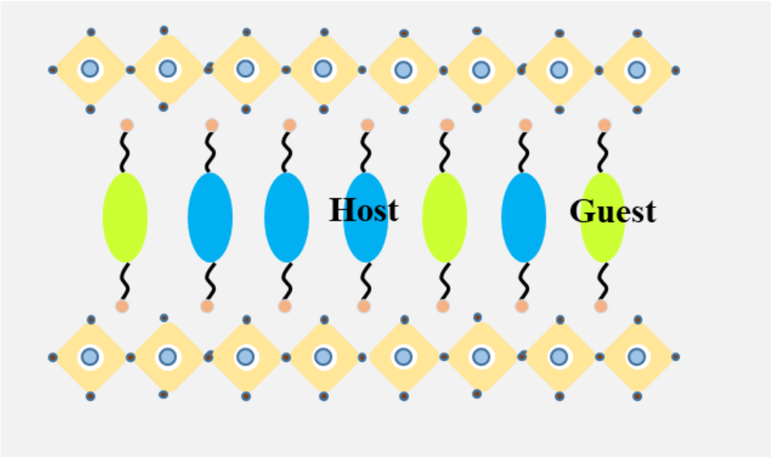

Chapter 5: Multi-component organic layers based on H-G systems in organic-inorganic 2D perovskites for efficient light emission

5.1 Introduction

Luminescent materials, which emit light when stimulated by an external energy source, have revolutionized various fields of science and technology. Their ability to convert energy into visible light has made them indispensable in applications such as lighting, displays, sensors, and optoelectronic devices[1-4]. Over the years, researchers have explored diverse classes of luminescent materials, constantly pushing the boundaries of efficiency, stability, and versatility[3, 4]. One class of luminescent materials that has attracted significant attention and transformed the landscape of optoelectronics is perovskites[5, 6]. Historically, luminescent materials such as organic dyes and inorganic phosphors dominated the field, offering certain advantages but also facing limitations in terms of efficiency, stability, and fabrication techniques[7, 8]. The advent of perovskite materials, particularly in the form of hybrid organic-inorganic structures, has disrupted this landscape by introducing exceptional optical properties and unprecedented possibilities. Traditionally, perovskites were known for their three-dimensional crystal structure, but the exploration of layered 2D perovskites has uncovered intriguing possibilities in the realm of light emission [9, 10]. Layered 2D perovskites, composed of inorganic layers separated by organic spacer molecules, offer several advantages for light emission applications [11-13].

In the previous chapter, we introduced the concept that efficient energy transfer can occur from an inorganic host to an organic emitter in a 2D layered perovskite structure. However, the layered structure of the hybrid material can potentially cause strong concentration quenching of the organic emitting layers, especially if these layers are formed by pure organic emitters. To reduce this concentration quenching effect, the dispersion of the organic emitters within the perovskite structure using additional hosts seems an interesting strategy. To this end, a host-guest (H-G) system can be utilized as organic sublayers and confined between the perovskite inorganic layers[14-16]. By incorporating a H-G system in a 2D perovskite structure, the light emission efficiency of the organic emitters is expected to be enhanced, due to the decreasing of the dyes aggregation and non-radiative processes.

In this chapter, our investigation focuses on the design and photophysical properties of multicomponent H-G systems in 2D perovskite structures. These H-G systems involve the combination of organic hosts, organic emitters and inorganic materials within the same 2D perovskite framework. The aim is to understand the influence of the molecular size and energy level differences between the host and guest molecules on the overall performance of the system. By examining the experimental results, we gain valuable insights into the design rules for developing high-performance, multicomponent H-G systems in perovskite structures specifically tailored for light-emitting applications.

5.2 Results and Discussions

5.2.1 Characterization of multi-component H-G systems

The structure of hosts, inorganic materials, and guest emitters used in this chapter are depicted in **Figure** 5. 1. The four hosts used in this study are different ammonium salts named phenethyl ammonium (M0), M1 (see Chapter 3), (((2',5'-difluoro-[1,1':4',1''-terphenyl]-4,4''-diyl)bis(oxy))bis(butane-4,1-diyl))bis(bromo-l5 azane) (M2), and decyl ammonium bromide (M3), respectively. For inorganic materials, we employed Pb and Br as the metal and halide ions, respectively. The organic hosts and the BT emitter were introduced into the inorganic framework to form a layered 2D perovskite structure. The absorption spectra of the thin films of the pure BT, the BT-based 2D perovskite BTPB, and the H-G system-based 2D perovskites MxBT/PB (5 mol% BT) are shown in **Figure** 5. 2a. All the MxBT/PB absorption spectra present an excitonic peak ranging from 390 nm to 400 nm which is consistent with the excitonic peak in the BT/PB film. This suggests the formation of the 2D perovskite structure (quantum well) in the multi-component hybrid perovskites MxBT/PB.

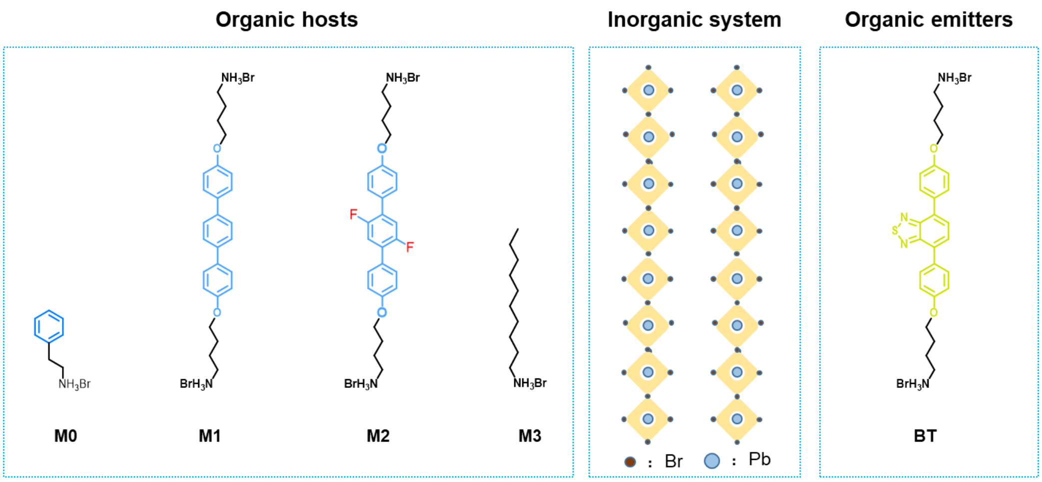

Figure 5. 1 Chemical structures of the organic hosts and BT emitter, and the inorganic system utilized in this chapter.

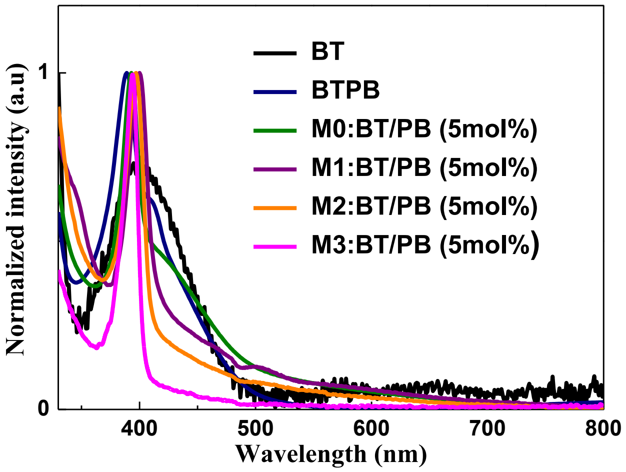

Figure 5. 2 Absorption spectra of the organic emitter, the 2D perovskite BT/PB perovskite, and the H-G system-based 2D perovskites, MxBT/PB, with molar ratio host:BT = 90:5.

5.2.2 Photophysical properties of multi-component H-G systems

As shown in **Figures** 5. 3, 5. 4, 5. 5, and 5. 6, the H-G system-based 2D perovskites MxBT/PB exhibit a residual emission around 400 nm which is consistent with the emission peak of their single component perovskite (perovskite with only host molecules). The PLQYs of these films were measured at the excitation wavelength of 430 nm (only the emitter is excited) and summarized in **Table** 5.1. For M0:BT/PB, the

PLQY is found to be around 30%, which is similar to that measured for BT/PB indicating no specific improvement. That can be explained by the significant difference of the molecular length between M0 host and BT guest. Unfortunately, the blend of M0 and BT salts in the precursor solution leads after spin-coating to the formation of two distinct perovskite phases, M0/PB and BT/PB, as evidenced by the two residual peaks around 400 and 410 nm in M0:BT/PB film as seen in **Figure** 5. 3. These two peaks correspond to the coexistence of both BT/PB and M0/PB phases, respectively, indicating the formation of separated phases in the M0:BT/PB layer. As a result, the similar PLQY observed for BT/PB and M0:BT/PB can be ascribed to the formation and the presence of BT/PB domains within the film preventing the dispersion of the BT dyes. In contrast, when the hosts have similar molecular sizes to the BT guest emitter, such as M1, M2, and M3, the films of the hybrid multi-component perovskites MxBT/PB exhibit strong PL emission from the BT emitter (**Figures** 5. 4, 5. 5, and 5. 6) and significant improvements on the PLQY when excited at 430 nm as seen in **Table** 5. 1. This PLQY enhancement could be attributed to the reduction of the concentration quenching of the BT emitters in M1:BT/PB, M2:BT/PB, and M3:BT/PB, due to efficient dispersion of BT emitting salts within the host salt layers to form homogeneous phases of MxBT/PB perovskites.

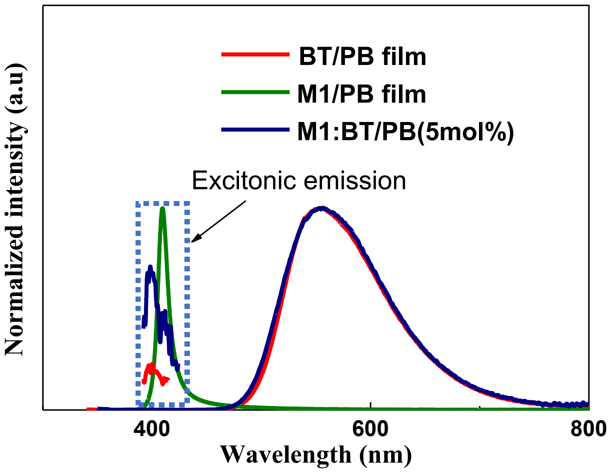

Figure 5. 3 PL spectra of the thin films of BT/PB, M0/PB, and M0:BT/PB (ratio host:BT = 90:5).

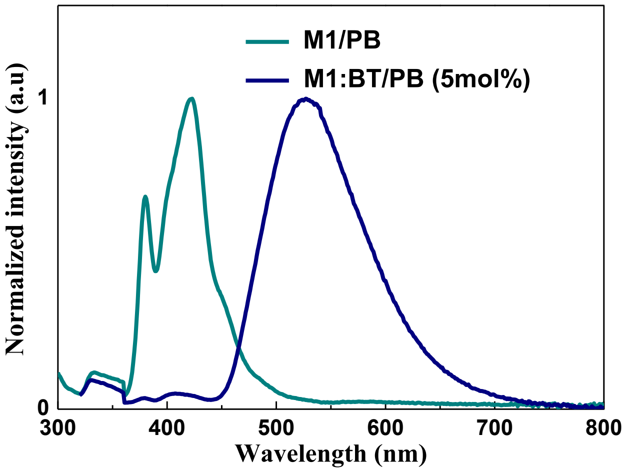

Figure 5. 4 PL spectra of M1/PB and M1:BT/PB 2D perovskite films using M1 as organic salt and host (ratio host:BT = 90:5).

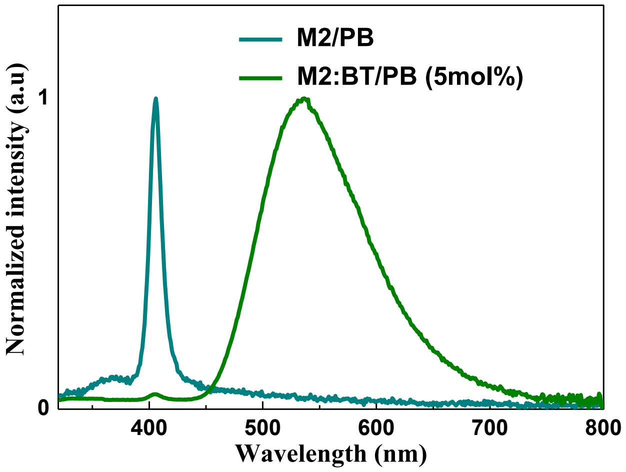

Figure 5. 5 PL spectra of M2/PB and M2:BT/PB 2D perovskite films using M2 as organic salt and host (ratio host:BT = 90:5).

Table 5. 1 PLQY of BT/PB and MxBT/PB 2D perovskite thin films (ratio host:BT = 90:5).

PLQY	BT/PB	M0:BT/PB	M1:BT/PB	M2:BT/PB	M3:BT/PB
(λ_{exc}) 430nm	29	30	46	55	59

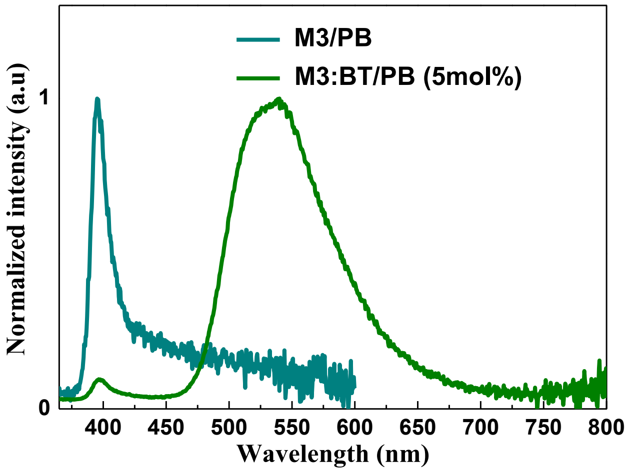

Figure 5. 6 PL spectra of M3/PB and M3:BT/PB 2D perovskite films using M3 as organic salt and host (ratio host:BT = 90:5).

Based on the successful strategy of the host-guest system as organic emitting layers, we investigated the effect of the BT emitter concentration (ratio host:BT) in the M1:BT/PB, M2:BT/PB and M3:BT/PB 2D perovskites. As shown in **Figures** 5. 7, 5. 8, and 5. 9, all the MxBT/PB films show a board and intense emission corresponding to the fluorescence of BT emitters, which is gradually redshifted as the BT concentration is increased. This redshift can be explained by the increasing the polarity of the organic medium with the BT concentration increase due to the substantial ground-state dipole moment of the BT emitters. In addition, with the BT concentration increases, the progressive disappearance of the residual emission peak (at 400nm) of the inorganic layers was observed, indicating an efficient energy transfer from hosts to the guest emitters.

Interestingly, the PLQYs also show different behaviors depending on the excitation wavelengths. As shown in **Figure** 5. 10, the PLQYs of M1:BT/PB significantly increase as the BT concentration decreases when the film is excited at 430 nm (excitation of the BT guest only). However, the PLQYs show a large decrease when the film is excited at 400 nm (excitation of the BT guest and inorganic layers) and 280 nm (excitation of the BT guest, host and inorganic layers). The reduction of the PLQYs implies that the M1 host is a quencher in M1:BT/PB system. As we introduced in Chapter 3, the HOMO energy level of M1 is shallower than the inorganic energy level, leading to the formation of a type II M1-inorganic heterointerface in M1PB. Thus, the decline of PLQYs can be attributed to the type II heterostructure formed by M1 and inorganic layers in M1:BT/PB perovskite. The proposed band alignment scheme is depicted in **Figure** 5.11. In conclusion, to confine the excitons and improve the PLQY, a host with a deeper HOMO energy level is needed.

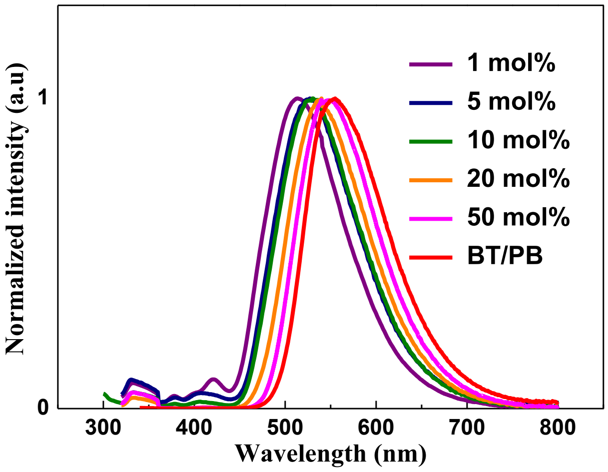

Figure 5. 7 PL spectra of M1:BT/PB perovskite films with different BT concentrations.

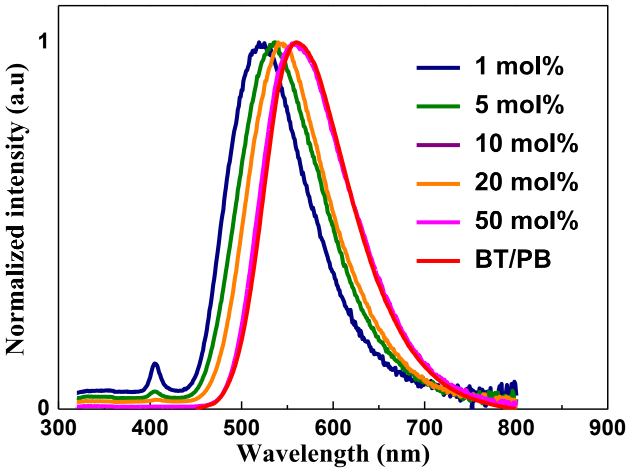

Figure 5. 8 PL spectra of M2:BT/PB perovskite films with different BT concentrations.

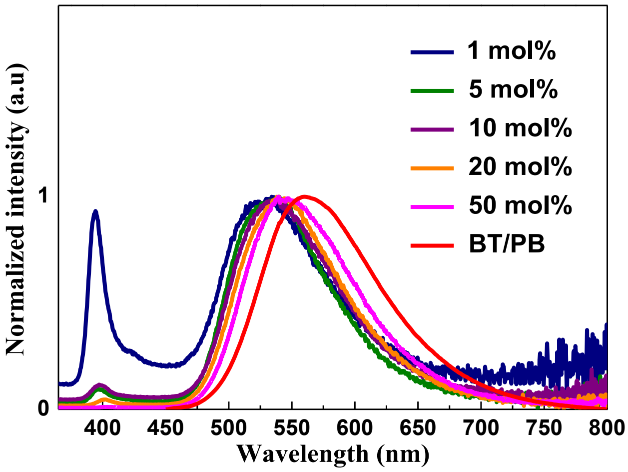

Figure 5. 9 PL spectra of M3:BT/PB perovskite films with different BT concentrations.

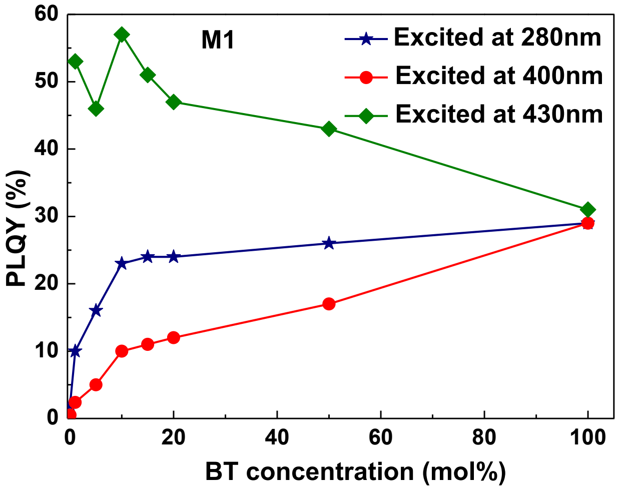

Figure 5. 10 PLQYs depending on the concentration of BT emitters in M1:BT/PB perovskite films when excited at 430 nm (excitation of BT guest only), 400 nm (excitation of BT guest and inorganic layers), and 280 nm (excitation of the BT guest, host, and inorganic layers).

In the case of host M2, the presence of the two fluorine atoms on the terphenyl core deepens the HOMO level. The HOMO energy level of M2 was measured by PES, AC-3 and shown in **Figure** 5.12. The deeper HOMO energy level of M2 than M1 resulted in a sharp emission peak from the inorganic layer in M2/PB 2D perovskite (**Figure** 5. 5), indicating a type I heterostructure formation between the M2 and inorganic layers.

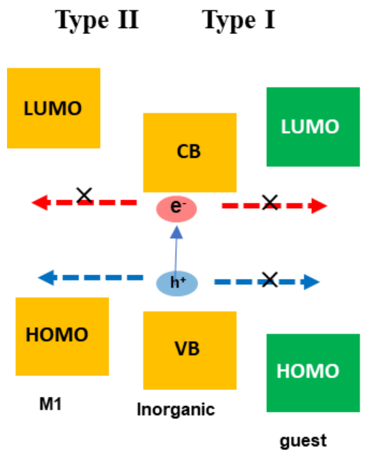

Figure 5. 11 Proposed energy level alignment for M1:BT/PB.

Using the M2 host and BT guest in the perovskite structure, the proposed energy level alignment is given in **Figure** 5.13. In such a hybrid system, the excitons are expected to be confined due to the type I host-inorganic heterostructure. As observed in **Figure** 5.14, with a BT concentration of 20 mol% taken as an example, M2:BT/PB shows PLQYs around 30% and 23% when excited at 400 and 280 nm, respectively, which are higher than M1:BT/PB. However, the PLQYs excited at 400 and 280 nm are still lower than those excited at 430 nm, indicating that energy losses still occur during the energy transfer process.

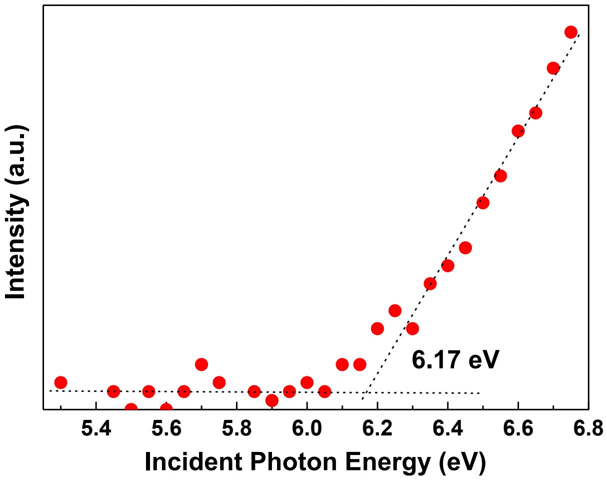

Figure 5.12 PES of M2 organic ligand film.

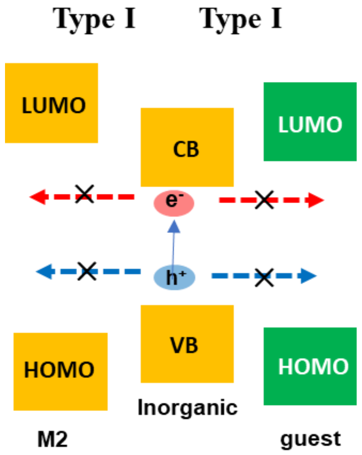

Figure 5. 13 Proposed energy level alignment for M2:BT/PB film.

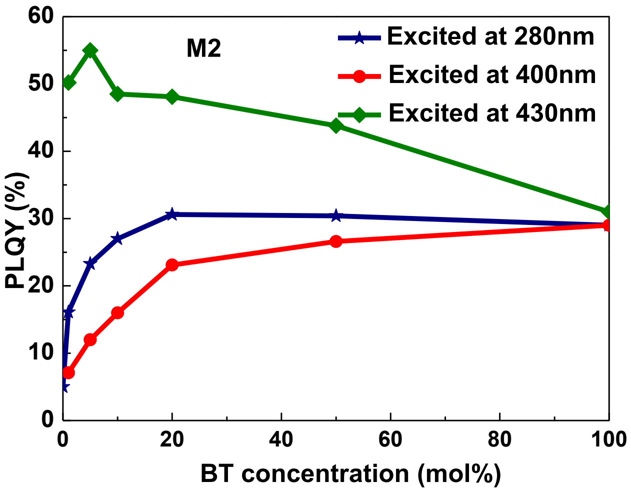

Figure 5. 14 PLQYs depending on BT concentration in M2:BT/PB perovskite films when excited at 430 nm (excitation of BT guest only), 400 nm (excitation of the BT guest and inorganic layers), and 280 nm (excitation of the BT guest, host, and inorganic).

To know the energy losses during the transfer processes between organic and inorganic layers, we attempted to calculate the energy transfer efficiency in the perovskite structures. In the previous chapter, we calculated the energy transfer efficiency to be 89.7% from the inorganic to BT layers. We assumed that this energy transfer efficiency is the same in M2:BT/PB. Thus, 10.3% of energy will be lost when the energy is transferred from the inorganic to the BT layer. Additionally, as shown in **Figure** 5. 15, a significant spectrum overlap exists between the emission spectrum of

M2 and the absorption spectrum of M2/PB, indicating that the energy transfer can occur between M2 and the inorganic layers. Therefore, using the method mentioned in Chapter 4, the energy transfer efficiency from M2 to inorganic was also calculated. The PL transient lifetimes of M2 and M2/PB films are given in **Figure** 5. 16. The significantly shorter PL lifetime of M2 in M2/PB than in pure M2 film indicates the important quenching of the M2 emission. The energy transfer efficiency was then calculated to be 93.2% from M2 to the inorganic layer. It should be emphasized that energy transfer efficiencies are not 100%, and some energy will inevitably be lost during the transfer from M2 to the inorganic layers and then to BT guests.

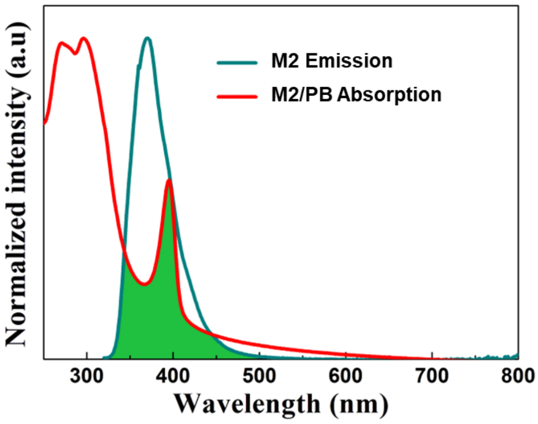

Figure 5. 15 Superposition of the absorption spectrum of an M2 film and the emission spectrum of an M2/PB film.

To address this issue, we proposed to use a host with a larger energy gap, in which the energy transfer from host to inorganic will not happen. Therefore, we synthesized the ligand M3 composed of an ammonium salt of an optically and electrically inert long alkyl chain. Utilizing this insulating ligand M3 to form the M3/PB 2D perovskite, the exciton will be confined in the inorganic layers, as well known as quantum well structures. This is confirmed by the sharp emission peak originating from the inorganic layer as shown in **Figure** 5. 6. By introducing BT guest emitters, the M3:BT/PB 2D perovskite structure was fabricated by the solution process. As evidenced in **Figure** 5. 17, and also observed for M2:BT/PB, the PLQYs of M3:BT/PB increased as the BT emitter concentration decreased when excited at 430 nm. Notably, for the 20 mol% BT guest emitters taken as an example, the PLQY of M3/PB (35%) was slightly higher than that of M2/PB (30%), which could be attributed to the stronger exciton confinement effect by using M3 insulating host.

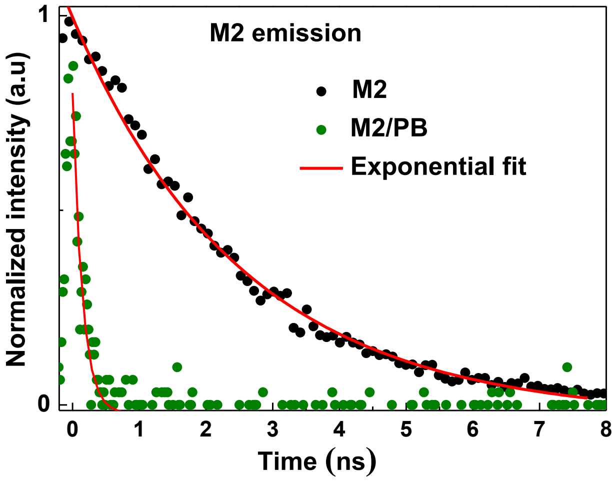

Figure 5. 16 Time-resolved transient PL decay curves of the M2 and M2/PB films.

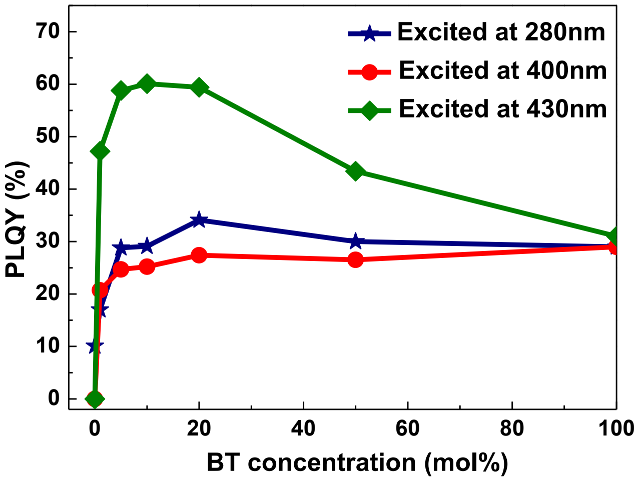

Figure 5. 17 PLQYs depending on BT concentration in M3:BT/PB perovskite when excited at 430 nm (excitation of the BT guest), 400 nm (excitation of the BT guest and inorganic layers), and 280 nm (excitation of the BT guest, host, and inorganic layers)

5.3 Summary

In summary, we investigated the utilization of four different host molecules for the fabrication of multi-component hybrid host-guest (H-G) systems in 2D perovskite structures. We aimed to understand the key requirements for the host molecules in order to enhance the photophysical performances of these systems. Through meticulous host design, considering different factors such as the molecular size and energy level alignment, we identified that an optimal host should possess a similar molecular size to the emitter and exhibit well-matched band alignment with the guest emitter in the H-G system-based 2D perovskites. By employing host molecules of M2 and M3 having large energy gaps and shallow energy levels, we successfully achieved high photoluminescence properties such as high PLQY in such 2D perovskite structures. This chapter provides valuable insights into the design of high-performance multi-component H-G systems in 2D perovskite structures, elucidating the crucial role played by the host molecules.

5.4 Experimental section

5.4.1 Characterization

M0 was synthesized by the chemical reaction of CH_3NH_2 and HBr (both purchased from Wako Pure Chemical), followed by recrystallization twice from a toluene-EtOH blend for purification. M1, M2, and M3 were supplied from Sorbonne University. M1 was mentioned in Chapter 3.

(((2',5'-difluoro-[1,1':4',1''-terphenyl]-4,4''-diyl)bis(oxy))bis(butane4,1 diyl))bis(bromo-l5 azane) (M2)

In a 10 mL round bottom flask fitted with a condenser, Boc-precursor (80 mg 0.12 mmol) was dissolved in a mixture of THF (2 mL) and methanol (1.5 mL) at 45 °C under argon. The solution of aq. HBr (48%) (0.3 mL, 2.6 mmol) was injected into the reaction mixture, and stirred for 24 hrs. under argon. After cooled to room temperature, solvents were removed under reduced pressure. The resulted product was purified by washing with dichloromethane to yield a pale solid (40 mg, 52%). 1H NMR (400 MHz, Methanol-d4) δ 7.56 (d, J = 8.5 Hz, 4H), 7.30 (t, J = 9.0 Hz, 2H), 7.10 – 7.02 (m, 4H), 4.13 (t, J = 5.5 Hz, 4H), 3.06 (t, J = 7.0 Hz, 4H), 1.93 (m, 8H). 19F NMR (400 MHz, Methanol-d4) δ -125.62 (s)

Decyl ammonium bromide (M3): To a cold solution of n-octylamine (0.50 g, 3.87 mmol, 0 °C) in ethanol, HBr (57 wt% aqueous solution, 0.62 mL, 4.64 mmol) was added. The solution was left to stir at room temperature overnight. Most of the solvent was removed under reduced pressure and diethyl ether was added to precipitate the solid. Then, filtration was performed to isolate the white solid (0.89 g, 89%). 1H NMR δH (ppm) (500 MHz, DMSO-d6): 7.59 (s, 3H), 2.76 (t, J = 7.5 Hz, 2H), 1.51 (t, J = 7.0 Hz, 2H), 1.25 (s, 10H), 0.86 (t, J = 6.0 Hz, 3H). 13C NMR δC (ppm) (125 MHz, DMSO-d6): 38.9, 31.2, 28.5, 27.0, 25.8, 22.1, 14.0. FAB-MS (m/z): 130.2 $[M]^+$.

UV-vis absorption spectra and steady-state PL spectra: UV-vis absorption spectra for all the samples were measured on Lambda 950 KPA spectrophotometer (PerkinElmer, USA). Steady-state PL spectra were recorded using an FP-8600 PL spectrometer (JASCO, Japan).

PL quantum yield and time-resolved spectroscopy measurements: Absolute PL quantum yields (PLQYs) were measured on a Quantaurus-QY measurement system (C11347-11, Hamamatsu Photonics) under nitrogen flow and all samples were excited at 280 nm. The transient PL decay characteristics of solution and film samples were recorded at room temperature using a Quantaurus-Tau fluorescence lifetime measurement system (C11367-03, Hamamatsu Photonics). All the samples were excited at 280 nm and the detection wavelength was 400 nm, 420 nm, and 410 nm for M1, M1/PB, and $(BA)_2PbBr_4$, respectively.

PES and LEIPS: The energy levels of all the films used in this study were measured by photoelectron yield spectroscopy (AC-3, Riken Keiki) or low-energy inverse photoemission spectroscopy (LE-1, ALS Technology) and the samples used for the energy-level measurements consisted of 10-nm-thick films spin-coated on ITO-coated glass substrates.

5.5 References

1. Jüstel, T., Nikol, H. & Ronda, C. New developments in the field of luminescent materials for lighting and displays. *Angew. Chem. Int. Ed.* **37**, 3084-3103 (1998).
2. Danielson, E. et al. A combinatorial approach to the discovery and optimization of luminescent materials. *Nature* **389**, 944-948 (1997).
3. Ha, J.M., Hur, S.H., Pathak, A., Jeong, J.-E. & Woo, H.Y. Recent advances in organic luminescent materials with narrowband emission. *NPG Asia Mater.* **13**, 53 (2021).
4. Blasse, G. New luminescent materials. *Chem. Mater.* **1**, 294-301 (1989).
5. Lu, M. et al. Metal halide perovskite light-emitting devices: promising technology for next-generation displays. *Adv. Funct. Mater.* **29**, 1902008 (2019).
6. Quan, L.N., García de Arquer, F.P., Sabatini, R.P. & Sargent, E.H. Perovskites for light emission. *Adv. Mater.* **30**, 1801996 (2018).
7. Veldhuis, S.A. et al. Perovskite materials for light-emitting diodes and lasers. *Adv. Mater.* **28**, 6804-6834 (2016).
8. Liu, Y., Ono, L.K. & Qi, Y. Organic additive engineering toward efficient perovskite light-emitting diodes. *InfoMat* **2**, 1095-1108 (2020).
9. Matsushima, T. et al. Enhanced Electroluminescence from Organic Light-Emitting Diodes with an Organic–Inorganic Perovskite Host Layer. *Adv. Mater.* **30**, 1802662 (2018).
10. Ferdowsi, P., Steiner, U. & Milić, J.V. Host-guest complexation in hybrid perovskite optoelectronics. *J. phys. mater.* **4**, 042011 (2021).
11. Hao, F., Stoumpos, C.C., Cao, D.H., Chang, R.P. & Kanatzidis, M.G. Lead-free solid-state organic–inorganic halide perovskite solar cells. *Nat. Photon.* **8**, 489-

494 (2014).

12. Liu, Y. et al. Efficient blue light-emitting diodes based on quantum-confined bromide perovskite nanostructures. *Nat. Photon.* **13**, 760-764 (2019).
13. Xiao, Z. et al. Efficient perovskite light-emitting diodes featuring nanometre-sized crystallites. *Nat. Photon.* **11**, 108-115 (2017).
14. Feng, Z. et al. Artificial p–n-like Junction Based on Pure 2D Organic–Inorganic Halide Perovskite Structure Having Naphthalene Diimide Acceptor Moieties. *Adv. Opt. Mater.* **11**, 2202734 (2023).
15. Gao, Y. et al. Molecular engineering of organic–inorganic hybrid perovskites quantum wells. *Nat. Chem.* **11**, 1151-1157 (2019).
16. Lédée, F. et al. Tetrazine molecules as an efficient electronic diversion channel in 2D organic–inorganic perovskites. *Mater. Horiz.* **8**, 1547-1560 (2021).

Chapter 6

Conclusions and perspective

Chapter 6: Conclusions and perspective

This chapter summarizes the design routes to realize high-performance H-G systems for light-emitting applications. It outlines future challenges that need to be tackled to implement these systems light-emitting applications.

6.1 Conclusions

This thesis presents a comprehensive investigation of H-G systems ranging from organic-organic to organic-inorganic for light-emitting applications. Host materials are essential components in these systems, facilitating electron and hole transport, and facilitating energy transfer to the emitters. These emitters can include fluorescence, phosphorescence, and TADF. Thus, designing high-performance H-G systems is critical to achieving efficient light emissions.

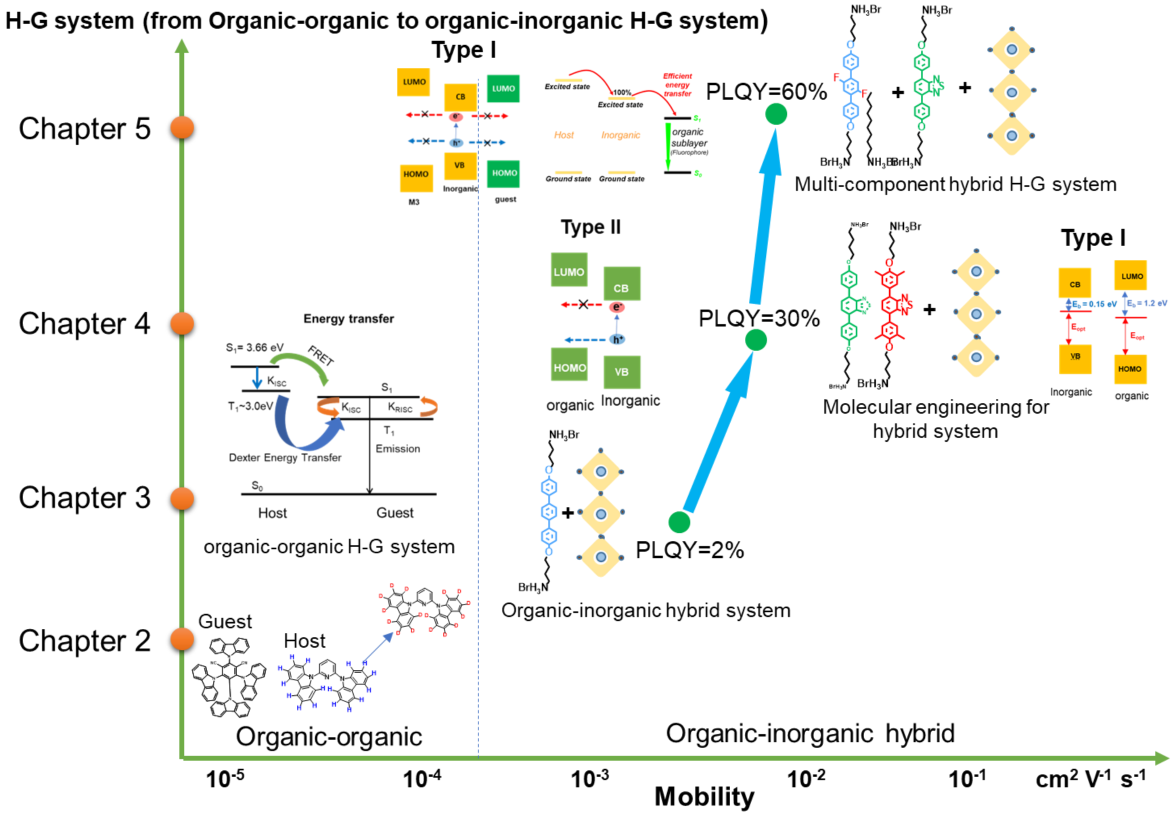

Figure 6.1 Summary of this thesis from organic-organic to organic-inorganic hybrid luminescent materials.

As seen in **Figure** 6.1, in Chapter 2: we introduced a deuterated host, PYD2Cz-d_{16}, and a TADF green emitter, 4CzIPN, to form an organic-organic H-G system. We found that the photophysical properties of the H-G system based on deuterated PYD2Cz-d$_{16}$ are similar to that of the non-deuterated PYD2Cz host. More importantly, deuterated PYD2Cz-d1$_6$ forms a denser film than PYD2Cz, resulting in different carrier transport properties as demonstrated by HODs/EODs. The green device using the deuterated H-G system exhibited enhanced stability (LT$_{95}$) of 1.7 times longer than that of the PYD2Cz system. The well-balanced carrier transport properties of PYD2Cz-d$_{16}$ can provide a broad recombination zone, thus increasing the LT$_{95}$ in OLEDs.

Chapter 3 introduced a novel organic molecule called M1 and its use in fabricating an organic-inorganic H-G structure, M1PB. The chapter examined the thin-film structure, morphology, and crystal structure of this hybrid architecture, as well as its electronic and photophysical properties, through both experimental and theoretical investigations. The charge transport properties of this type II 2D hybrid heterostructure were also probed using HODs/EODs. The results demonstrated that this hybrid material, composed of intertwined M1 and PbBr$_4$ inorganic monolayers, presents two intercalated separate pathways for electrons and holes that can migrate within the inorganic and organic sublayers, respectively. This work provides insight into the band alignment effect on the performance of inorganic-organic H-G systems, which is of paramount importance for future optoelectronic applications.

Chapter 4 extended the previous section. Two major issues need to be addressed for light-emitting applications: exciton dissociation at the Type II heterointerface and limited charge transport in horizontally oriented films. To overcome these challenges, we designed and synthesized new organic fluorophores (BT and 4mBT) with a diamine group and incorporated them into the inorganic framework to form an H-G system. The resulting perovskite films exhibited a type I heterostructure, confining excitons for efficient light-emission, and vertically oriented structures that allow for charge carriers to travel through the inorganic layers between two electrodes. The 2D perovskite films with a type I heterostructure exhibited efficient FRET from the inorganic layer to the organic layer, resulting in high PLQYs. These vertically oriented hybrid H-G systems with efficient interlayer energy transfer hold great potential for optoelectronic device applications.

Chapter 5: In the previous chapter, we successfully fabricated vertically oriented perovskite films containing an inorganic-organic H-G system. However, we found that the PLQY of these perovskite films was lower than that of the pure organic solution. To address this issue, we introduced several host materials into the perovskite structure to form a multi-component H-G system. This approach allowed for the dispersion of the emitter, such as the BT molecule, by the host material, which reduced concentration quenching. Additionally, we investigated the molecular length and energy level requirements of the organic host in the perovskite structure. By carefully selecting the host materials, the multi-component H-G systems showed higher PLQY than the single H-G system, which contains only the inorganic layer and pure emitter layer. This work provides a deep understanding of the critical role played by host materials in organic-inorganic hybrid structures for achieving high PLQY, which is essential for optoelectronic device applications.

6.2 Perspective

The use of H-G systems in light-emitting applications, such as OLEDs, has been extensively researched in the context of organic-organic systems. However, the potential advantages of utilizing both organic and inorganic semiconductors in the organic-inorganic hybrid system are not yet fully understood. We have designed several systems that combine organic and inorganic materials for light-emission. As discussed above, these systems have become prominent platforms to explore the photophysics of organic-inorganic semiconductors in the perovksite matrics. As expected, efficient emission could be emitted from Type I heterostructure, while queched in Type II heterostructrue. In future work, Type III band alignment, as shown in **Figure** 6.2, is theoretically plausible if the energy transfer is restricted. This could be achieved by incoporating strongly electron-donating or accepting organic ligands or by using quasi-

2D perovksites to reduce the inorganic band gap. These systems could potentially produce spontaneous charge transfer or white emission as a combination of both organic and inorganic emissions.

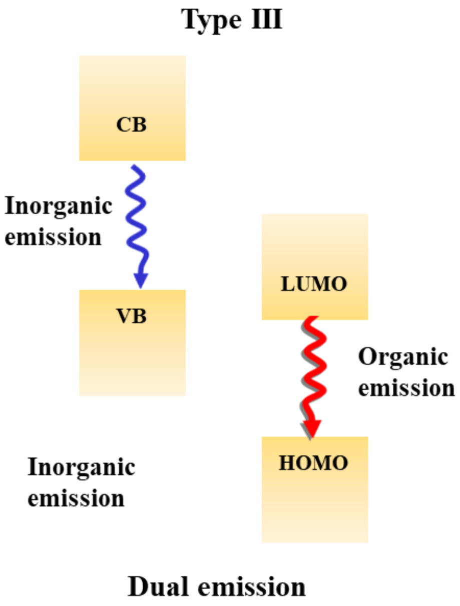

Figure 6.2 Imaginary case of Type III band alignment in perovskite system.

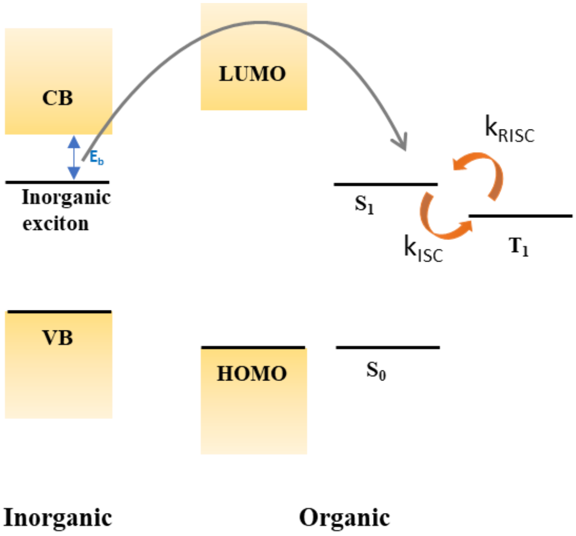

Figure 6.3 Energy and band diagrams of inorganic and organic semiconductors. The singlet and triplet levels of organic semiconductors are shown as well.

In addition, these hybrid systems have not been used in OLEDs due to poor morphology and other unresolved issues. In future work, improving the film quality and device structure could lead to improved device performance. Additionally, given the significant enhancement of spin-orbital coupling (SOC) efficiencies of organic cations from the external heavy atom effects of lead-halide inorganic lattices, incorporating efficient organic phosphors or TADF molecules that ultilizes triplet excitons can enable the realization of the full potential of perovskite matrices to enhance the emitting performance of organic semiconductors, particularly triplet emitters as shown in **Figure** 6.3.

Acknowledgement

It is astonishing to realize that nearly four years have elapsed since my arrival in Fukuoka. The memories of my time here remain vivid in my mind, as if it were just yesterday. Throughout the journey of completing this dissertation, I have been immensely fortunate to receive guidance and support from numerous individuals who have played an indispensable role in my academic pursuits.

First and foremost, I would like to express my heartfelt gratitude to my supervisor, Professor Chihaya Adachi. His unwavering support and invaluable advice have been instrumental in shaping my research process. Professor Adachi's benevolence, intelligence, diligence, and erudition have left an indelible mark on me, inspiring both my academic and daily life. I am truly grateful for the profound lessons and experiences that will undoubtedly guide my future career.

I extend my deepest appreciation to Professor Fabrice Mathevet for his insightful discussions and constructive comments, not only on this dissertation but also throughout my Ph.D. journey. His guidance extended beyond the realm of academia, encompassing experimental skills and life lessons. Professor Mathevet's contributions have been invaluable in shaping the development of my research.

I would like to express my gratitude to Associate Professor Hajime Nakanotani for his meticulous review of my presentation and the invaluable comments provided. His suggestions have significantly contributed to refining my presentation during the preparation of the oral defense.

I am also grateful to Associate Professor Chin-Yiu Chan for his patience and guidance during my doctoral studies. I am indebted to him for his assistance when I first joined the Adachi lab, as I was unfamiliar with the equipment, laboratory rules,

and regulations. Despite the challenges I faced, Associate Professor Chan's unwavering patience and understanding ensured my smooth integration into the lab.

I would like to acknowledge the contributions of Professor Toshinori Matsushima, whose assistance greatly aided my experiments. His kind suggestions and valuable comments played a crucial role in enhancing the quality of my work.

My heartfelt appreciation goes out to the members of the SC group, including Dr. Zhao Feng and Kentaro Imaoka, for their inspiring discussions and critical feedback. I am also grateful to Ms. Nozomi Nakamura and Keiko Kusuhara for their technical support.

I would like to express my sincere gratitude to Prof. Hayashi and Prof. Oki for their valuable time in reviewing my thesis and attentively listening to my presentation. Their valuable suggestions and comments have contributed to the improvement of my work.

I extend my gratitude to Prof. Xiankai Chen, Associate Professor Youichi Tsuchiya, Assistant Prof. Kenichi Goushi, Masashi Mamada, Dr. Yiting Lee, Dr. Xun Tang, Dr. Tai Chen, Dr. Zesen Lin, Dr. Tomohiro Ishii, and Dr. Ganbaatar Tumen-Ulzii for their contributions and support.

I am profoundly grateful to my beloved wife, for her endless love, understanding, and unwavering support throughout my doctoral journey. Her encouragement and sacrifices have been instrumental in my success.

A special thanks goes to all the staff members of Adachi's group for their continuous support and care during my time in the laboratory. I am especially grateful to Ms. Chihiro Hino and Sachiko Higashikawa for their invaluable assistance with my

Ph.D. degree application. These acts of kindness and support will forever hold a special place in my heart.

Fukuoka
June 2023
Xuelong Liu

Appendixes

List of Chemical Compounds

PYD2Cz	2,6-di(9H-carbazol-9-yl-)pyridine
PYD2Cz-d_{16}	2,6-di(9H-carbazol-9-yl-)pyridine-d_{16}
HAT-CN	1,4,5,8,9,11-hexaazatriphenylene-hexacarbonitrile
Tris-PCz	9,9′,9″-triphenyl-9*H*,9′*H*,9″*H*-3,3′:6′3″-tercarbazole
T2T	2,4,6-tris(biphenyl-3-yl)-1,3,5-triazine
BPy-TP2	2,7-bis(2,20- bipyridine-5-yl)triphenylene
***m*CBP**	3,3-di(9*H*-carbazol-9-yl)biphenyl
LiF	lithium fluoride
Al	aluminum
5CzBN	penta(9H-carbazol-9-yl)benzonitrile
4CzIPN	1,2,3,5-tetrakis(carbazol-9-yl)-4,6-dicyanobenzene
M1	4,4'-([1,1':4',1"-terphenyl]-4,4"-diylbis(oxy))bis(butan-1-aminium)dibromide
M1’	4,4"-bis(decyloxy)-1,1':4',1"-terphenyl
C_{60}	fullerene
MoO_x	molybdenum trioxide
Au	Gold
DMF	N,N-dimethylformamide
DMSO	dimethyl sulfoxide
BT	4,4'-((benzo[c][1,2,5]thiadiazole-4,7-diylbis(4,1 phenylene))bis(oxy))bis(butan-1-aminium) bromide
4mBT	4,4'-((benzo[c][1,2,5]thiadiazole-4,7-diylbis(2,6-dimethyl-4,1 phenylene))bis(oxy)) bis(butan-1-aminium)dibromide
DCM	Dichloromethane
$PbBr_2$	lead bromide

List of Abbreviations

CIE	commission internationale de l‟Eclairage
DFT	density functional theory
DSC	differential scanning calorimetry
EBL	electron blocking layer
EIL	electron injection layer
EL	electroluminescence
EML	emissive layer
EQE	external quantum efficiency
ETL	electron hole transport layer
eV	electron volt
GIWAXS	Grazing-incidence wide-angle X-ray scattering
HBL	hole blocking layer
HIL	hole injection layer
HOMO	highest occupied molecular orbital
HTL	hole transport layer
IC	internal conversion
IQE	internal quantum efficiency
ISC	intersystem crossing
ITO	indium tin oxide
LUMO	lowest unoccupied molecular orbital
LEIPS	low-energy inverse photoemission spectroscopy
NMR	nuclear magnetic resonance
OLEDs	organic light emitting diodes
PL	photoluminescence
PLQY	photoluminescence quantum yield
RISC	reverse intersystem crossing
PES	photoelectron spectroscopy
PBE	Perdew-Burke-Ernzerhof

SCLC	space charge limited current
SOC	spin-orbit coupling
TADF	thermally activated delayed fluorescence
TGA	thermogravimetric analysis
UV	ultraviolet
XRD	X-ray Diffraction
PDOS	Computed projected density of states

List of important Symbols

S_0	singlet ground state
S_1	lowest singlet excited state
T_1	lowest triplet excited state
λ	wavelength
f	oscillator strength
k_r	radiative decay rate
k_nr	non-radiative decay rate
k_ISC	intersystem crossing rate
k_RISC	reverse intersystem crossing rate
k_Ph	radiative decay rate of phosphorescence
τ_S	singlet lifetime
τ_T	triplet lifetime
Φ_PL	fluorescence quantum yield
Φ_Ph	phosphorescence quantum yield
Φ_p	prompt fluorescence quantum yield
Φ_d	delayed fluorescence quantum yield
μ	charge carrier mobility
J	current density
V	voltage
k_B	Boltzmann constant
η_EQE	external quantum efficiency
η_r	charge carrier balance factor
η_out	outcoupling factor
ΔE_ST	singlet-triplet energy splitting
T_{50}	half lifetime
nm	nanometer
ns	nanosecond
μ**s**	microsecond

°C	degrees Celsius
Å	Angstrom
h	hour
K	kelvin
β	Poole–Frenkel factor
L	luminance
T_g	glass transition temperature
T_m	thermal decomposition temperature

List of publications and symposiums

Original papers

1) **Xuelong Liu**, Chin-Yiu Chan*, Fabrice Mathevet, Masashi Mamada, Youichi Tsuchiya, Yi-Ting Lee, Hajime Nakanotani, Chihaya Adachi*. "Isotope Effect of Host Material on Device Stability of Thermally Activated Delayed Fluorescence Organic Light-Emitting Diodes" Small Sci., **2021**, 1, 2000057.
2) **Xuelong Liu**, Chin-Yiu Chan, Lydia, Youichi Tsuchiya, Toshinori Matsushima, Xiankai Chen, Fabrice Mathevet*, and Chihaya Adachi*. "Investigation of charge transport properties in a 2-Dimensional (2D) Dion-Jacobson halide perovskite-basedperovskite based on terphenyl dications", *ACS Mater. Lett.* **2023** (Submitted).
3) **Xuelong Liu**, Zhangsheng Shi, Chin-Yiu Chan, Youichi Tsuchiya, Toshinori Matsushima, Fabrice Mathevet*, and Chihaya Adachi*. "Vertical orientated 2D organic-inorganic hybrid perovskite incorporating fluorophores" **2023** (to be submitted).
4) **Xuelong Liu**, Robin Troiville-Cazilhac, Fabrice Mathevet* and Chihaya Adachi* "Investigation of charge transport properties of terphenyl derivative based Liquid crystal in organic thin film transistor (TFT) configuration" **2023** (to be submitted)

Joint Papers

1) Lihua Chen, Chuanlong Li, Enguang Fu, Mengyang Li, Yoshiaki Kuboi, Zi-Ying Li, Zhenghong Chen, Jiaolong Chen, **Xuelong Liu**, Xun Tang, Lucas Frédéric, François Maurel, Chihaya Adachi, Fabrice Mathevet*, and Shaodong Zhang*. "A Donor−Acceptor Cage for Thermally Activated Delayed Fluorescence: toward a New Kind of TADF Exciplex Emitters." *ACS Mater. Lett.* **2023**, 5, 1450-1455
2) Zhao Feng, **Xuelong Liu**, Imaoka Kentaro, Tomohiro Ishii, Ganbaatar Tumen-Ulzii, , Xun Tang, George F. Harrington, Fabrice Mathevet*, and Chihaya Adachi*, Artificial p-n-like junction based on pure 2D organic-inorganic halide perovskite structure having naphthalene diimide acceptor moieties. **Adv. Opt. Mater**. **2023**, 2202734.

Symposiums

1) **Xuelong Liu**, Chin-Yiu Chan, Fabrice Mathevet, and Chihaya Adachi. "Investigation of charge transport properties in a Dion−Jacobson-type 2D organic-inorganic perovskite." *The 83rd JSAP Autumn Meeting 2022*, **Poster Presentation**, Sendai, Japan, (Sep. **2022**)
2) **Xuelong Liu**, Fabrice Mathevet, and Chihaya Adachi. Isotope Effect on Device Stability of Thermally Activated Delayed Fluorescence Organic Light-Emitting Diodes (TADF OLEDs). *International Conference on the Science and Technology of Synthetic Metals (ICSM)*, **Poster Presentation**, Glasgow, UK, (July. **2022**)